Department of Ocean, Technology, Policy, and Environment
Graduate School of Frontier Sciences
The University of Tokyo

2018

Master's thesis

Free-surface and free-end effects on flow around half-submerged circular cylinders
(半没水円筒周りの流れに対する自由表面及び端部の影響)

Submitted January 23, 2019

Supervisor Professor Hideyuki Suzuki
Associate Professor Shinichiro Hirabayashi

47-176634 Keigo Sakata

Abstract

Floating offshore wind turbines (FOWTs) are subjected to severe environmental loads due to winds, waves, and currents. Vortex-induced motion (VIM) is the result of the exciting forces by vortex shedding on the hull of a bluff body exposed to currents. VIM results in additional oscillating mooring line tensions and affects mooring lines' fatigue damage seriously. Concerning economy, exchanging mooring lines is not desirable during the service lifetime of FOWT. To predict the service lifetime of mooring lines and design the rational floating body and mooring lines, the mechanism of VIM needs to be clarified. The VIM behavior is more susceptible in low aspect ratio structures such as a spar, monocolumn, and multi-columns platforms. Free-surface and free-end effects are supposed to be large because of the low aspect ratio. However, free-surface and free-end effects in VIM have not been investigated fully. Then, this experimental study tried to figure out the free-surface and free-end effects on half-submerged circular cylinders. To achieve this goal, two experiments were performed.

PIV measurements were carried out in a recirculating water channel at the Reynolds number of 43,000 & 23,000 to understand the three-dimensional flow structures around the free end of half-submerged circular cylinders with low aspect ratio. The differences of vortices showing up among different aspect ratios were presented.

Forces in streamwise and transverse directions were measured for half-submerged circular cylinders in a towing tank and a recirculating water channel to understand the free-surface effect. By evaluating forces in streamwise and transverse directions as a function of each non-dimensionalized number, the effect of each parameters were discussed.

From these two experiments, some new findings were obtained about:

- the three-dimensional flow structure around half-submerged circular cylinders with low aspect ratio
- the effect of aspect ratio on the hydrodynamic force and vortex structure (free-end effect)

- the effect of Froude number on the hydrodynamic force and vortex structure (free-surface effect)
- the effect of each non-dimensionalized parameter (Reynolds number, Froude number, and aspect ratio) on the hydrodynamic force and the interaction effect of them

Table of Contents

List of Tables

List of Figures

Nomenclature

Abbreviations

2D	Two-dimensional
3D	Three-dimensional
CFD	Computational Fluid Dynamics
DMD	Dynamic Mode Decomposition
FFT	Fast Fourier Transformation
LES	Large Eddy Simulations
PIV	Particle Image Velocimetry
POD	Proper Orthogonal Decomposition
PSD	Power Spectrum Density
VIM	Vortex-Induced Motion
VIV	Vortex-Induced Vibration

Symbols

D	cylinder diameter[m]
L	submerged cylinder length[m]
$AR = \frac{L}{D}$	aspect ratio[-]
U	constant towing velocity[m/s]
ν	coefficient of kinetic viscosity[m^2/s]
$Re = \frac{UD}{\nu}$	Reynolds number[-]
g	acceleration of gravity[m^2/s]
$Fr = \frac{U}{\sqrt{gD}}$	Froude number[-]
f	frequency[s]
St	Strouhal number[-]
Fx	streamwise force[N]
Fy	transverse force[N]
ρ	water density[kg/m^3]
Cx	non-dimensionalized streamwise force[-]
Cy	non-dimensionalized streamwise force[-]

Vx	streamwise velocity
Vy	transverse velocity
Vz	vertical velocity
Mean V	time-averaged mean velocity
RMS V	root-mean-square component velocity
$\omega_x D/U$	non-dimensionalized mean streamwise component of vorticity vector ($\omega_x = \frac{\partial V_z}{\partial y} - \frac{\partial V_y}{\partial z}$)
$\omega_y D/U$	non-dimensionalized mean transverse component of vorticity vector ($\omega_y = \frac{\partial V_x}{\partial z} - \frac{\partial V_z}{\partial x}$)
$\omega_z D/U$	non-dimensionalized mean vertical component of vorticity vector ($\omega_z = \frac{\partial V_y}{\partial x} - \frac{\partial V_x}{\partial y}$)
$\omega_m D/U$	non-dimensionalized mean magnitude of vorticity vector ($\omega_m = \sqrt{{\omega_x}^2 + {\omega_y}^2 + {\omega_z}^2}$)

In this thesis, as physical constants, $\nu = 1.0 \times 10^{-6}, g = 9.8, \rho = 1000$ are adopted.

Chapter 1 Introduction

1.1 Background and motivation

The last two decades have seen a growing demand for renewable energy sources in the world. Floating offshore wind turbine (FOWT) is an emerging technology in maritime renewable energies. The offshore wind market has so far been dominated by countries with relatively shallow water depths (<50m) and more countries are beginning to explore the potential for floating offshore wind. Various types of offshore wind turbines are presented in Figure 1.1. The exponential rise of offshore wind energy can be attributed to a number of factors, abundance of space and consistent wind resources, which result in an energy output up to 40% higher than onshore. There is significant potential and appetite for the growth of FOWT in Japan, the United States, and a number of European countries including the Norway, France, UK, Portugal, and Spain (Table 1.1). Floating offshore wind market outlook is presented in Figure 1.2. Although fossil fuels will occupy the largest part of the world's use of energy in the decades ahead, demand for wind power will be expected to increase rapidly.

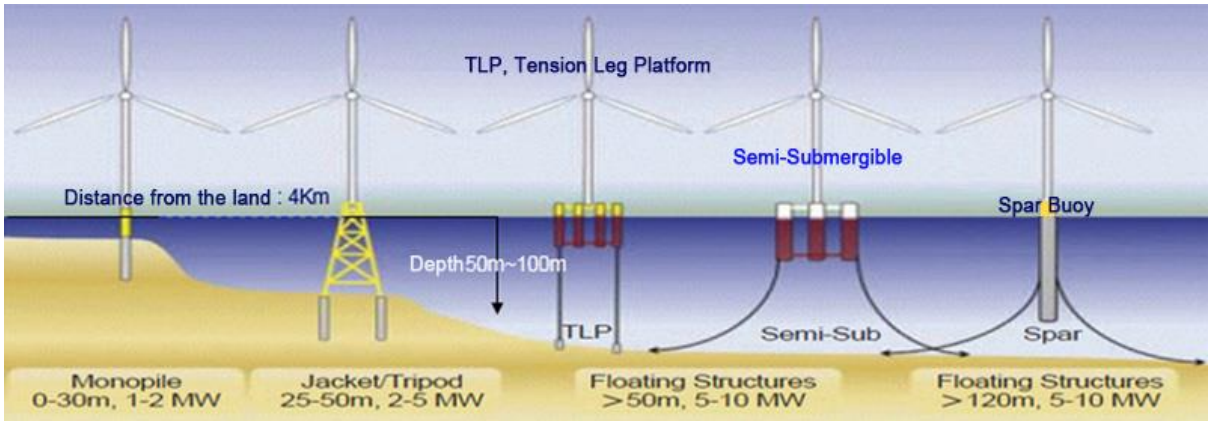

Figure 1.1 - Types of offshore wind turbines from MASTEK HP

Table 1.1 - Offshore wind resource and potential floating wind capacity in Japan, USA, and Europe

(US NREL, 2012; EWEA, 2013; Marine International Consulting, 2013)
(reproduced from James and Ros (2015))

Country/Region	Share of offshore wind resource in deep water locations (>60m depth)	Potential floating wind capacity
Japan	80%	500GW
USA	60%	2450GW
Europe	80%	4000GW

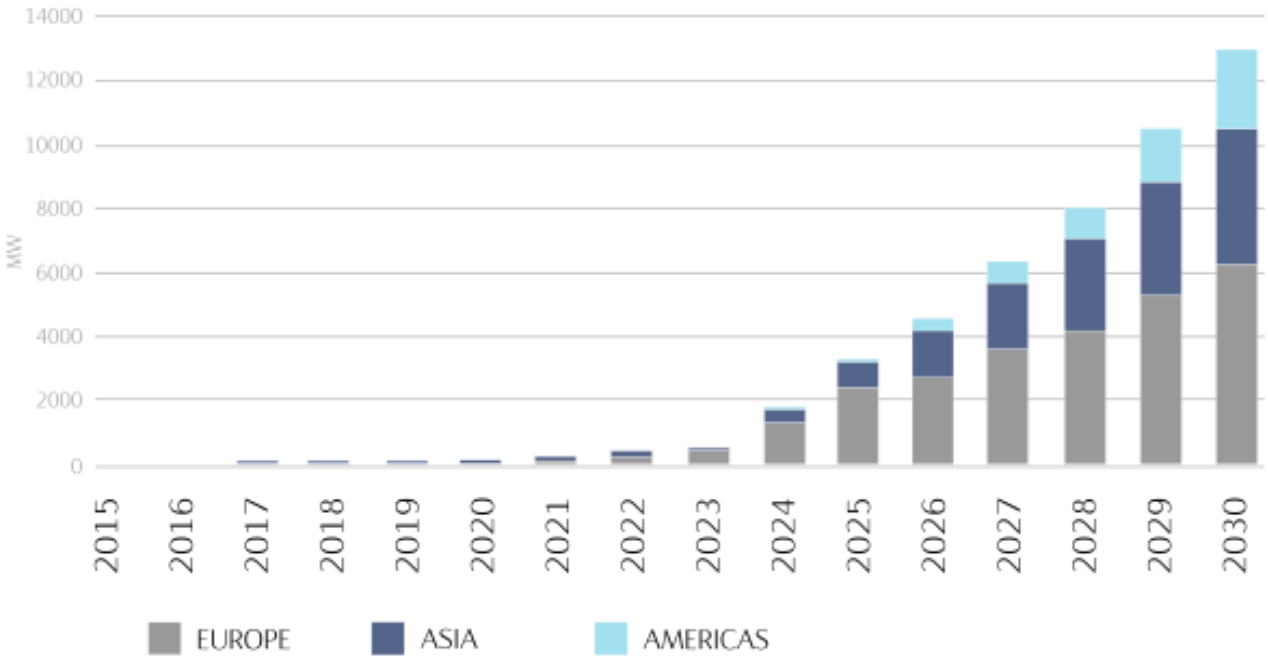

Figure 1.2 - Floating offshore wind market outlook from equinor HP

FOWTs show complex motion behavior subjected to severe environmental loads due to winds, waves, and currents. The floating body part in currents experiences periodic motion induced by vortex shedding from the body. This behavior is called Vortex-Induced Motion (VIM). VIM results in additional oscillating mooring line tensions and affects mooring lines' fatigue damage severely. Concerning economy, changing mooring lines is not desirable during the service lifetime of FOWT. The mechanism of VIM needs to be clarified to predict the service lifetime of mooring lines and better design the

floating unit. The VIM behavior is susceptible in offshore platforms such as a spar, monocolumn, and multi-columns platforms, see examples by Gonçalves *et al.* (2010) [1]. The main characteristic of these platforms is to present a low aspect ratio (ratio of the draft to the characteristic diameter). Free-surface and free-end effects are supposed to be large because of the low aspect ratio. However, these effects in VIM have not been investigated fully. As an initial stage of the research, this study tried to figure out the free-surface and free-end effects on flow around half-submerged circular cylinders. The detail is explained in section 2.3 in Chapter 2.

1.2 Structure of the thesis

The present thesis is divided into 6 chapters, including this introduction:

_ Chapter 2 presents the fundamental knowledge about the phenomenon of vortex shedding from bluff bodies and literature review about flow around a single circular cylinder and hydrodynamic force for a single circular cylinder. Moreover, this chapter also explains objectives and methodology of this study and what differs the present study from the preceding studies.

_ Chapter 3 describes the PIV measurement experiment and results.

_ Chapter 4 describes the force measurement experiment and results.

_ Chapter 5 expands discussions based on two experiments results.

_ Chapter 6 concludes the thesis summarizing the main findings and contributions of the present study. It also suggests future suggestions to advance the present investigation.

Chapter 2 Flow around circular cylinders

2.1 Vortex shedding from bluff bodies

2.1.1 Boundary layers and separation

Flow visualization around a cylinder in water current is shown in Figure 2.1. As the stream approaches the cylinder, the flow splits into upper and below parts respectively. Boundary layers develop from the front stagnation point while the flow remains attached to the solid wall unless separation is initiated. The separation is generated by the development of the adverse pressure gradient. The vortices which the detached layers roll up and form are conveyed ahead in the cylinder wake, the area behind the cylinder.

The flow around bluff bodies is characterized by the Reynolds number (Re), which is the dimensionless parameter most widely used today. Re is defined as:

$$\mathrm{Re} = \frac{UD}{\nu}$$

where U is the velocity of the uniform flow undisturbed by the presence of the cylinder with diameter D in case that the bluff body is a cylinder. ν is the kinetic viscosity of the fluid.

The flow behavior changes as Re increases. This is categorized by Sumner and Fredsøe (2006). The repeating pattern of rolling vortices in the wake of the cylinder is often called von Kármán vortex street. The vortex shedding frequency is commonly characterized by the dimensionless parameter St (Strouhal number). St is defined as:

$$\mathrm{St} = \frac{\mathrm{fD}}{\mathrm{U}}$$

when f is the vortex shedding frequency. This St is a function of Re. For a wide range of subcritical Re, St is almost constant with values around 0.2. At the transition to the super-critical Re, St sharply increases.

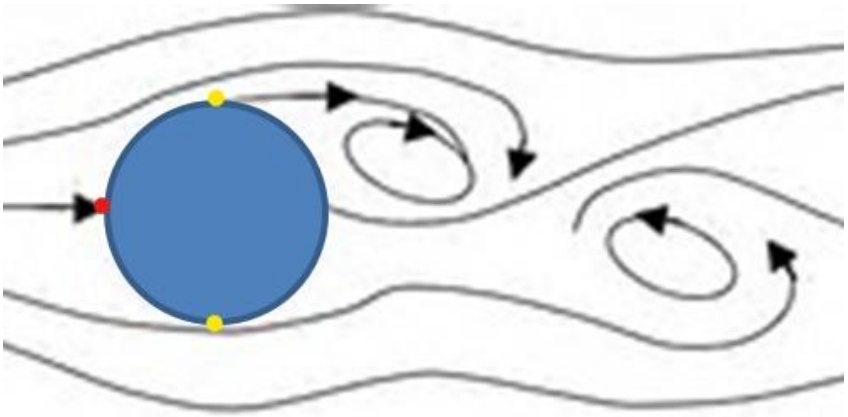

Figure 2.1 - Visualization of the flow around a circular cylinder
The red dot is the front stagnation point. The yellow dots are the separation points. (reproduced from van Dyke (1982))

2.1.2 VIV and VIM

A fluid flow past a bluff body, such as a circular cylinder, generates periodic vortex shedding in the wake for all but very low Reynolds numbers. This process gives rise to oscillatory lift and drag forces if the body is elastically supported. This is called Vortex-Induced Vibration (VIV). VIV can lead to fatigue damage in vibrating structures, such as bridges, chimney stacks and marine riser pipes.

Vortex-Induced Motion (VIM) has basically the same generation mechanism as VIV. Both phenomena are caused by the exciting forces due to the periodic vortex shedding from the hull of a bluff body. VIM occurs to a platform and increases tensions of mooring cables. As mentioned in Chapter 1, one of the characteristics of VIM is the low aspect ratio (ratio between the draft and the characteristic diameter).

2.2 Review of previous studies on flow around circular cylinders

The subjects of previous studies on flow around circular cylinders are roughly divided into 3 types as shown in below.

2.2.1 Cylinders with free ends

The free-end effect on vortex shedding in the case of circular cylinders has been studied by many authors for the cylinder fixed on the ground plane, see the example by Kawamura *et al.* (1984).

Khalak & Williamson (1996) measured the lift force of a circular cylinder with free-end at Re=10 600. They showed that a peak due to Karman vortex shedding, as well as a peak due to a vortex whose frequency was approximately 1/3 of the Karman vortex-shedding frequency appeared in the power spectrum of the lift force. This means the end-cell-induced vibration (ECIV). ECIV was induced by the tip-associated vortices of this non-dimensionalized vortex-shedding frequency 0.067. Kitagawa *et al.* (1998) and Park & Lee (2000) also mentioned about this.

Some investigations have considered the flow structure around the low-aspect-ratio and wall-mounted cylinders. Pattenden *et al.* (2005) sketched the flow around cylinders on the ground plane with aspect ratio equal one, and showed that there are some kinds of vortex namely, tip vortex, arch vortex, trailing vortex, and horseshoe vortex. The paper by Sumner (2013) is an excellent review of this theme.

Recently, Zhu *et al.* (2017) revealed the 3D M-Shape arch-type vortex around the free end of the cylinder with AR=2 fixed on the plane at Re=3830 by using the tomographic PIV.

2.2.2 Half-submerged cylinders

Froude number, Fr is also an important parameter in fluid mechanics. Dimensionless Navier-Stokes equation for incompressible fluid in gravity field is

$$\frac{\partial u_i}{\partial t} + u_j \frac{\partial u_i}{\partial x_j} = -\frac{\partial p}{\partial x_i} + \frac{1}{Re}\frac{\partial^2 u_i}{\partial {x_j}^2} - \frac{1}{Fr^2}\delta_{i3}$$

This solutions depend on Re and Fr. Fr is defined as below.

$$\mathrm{Fr} = \frac{U}{\sqrt{gD}}$$

Fr is the parameter to characterize the free surface.

Half-submerged cylinders have been investigated both experimentally and numerically. Experiments on surface-piercing cylinders were carried out by Inoue *et al.* (1993) and Akilli and Rockwell (2002), and Chaplin and Teigen (2003).

Inoue et al. (1993) carried out a towing tank experiment using a cylinder of 5cm in diameter for two Froude numbers, Fr=0.8 and 1.0. They stated that the periodic vortex shedding is attenuated near the free surface.

Akilli and Rockwell (2002) investigated the flow around a half-submerged cylinder on the ground plane in shallow water at Re=10052. In the shallow water, the effect of the finite distance between the bed and the free surface is associated with a three-dimensional mechanism that arouses a horizontally-oriented vortex, which is evident immediately beneath the free surface. However, the dimensionless circulation of this vortex is an order of magnitude smaller than that of the quasi-two-dimensional Kármán vortex.

Chaplin and Teigen (2003) carried out an experimental study with Froude numbers Re between 0.4 and 1.64 and Reynolds numbers Re between 12000 and 47000 at constant values of the ratio $\frac{\mathrm{Re}}{\mathrm{Fr}} = \frac{\sqrt{gD^3}}{\nu} = 27900$ for a vertical surface-piercing circular cylinder with a large draught. It was found that the total resistance coefficient reached a maximum at Fr~1. They also found that the local drag coefficient on the cylinder decreased near the free surface.

Numerical work on the drag coefficients of half-submerged cylinders has been carried out in Kawamura *et al.* (2002), Yu *et al.* (2008), Suh *et al.* (2011), and Koo *et al.* (2014).

Kawamura *et al.* (2002) investigated the wave-wake interaction about a half-submerged circular cylinder using Large-Eddy Simulation (LES) at

Re=27,000 with three different Fr =0.2, 0.5 and 0.8. At a low Fr, surface deformations were small and the influence on the wake was negligible. On the contrary, the generated surface wave was very steep and strongly unsteady at a high Fr. They were able to visualize the attenuation of vortex shedding near the interface.

Previous work, both experimental and numerical, demonstrates that the presence of a free surface leads to a decrease of local drag coefficient. In addition to effects on the drag behavior, the presence of a free surface has been shown to affect vortex shedding and lift forces. Yu *et al.* (2008) found that vortex shedding was suppressed near the free surface, which alters the lift forces acting along the length of the cylinder.

Suh *et al.* (2011) performed large-eddy simulation of the flow past an interface piercing circular cylinder at Re=27000 and Fr=0.2 and 0.8. Organized periodic vortex shedding was observed in the deep flow whereas it disappeared near the interface and small-scale vortices inclined along the interface were observed. The streamwise vorticity and outward transverse velocity generated at the edge of the separated region due to the lateral gradient of the difference between the vertical and transverse Reynolds sheer stress increasing with the Froude number are responsible for the attenuation of organized periodic vortex shedding.

Koo *et al.* (2014) numerically studied the wave run-up height and depression depth around air-water interface-piercing circular cylinder. Kelvin waves behind the cylinder were generated and its wave lengths are longer and its angles are smaller as Froude numbers increase.

From the prior research, Sareen *et al.* (2018) inferred for a cylinder that the free surface acts like a rigid free-slip boundary for low Froude numbers of Fr<0.5. For 0.8<Fr<2, the free surface influences the shedding near the free surface, leading to 3D features very close to the free surface; however, for very high Froude numbers of Fr>2, the free surface was significantly deformed; there were then strong wave–wake interactions, and the periodic vortex shedding was suppressed for cylinder depths less than one diameter from the free surface.

2.2.3 Half-submerged cylinders with free ends

Investigations of finite cylinders have been carried out both experimentally and numerically for the needs of various engineering applications. This is the case of our interest. Most cases targeted cylinders on the ground plane or surface-piercing cylinders with a large draft. On the other hand, the case of the cylinders with low aspect ratio piercing the free surface needs more attention and to be better studied for the offshore scenario. However, there are few works for L/D<2 and piercing the free surface.

Gonçalves *et al.* (2015) measured the drag and lift forces for a 0.125m diameter cylinder at 8 different aspect ratios, namely 0.1, 0.2, 0.3, 0.5, 0.75, 1.0, 1.5 and 2.0. The range of Reynolds number covered 10000<Re<50000. They also visualized the flow around two horizontal planes and one vertical plane for low aspect ratio cylinders including the free-surface with L/D=2.0, 1.0, 0.5, 0.3 by PIV. The results showed a decrease in drag force coefficients and a decrease in Strouhal number with decreasing aspect ratio. The PIV measurements and the PSD of forces showed different behavior for cylinders with AR<0.5, in which cases the free-end effects were predominant. Even without von Kármán street main characteristics around the majority length of the cylinder, in the range of 0.2<AR<0.5, the vortex shedding from the bottom of the cylinder produced alternating forces in the transverse direction.

Fukuoka *et al.* (2016) also conducted PIV and force measurement. The conditions range of PIV measurement was 4100<Re<12600, 0.14<Fr<0.42, and 1.0<AR<4.0. Force measurement conditions including other works are presented in Table 1. Forces at the same non-dimensionalized parameters were compared. However, the force measurement data were not filtered and included high frequencies which is not physically meaningful. Therefore, they confined to conclude that the dependency of mean drag coefficient on Re is different for different aspect ratios. The statements about force fluctuation that the fluctuating components of the force decreases with the increasing Fr should be discussed at the appropriate range frequency, 0<fD/U<0.5.

Benitz *et al.* (2016) carried out numerical and experimental work at Re=2900, Fr=0.65, 0.875<AR<19. They showed a reduction of Strouhal number at AR=9 and attenuation of periodic vortex shedding at AR=3 and below.

Table 2.1 - Force measurement conditions in previous works

Work	Re	Fr	AR
Gonçalves et al. (2015)	10000–50000	0.07–0.361	0.1–2.0
Fukuoka et al. (2016)	28000, 51000, 79000	0.1	0.25–1.50
	112000, 206000, 317000	0.4	
	160000	0.20, 0.31, 0.57	
Benitz et al. (2016)	2900	0.65	0.875–19

2.3 Objective of this study

Following these previous studies, Sakata et al. (2018) measured eleven vertical planes for cylinders piercing the free-surface with Re=43000, Fr=0.311, AR=2.0 and 0.5 by PIV and reconstructed the three-dimensional structures around cylinders. This thesis includes other conditions. The goal of this PIV measurement study is to understand the 3D structures around the cylinders with low aspect ratio and the free-end effect.

In our interest cases, stationary cylinders with low aspect ratio piercing the free surface, there are three non-dimensionalized parameters to govern the fluid phenomenon, namely Re, Fr and AR. Although searching for previous studies, there is no work to evaluate the effect of Fr on hydrodynamic forces strictly, which means that the data was compared at the appropriate frequency range with moving only Fr independently while fixing Re and AR. In this study, since free-surface motion is characterized by the Froude number, nine cylinders with different diameters were prepared to test the effect of Froude number at the same Reynolds number, 43000. Different aspect ratios were tested for each cases. Making the diameter larger and the flow velocity smaller, the Froude number becomes closer to zero, which means the free-slip condition in CFD. The maximum Froude number tested

in this study was around 0.7, taking the real sea condition into consideration. By evaluating forces in streamwise and transverse directions as a function of Froude number, the effect of the free surface on hydrodynamic forces on circular cylinders with low aspect ratio piercing the free surface was discussed. And the difference of the free-surface effect in different aspect ratios was also discussed. If AR is smaller, the interaction effect between free end and free surface is supposed to be larger, and vice versa. Moreover, as the study to focus on the boundary conditions (Figure 2.2), another experiment was performed in a recirculating water channel to compare free-surface conditions and no-slip conditions, the same cases on the ground plane. This work differs from previous studies in that providing results more widely and processing them more strictly.

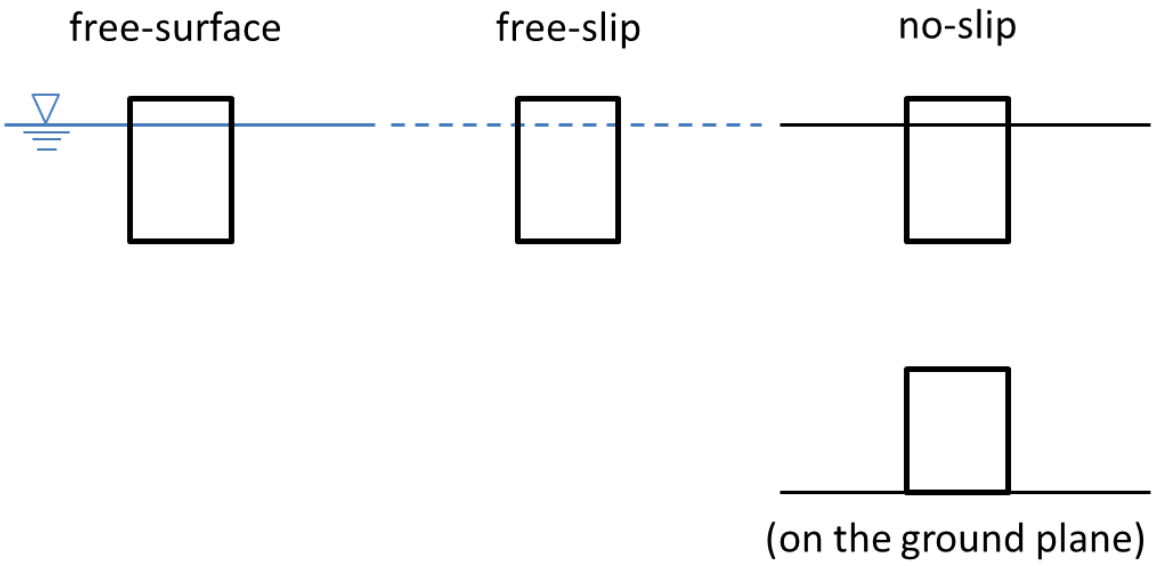

Figure 2.2 - Boundary conditions

Chapter 3 PIV measurement

3.1 Experimental setup

PIV measurements were carried out in a circulating water channel at the Reynolds number of 43,000 & 23,000 to understand the three-dimensional flow structures around the free end of the cylinders with low aspect ratio piercing the free surface. The circulating water channel is at the NDF – Fluid & Dynamics Research Group Laboratory facility of USP – University of Sao Paulo, Brazil, see Figure 3.1. The scale of the test section is 7500x700x700mm, and the flow has low levels of turbulence (less than 2%) with free-stream velocities up to 0.4m/s. Further details concerning the water channel can be found in Assi *et al.* (2005).

Stereo PIV measurements (velocity components in 3 directions) were carried out in a recirculating water channel to understand the 3D formations around the free end of the cylinders. 345 snapshots were acquired at a 15Hz sample frequency. Further details regarding the PIV facility can be found in Korkischko & Meneghini (2011). Four different aspect ratios were tested namely, AR=0.3, 0.5, 1.0 and 2.0 (where L is the submerged length of the cylinder and D is the diameter of the cylinder) at the Reynolds number of 43,000. The flow field in each case was 'sliced' vertically by D/10 at constant intervals to reveal the detailed 3D flow structure from the centerline of the cylinder until D/2 besides the cylinder. The number of slices was 11 in each case, and at least half diameter below the free end and around the cylinder was measured to comprise all the volume around each cylinder case. The number of velocity measurement point for each plane was 35×50. Furthermore, three different aspect ratios were tested namely, AR=L/D=0.5, 1.0, and 2.0 at the Reynolds number of 23000. The flow field in each case was 'sliced' horizontally by D/4 from the bottom of the cylinder. The total number of horizontal slices was 14. The number of velocity measurement point for each plane was 38×47. The flow characteristic at each planes was investigated.

Figure 3.2 shows the schematic diagram of vertical PIV measurement.

Eleven different vertical planes xz were measured. The acquired vertical planes were spaced 0.1 diameters each other from the cylinder center plane at $y/D = 0$ to $|y/D| = 1$. Due to the three-dimensional characteristic of the measurements, the velocities in the vertical plane xz and horizontal planes xy and yz can be evaluated (Figure 3.3). Figure 3.4 shows the schematic diagram of horizontal PIV measurement. Total 14 horizontal planes xy were measured. The acquired vertical planes were spaced 0.25 diameters from the bottom of the cylinder to near the free surface. The model was made of PVC – polyvinyl chloride with external diameter D=125mm. See details about the PIV setup and measurements in Figure 3.5.

Figure 3.1 - Circulating water channel at the NDF, USP from NDF HP

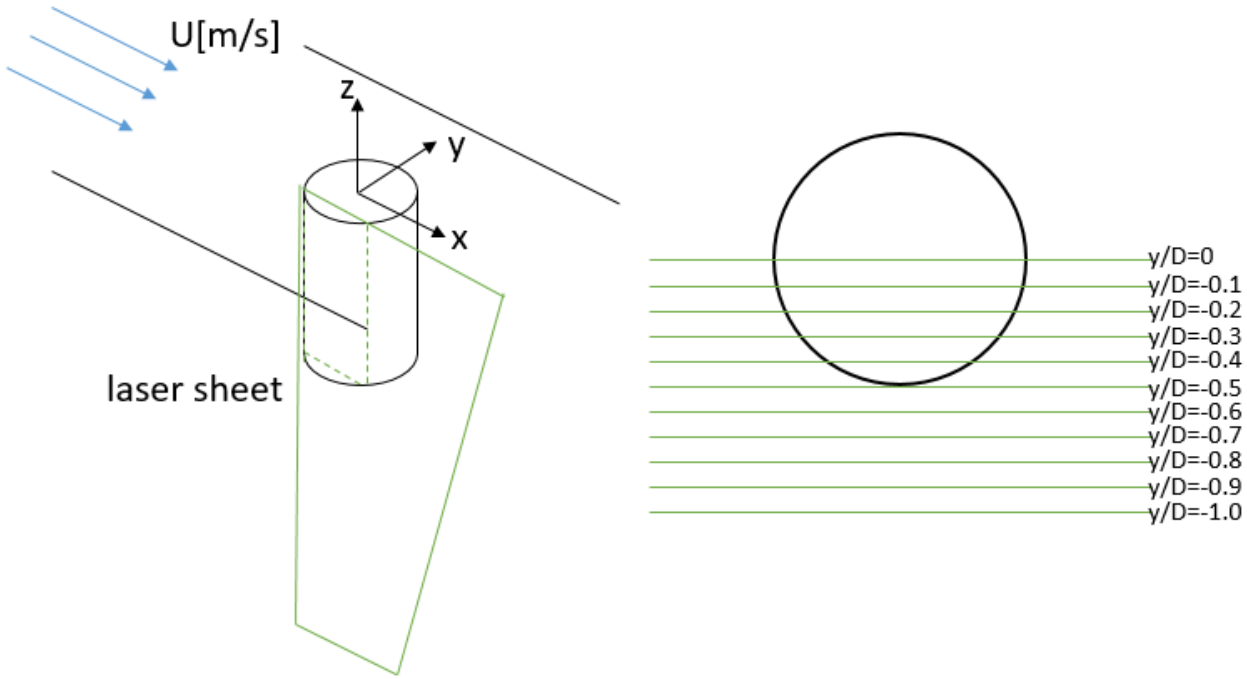

Figure 3.2 - Schematic diagram of horizontal PIV measurement and laser positions.

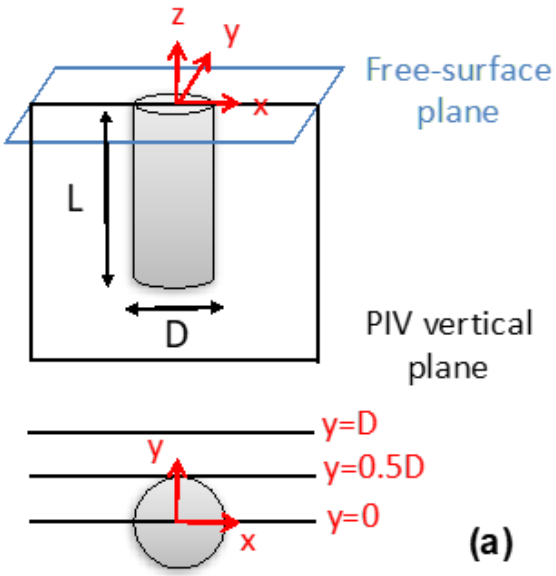

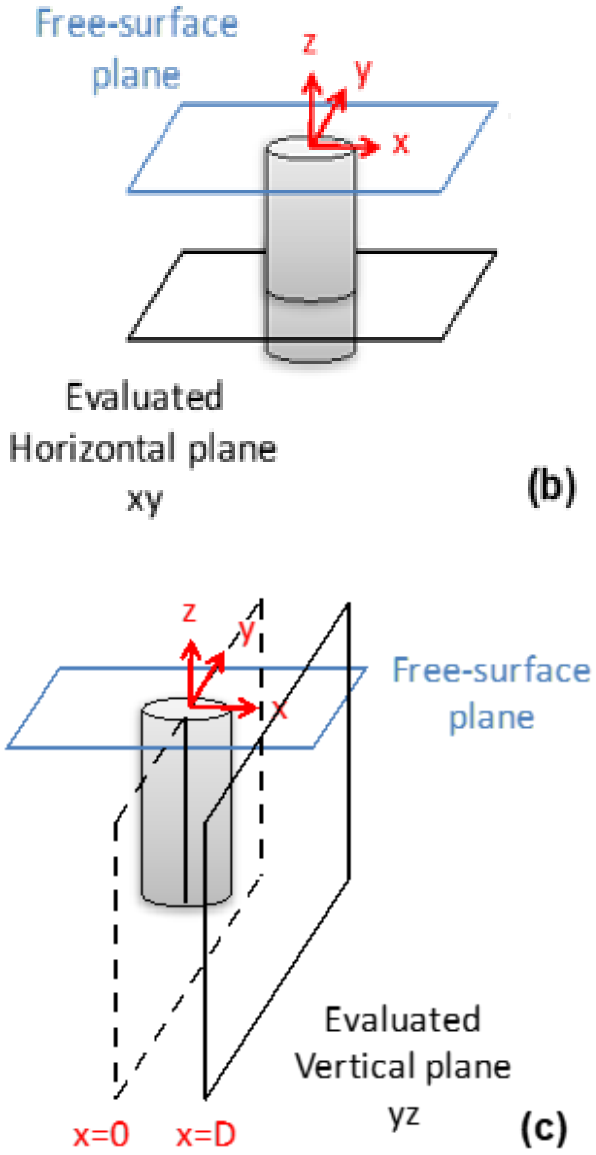

Figure 3.3 - (a) PIV measured plane xz; (b) evaluated horizontal plane xy; (c) evaluated vertical plane yz.

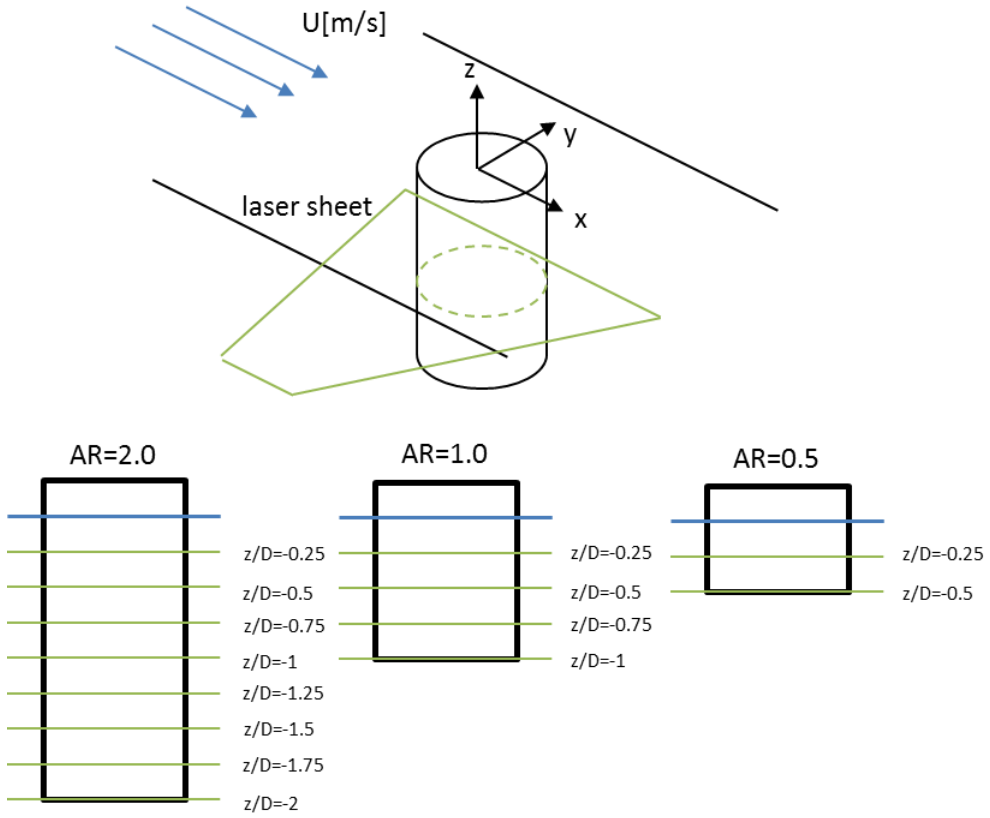

Figure 3.4 - Schematic diagram of horizontal PIV measurement and laser positions.

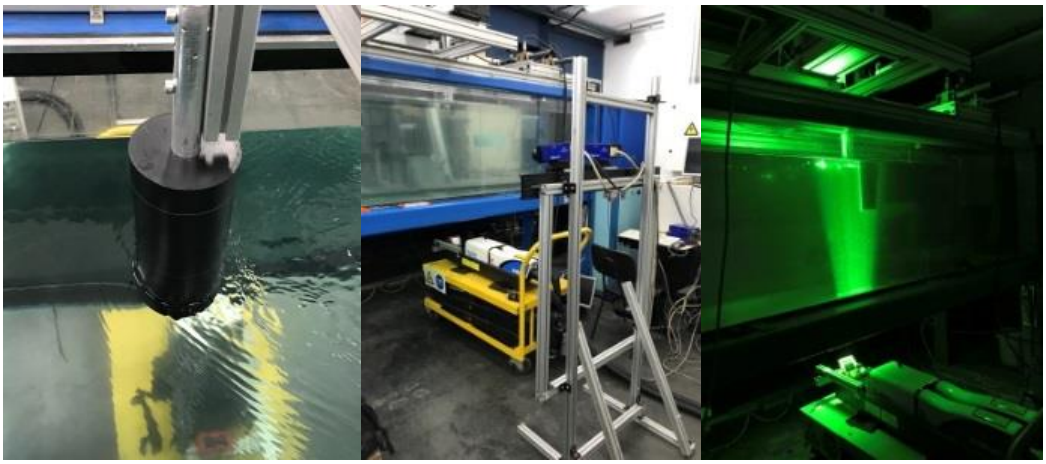

Figure 3.5 - Illustration of the stationary cylinder, the PIV measurement system and the PIV measurement in the vertical plane

3.2 Vertical PIV measurements

Time-averaged fields & root mean square fields

(a) Vertical planes xz

Selected flow field for Re=43000 for each aspect ratios was presented in Figure 3.6, 3.7, 3.8, and 3.9. In these figures, both the mean velocity field and the mean vorticity field are made dimensionless with the uniform flow velocity U=0.344m/s and the cylinder diameter D=0.125m. The white square means the position of the cylinder submerged and the top line, z/D=0 is the still water surface. In this PIV measurement, near the free surface was not able to be measured due to the reflection of water.

Figure 3.6 shows the time-averaged streamlines and contours of mean velocity component Vx/U in different vertical planes xz for L/D=2.0. At $|y/D|<0.6$, recirculation flow from the bottom of the cylinder can be observed. The transition of the recirculation core of each vertical plane is found. The other recirculation under the cylinder ($|x/D|<0.5$ and $z/D<-2.0$) disappears at $|y/D|>0.4$. At $|y/D|>0.6$, the regions of which region are less susceptible by the cylinder, the stream direction is almost the same as that of uniform flow.

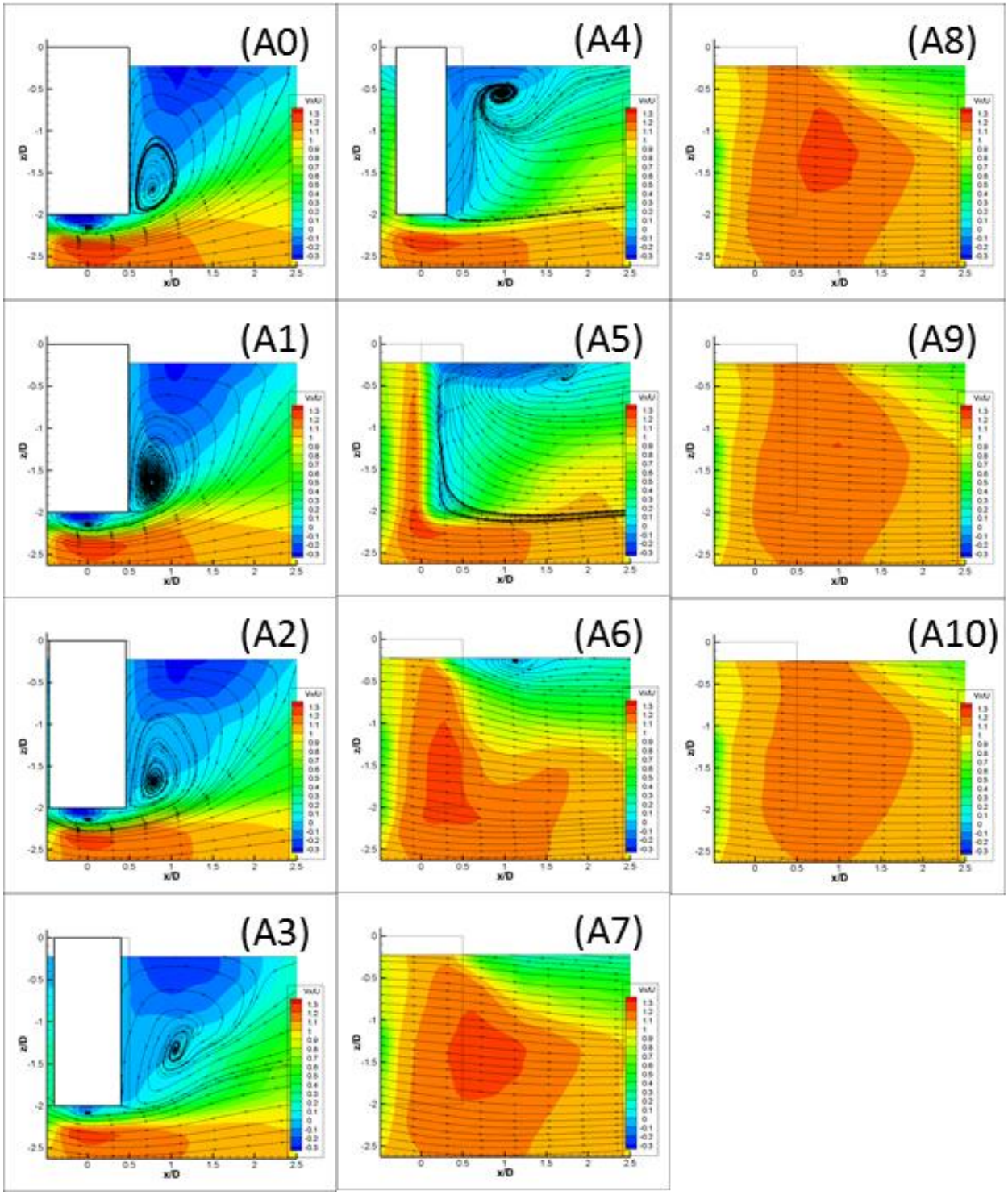

Figure 3.6 - Time-averaged streamlines and contours of mean velocity component Vx/U in the vertical planes xz for L/D=2.0 at Re=43000: (A0) y/D=0, (A1) |y/D|=0.1, (A2) |y/D|=0.2, (A3) |y/D|=0.3, (A4) |y/D|=0.4, (A5) |y/D|=0.5, (A6) |y/D|=0.6, (A7) |y/D|=0.7, (A8) |y/D|=0.8, (A9) |y/D|=0.9, (A10) |y/D|=1.0

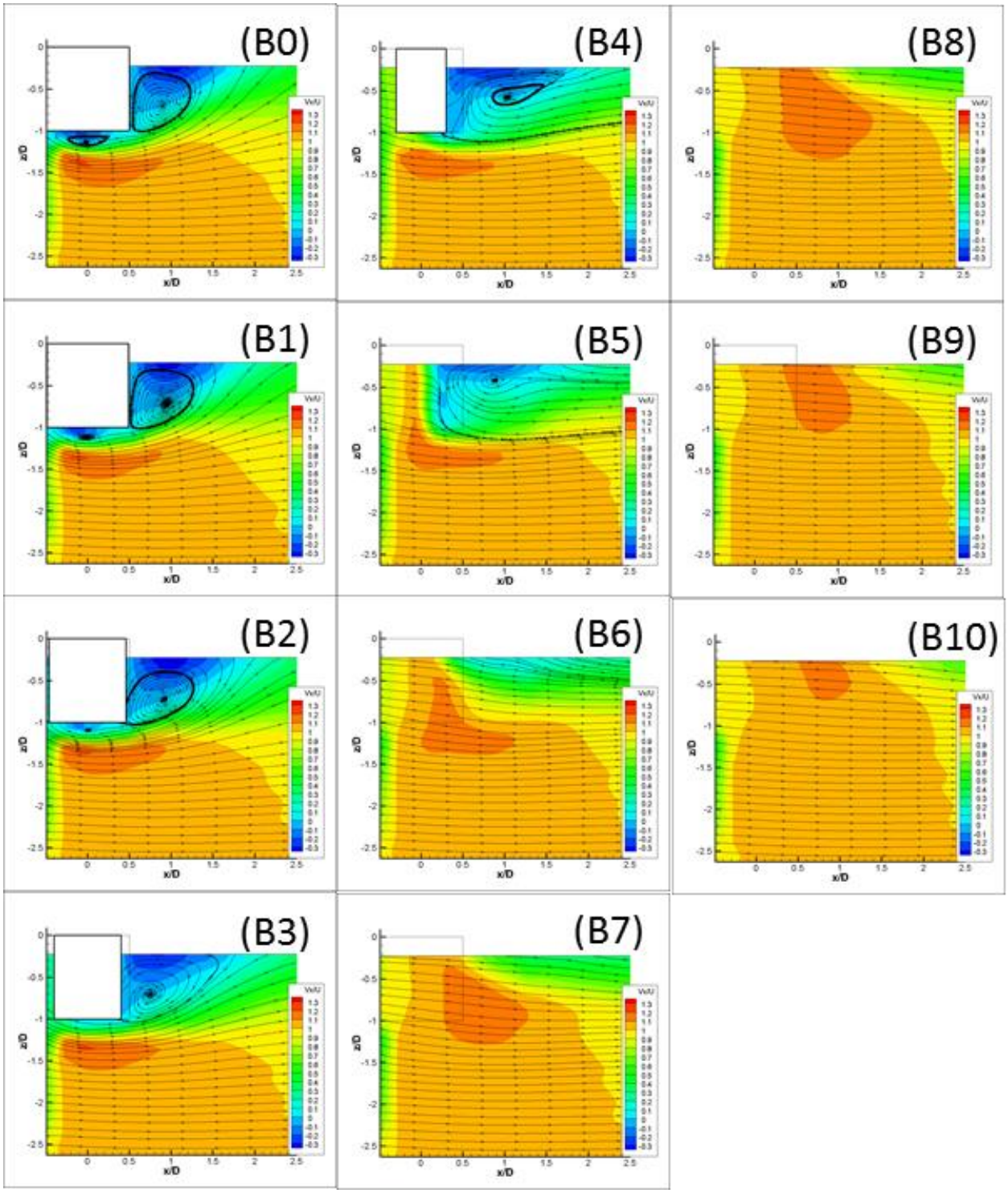

Figure 3.7 - Time-averaged streamlines and contours of mean velocity component Vx/U in the vertical planes xz for L/D=1.0 at Re=43000: (B0) y/D=0, (B1) |y/D|=0.1, (B2) |y/D|=0.2, (B3) |y/D|=0.3, (B4) |y/D|=0.4, (B5) |y/D|=0.5, (B6) |y/D|=0.6, (B7) |y/D|=0.7, (B8) |y/D|=0.8, (B9) |y/D|=0.9, (B10) |y/D|=1.0

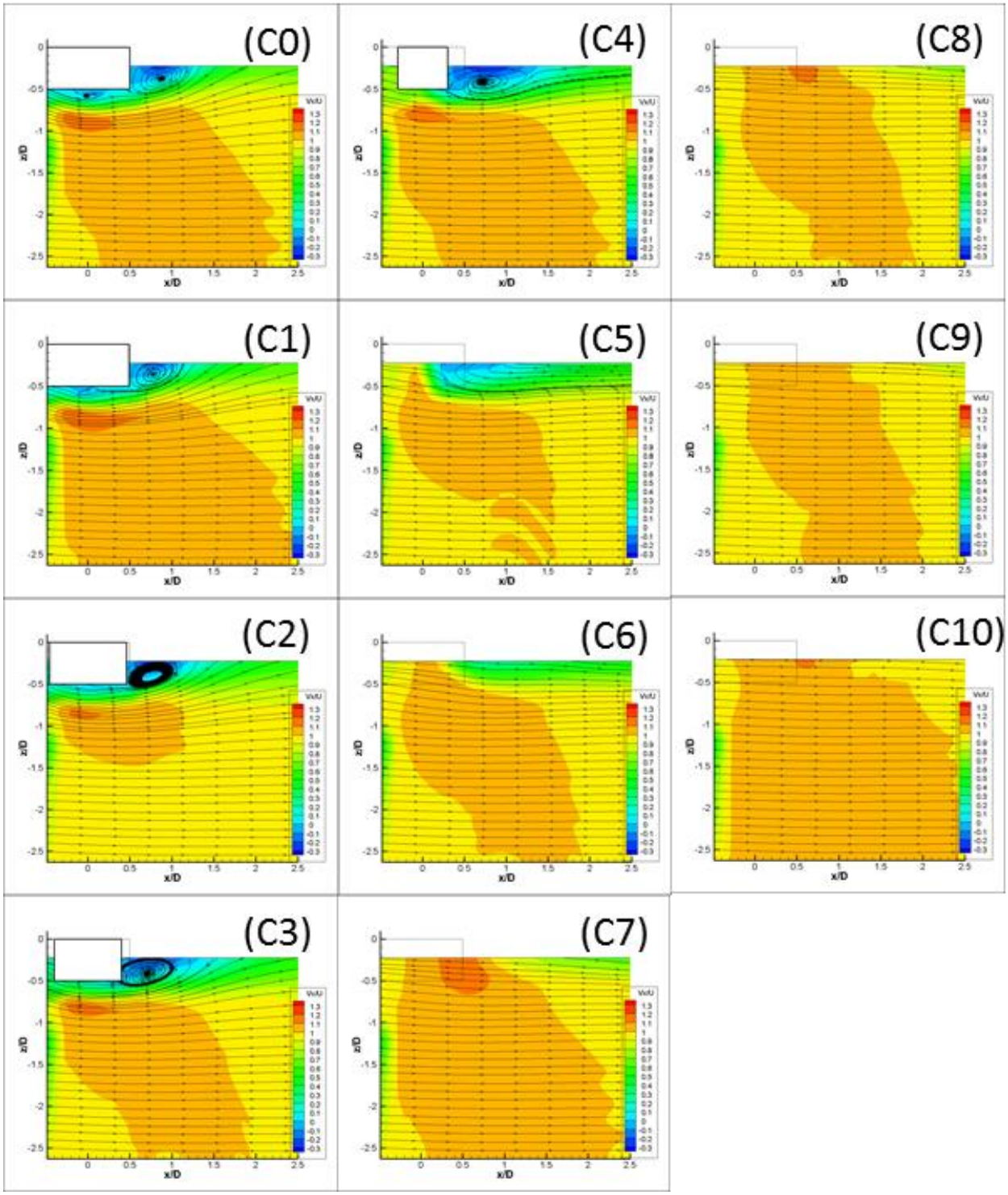

Figure 3.8 - Time-averaged streamlines and contours of mean velocity component Vx/U in the vertical planes xz for L/D=0.5 at Re=43000: (C0) y/D=0, (C1) |y/D|=0.1, (C2) |y/D|=0.2, (C3) |y/D|=0.3, (C4) |y/D|=0.4, (C5) |y/D|=0.5, (C6) |y/D|=0.6, (C7) |y/D|=0.7, (C8) |y/D|=0.8, (C9) |y/D|=0.9, (C10) |y/D|=1.0

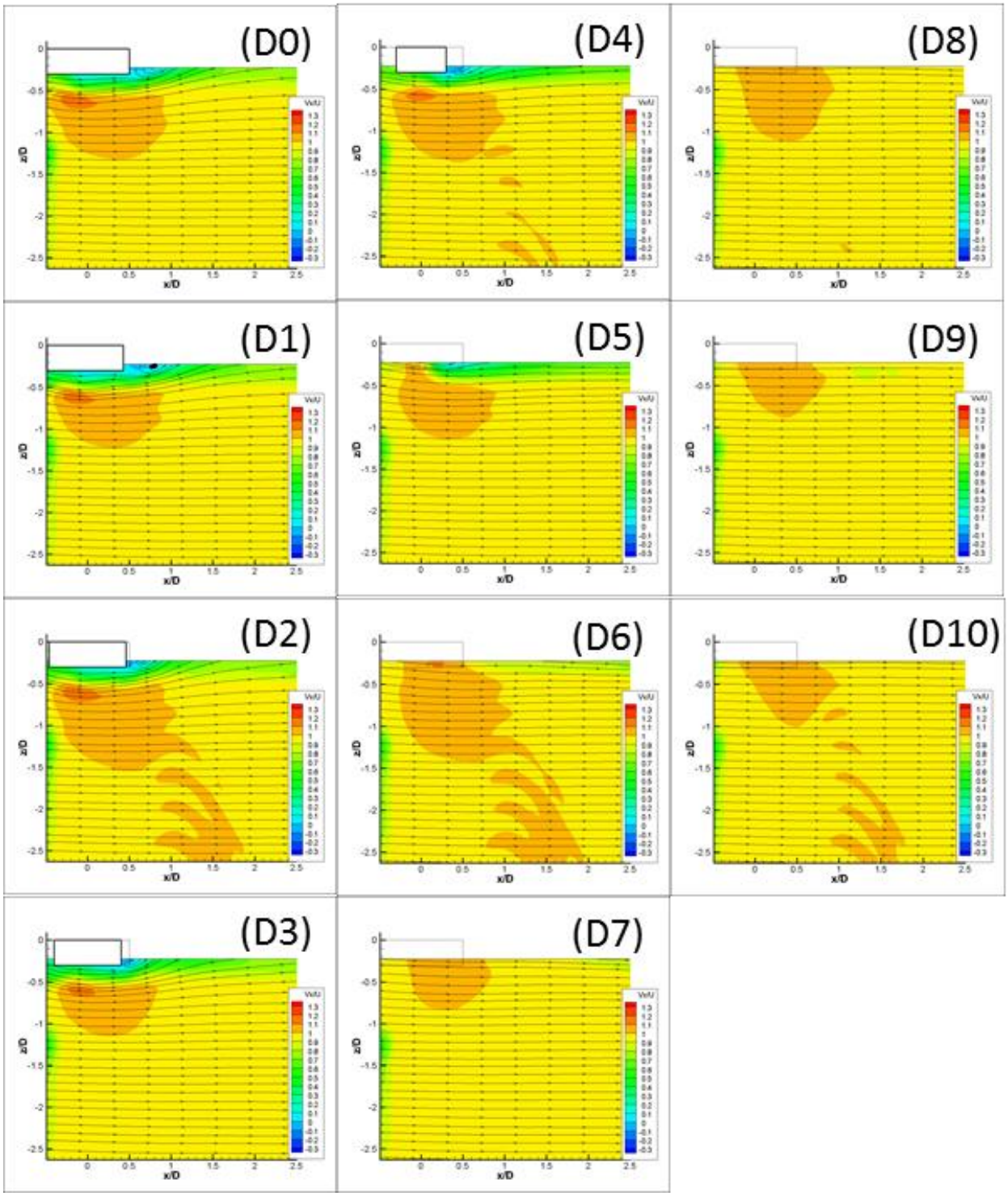

Figure 3.9 - Time-averaged streamlines and contours of mean velocity component Vx/U in the vertical planes xz for L/D=0.3 at Re=43000: (D0) y/D=0, (D1) |y/D|=0.1, (D2) |y/D|=0.2, (D3) |y/D|=0.3, (D4) |y/D|=0.4, (D5) |y/D|=0.5, (D6) |y/D|=0.6, (D7) |y/D|=0.7, (D8) |y/D|=0.8, (D9) |y/D|=0.9, (D10) |y/D|=1.0

Figure 3.7 - 3.9 show the time-averaged streamlines and contours of mean velocity component Vx/U in the vertical plane xz for L/D=1.0, 0.5, and 0.3. Unlike the case with the aspect ratio of 2.0, recirculation flow from the bottom of the cylinder can be observed only in $|y/D|<0.5$ for L/D=1.0 and in $|y/D|<0.4$ for L/D=0.5 and 0.3. The recirculation core in the wake of each vertical plane did not change so much at different planes. Positions of the core of longitudinal recirculation region behind the cylinder for all aspect ratios are presented in Table 3.1. The positions for L/D=2.0 and 0.5 are extracted and presented in Figure 3.10. The same type of comparison in the y/D=0 was presented by Palau-Salvador *et al.* (2010) for L/D=2.5 and 5.0, and by Gonçalves *et al.* (2013) for L/D=0.3, 0.5, 1.0, and 2.0, see Table 3.2. Results in Table 3.1 shows good agreement with results in Table 3.2. Moreover, the other recirculation under the cylinder ($|x/D|<0.5$ and $z/D<-0.5$) disappears at $|y/D|>0.2$.

Table 3.1 - Positions of the core of the longitudinal recirculation region behind the cylinders with different aspect ratios.

L/D	$\|y/D\|$	x/D	$\|z/D\|$	$\|z/L\|$
2	0	0.75	1.75	0.875
2	0.1	0.75	1.75	0.875
2	0.3	0.75	1.75	0.875
2	0.3	1.1	1.25	0.625
2	0.4	0.9	0.55	0.275
2	0.5	1.75	0.4	0.2
2	0.6	1.1	0.25	0.125
1	0	0.9	0.7	0.7
1	0.1	0.95	0.7	0.7
1	0.2	0.95	0.7	0.7
1	0.3	0.8	0.7	0.7
1	0.4	1.05	0.6	0.6
1	0.5	0.9	0.4	0.4
0.5	0	0.8	0.35	0.7
0.5	0.1	0.8	0.35	0.7
0.5	0.2	0.8	0.4	0.8
0.5	0.3	0.75	0.4	0.8
0.5	0.4	0.7	0.4	0.8
0.3	0	0.8	0.24	0.8
0.3	0.1	0.8	0.24	0.8
0.3	0.2	0.7	0.21	0.7
0.3	0.3	0.6	0.21	0.7
0.3	0.4	0.6	0.27	0.9

Table 3.2 - Positions of the core of the longitudinal recirculation region behind the cylinders in the function of aspect ratio
(reproduced from Gonçalves et al. (2013))

Work	L/D	$\|y/D\|$	x/D	$\|z/D\|$	$\|z/L\|$
Gonçalves et al. (2015)	0.3	0	0.8	0.2	0.7
	0.5	0	0.8-0.9	0.3	0.6
	1	0	0.9	0.6-0.7	0.6-0.7
	2	0	0.8-0.9	1.6	0.8
Palau-Salvador et al. (2010)	2.5	0	0.8	2	0.8
	5	0	0.9	4	0.8

Figure 3.11 shows contours of the mean transverse vorticity in the vertical planes xz. The vorticity was calculated by the following equation, see Figure 3.12 for details. Vorticities in other two directions were calculated in the same way.

$$\omega_y \ at \ (i,j) = \frac{V_{x_{i,j-1}} - V_{x_{i,j+1}}}{\Delta Z} - \frac{V_{z_{i+1,j}} - V_{z_{i-1,j}}}{\Delta X}$$

All aspect cases confirmed the vortex from the bottom at |y/D|<0.5. Although Gonçalves *et al.* (2015) presented the same cases as y/D=0, the value of this study is correct. The vortex from the bottom is gradually stretched out in the streamwise direction away from the centerline. On the other hand, at |y/D|>0.5, the vortex comes from the side of the cylinder. For L/D=2.0 and 1.0, the vortex shedding from the side is dragged to z-direction because the streamline direction is like Figure 3.6. Since there is separation from the side of the cylinder (see Figure 3.15), this fact suggests that the rotation axis of vortex shedding is inclined. This inclination is not confirmed for the cylinder on the ground plane and there is a possibility that the vortex from near the free-surface is suppressed by free-surface and inclined.

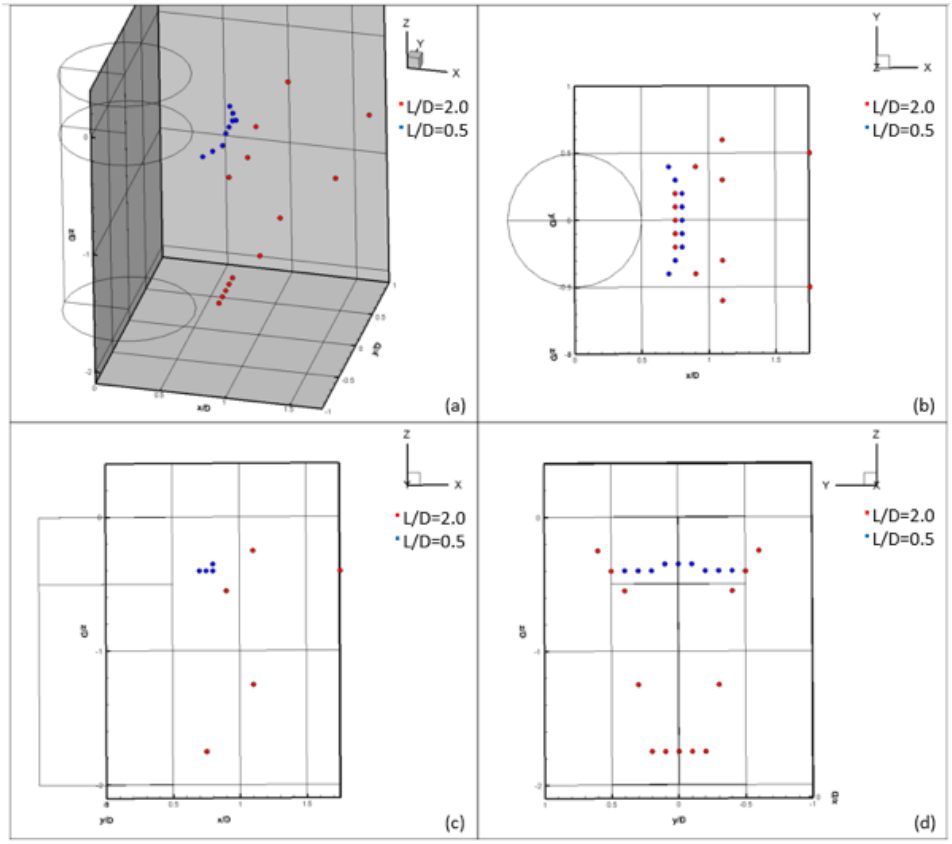

Figure 3.10 - Positions of the core of the longitudinal recirculation region behind the cylinders for Re=43000, (a) 3D (b) top view (c) side view (d)front view.

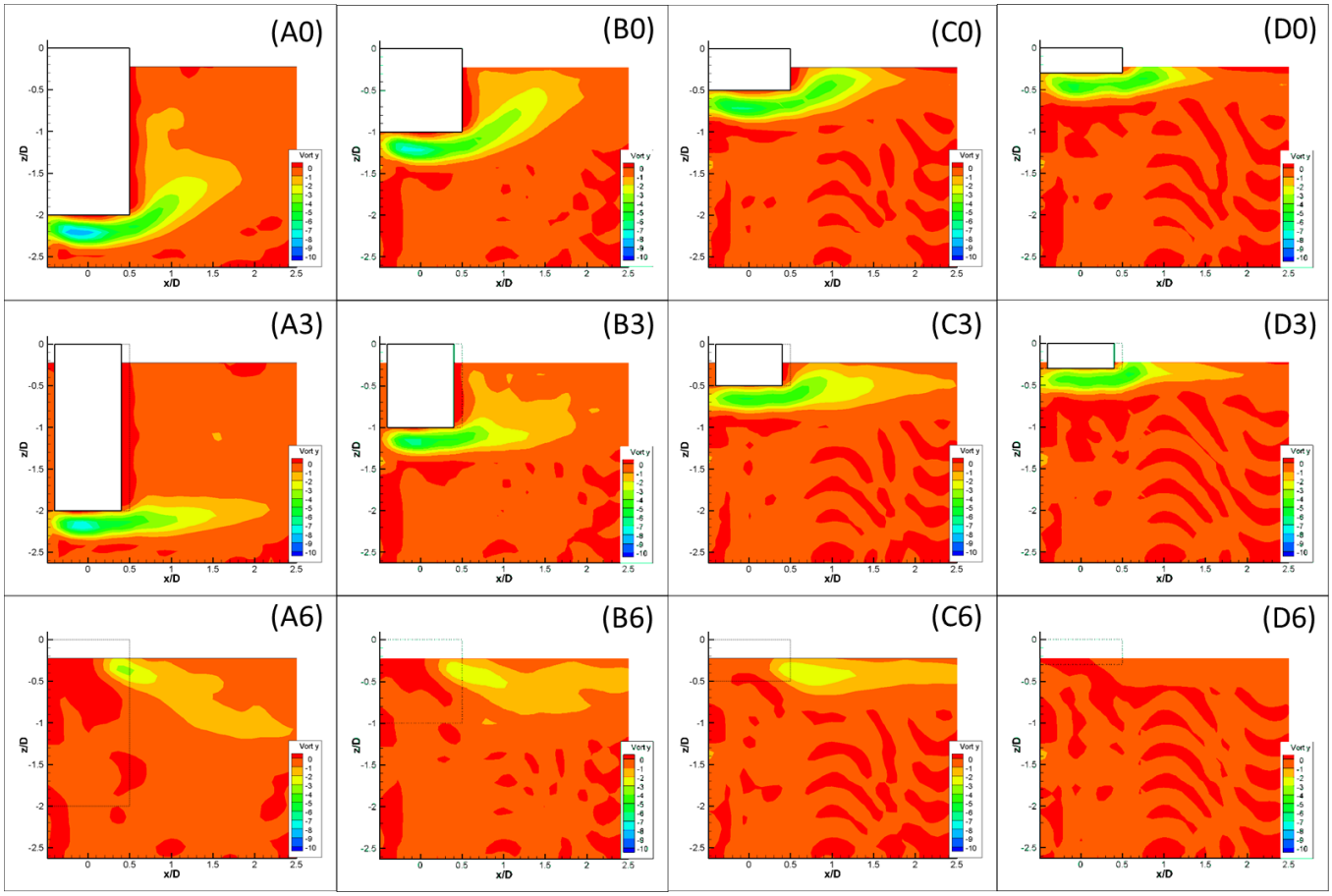

Figure 3.11 - Contours of mean transverse vorticity $\omega_y D/U$ in the vertical planes xz for Re=43000, L/D=2.0: (A0) y/D=0, (A3) y/D=-0.3, (A6) y/D=-0.6, L/D=1.0: (B0) y/D=0, (B3) y/D=-0.3, (B6) y/D=-0.6, L/D=0.5: (C0) y/D=0, (C3) y/D=-0.3, (C6) y/D=-0.6, L/D=0.3: (D0) y/D=0, (D3) y/D=-0.3, (D6) y/D=-0.6,

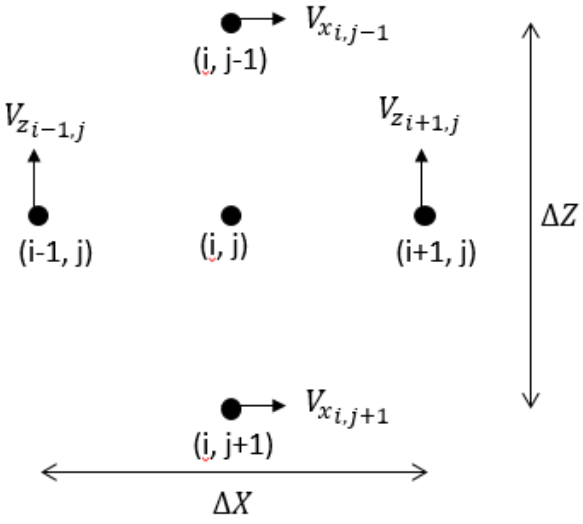

Figure 3.12 - Vorticity calculation model

Figure 3.13 and 3.14 show contours of root mean square of streamwise and transverse velocity fluctuations, RMS Vx/U and RMS Vz/U in the vertical planes xz. Each velocity fluctuation was calculated as root mean square of the deviation from time-averaged velocity. RMS Vx/U behind the cylinder for L/D=2.0 becomes larger away from the centerline. On the other hand, RMS Vz/U behind the cylinder becomes smaller away from the centerline. This is because, near the centerline, the vortex from the bottom is dominant, and away from the centerline, the streamwise velocity is strengthened by the separation from the side of the cylinder. As Palau-Salvador *et al.* (2010) pointed out for L/D=2.5, the elevated RMS Vx/U behind the cylinder at |y/D|=0 may be caused by an energy transfer from the much larger RMS Vz/U. This explanation is also true of the case at |y/D|=0.6.. The elevated RMS Vz/U behind the cylinder at |y/D|=0 may be caused by an energy transfer from the much larger RMS Vx/U. The high-velocity fluctuations behind the cylinder are not aligned with the shear layer bordering the longitudinal recirculation region. Comparing with two aspect ratio cases namely, L/D=2.0 and 0.5 in|y/D|=0.6, the value of L/D=2.0 behind the cylinder was larger than that of L/D=0.5 because of the Karman vortex shedding. For L/D=0.5, at |y/D|=0 and 0.3, the high-velocity fluctuations behind the cylinder are aligned with the shear layer bordering the longitudinal recirculation region. Unlike the cases of L/D=2.0, the velocity fluctuations behind the cylinder of |y/D|=0.3 are higher than that of |y/D|=0. At |y/D|=0.6, the high-velocity fluctuations behind the cylinder are aligned with the separation from the side of the cylinder.

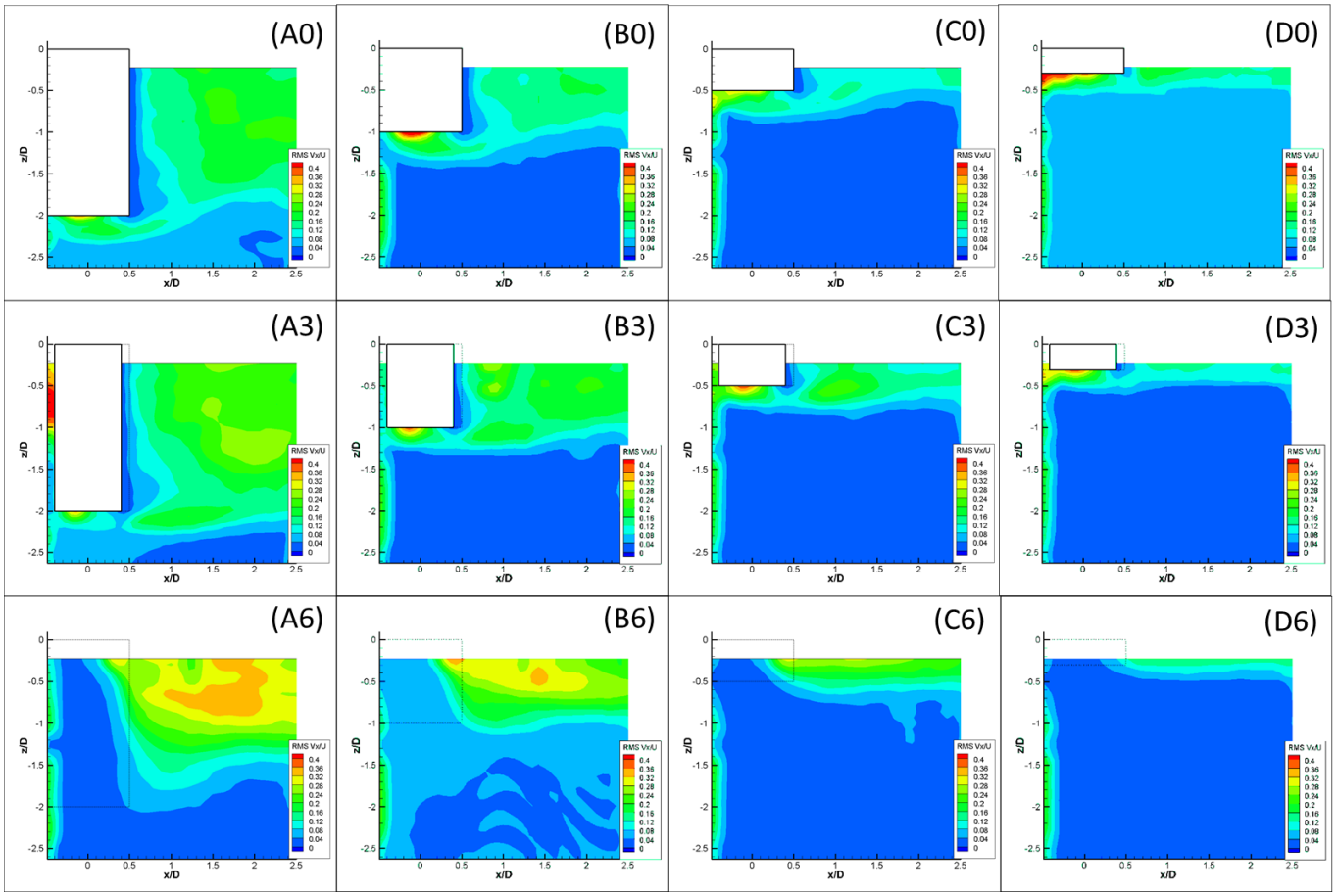

Figure 3.13 - Contours of root mean square of streamwise fluctuations RMS Vx/U in the vertical planes xz for Re=43000, L/D=2.0: (A0) y/D=0, (A3) y/D=-0.3, (A6) y/D=-0.6, L/D=1.0: (B0) y/D=0, (B3) y/D=-0.3, (B6) y/D=-0.6, L/D=0.5: (C0) y/D=0, (C3) y/D=-0.3, (C6) y/D=-0.6, L/D=0.3: (D0) y/D=0, (D3) y/D=-0.3, (D6) y/D=-0.6.

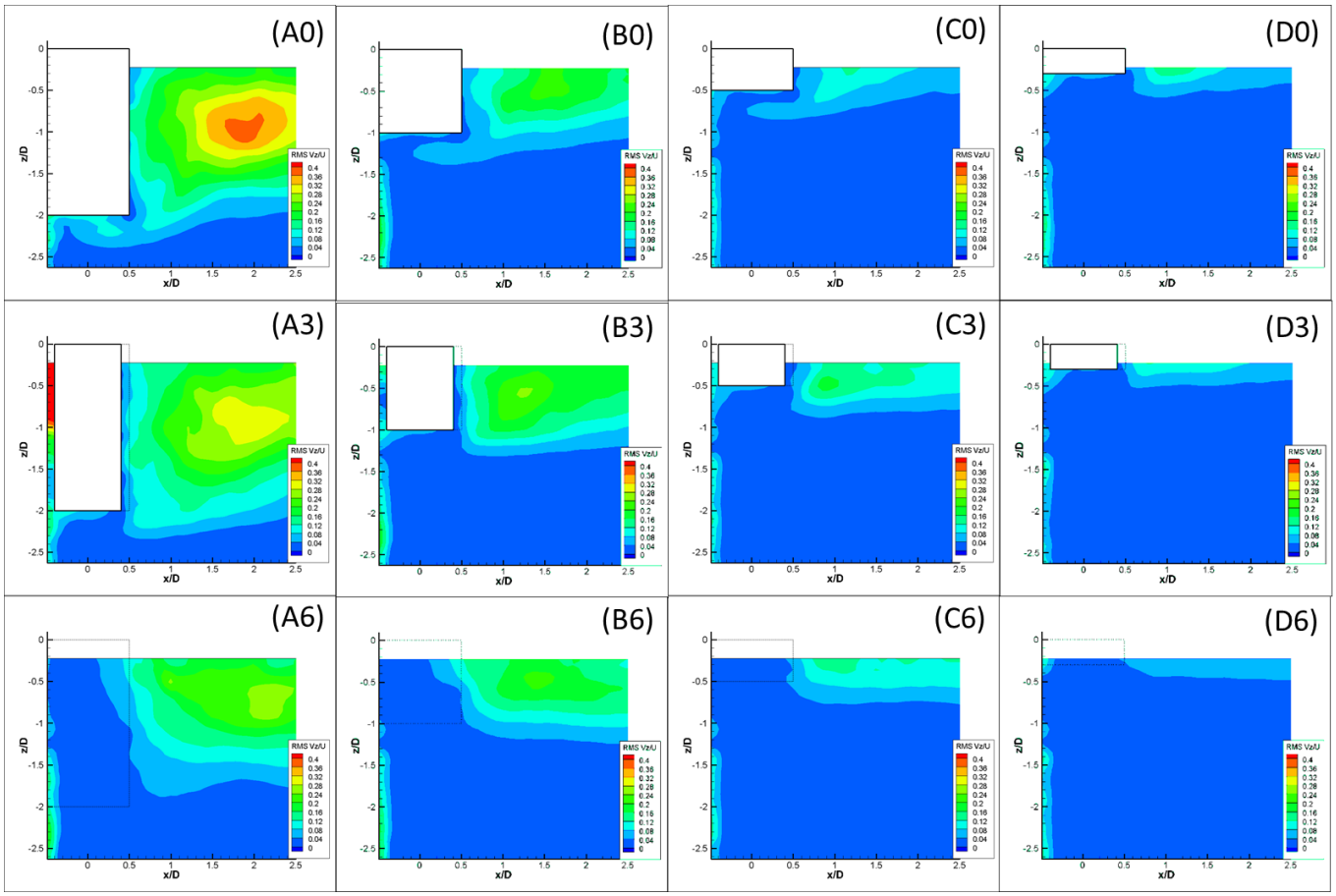

Figure 3.14 - Contours of root mean square of vertical fluctuations RMS Vz/U in the vertical planes xz for Re=43000, L/D=2.0: (A0) y/D=0, (A3) y/D=-0.3, (A6) y/D=-0.6, L/D=1.0: (B0) y/D=0, (B3) y/D=-0.3, (B6) y/D=-0.6, L/D=0.5: (C0) y/D=0, (C3) y/D=-0.3, (C6) y/D=-0.6, L/D=0.3: (D0) y/D=0, (D3) y/D=-0.3, (D6) y/D=-0.6.

(b) Horizontal planes xy

Figure 3.15 shows contours of the mean vertical vorticity in the vertical planes xz at different horizontal slices. Separation can be confirmed for each aspect ratio vertically from z/D=-0.23 (near the free surface) to the end of each cylinder.

(c) Vertical planes yz

Figure 3.16 and 3.17 show contours of the mean vertical vorticity in the vertical planes yz at x/D=0 and 0.5. The red contour vorticity below the bottom of the cylinder means trailing vortex. For L/D=0.3, the trailing vortex cannot be confirmed. On the other hand, the blue contour vorticity beside the

cylinder is the tip vortex from the corner of the bottom. As it can be seen from this figure, the rotating direction of the trailing vortex is opposite to the directions of the tip vortex. Thus, the trailing vortex is considered to be induced by the blue contour vortices. The blue contour vorticity below the cylinder is included in the vortex from the bottom in Figure 3.11.

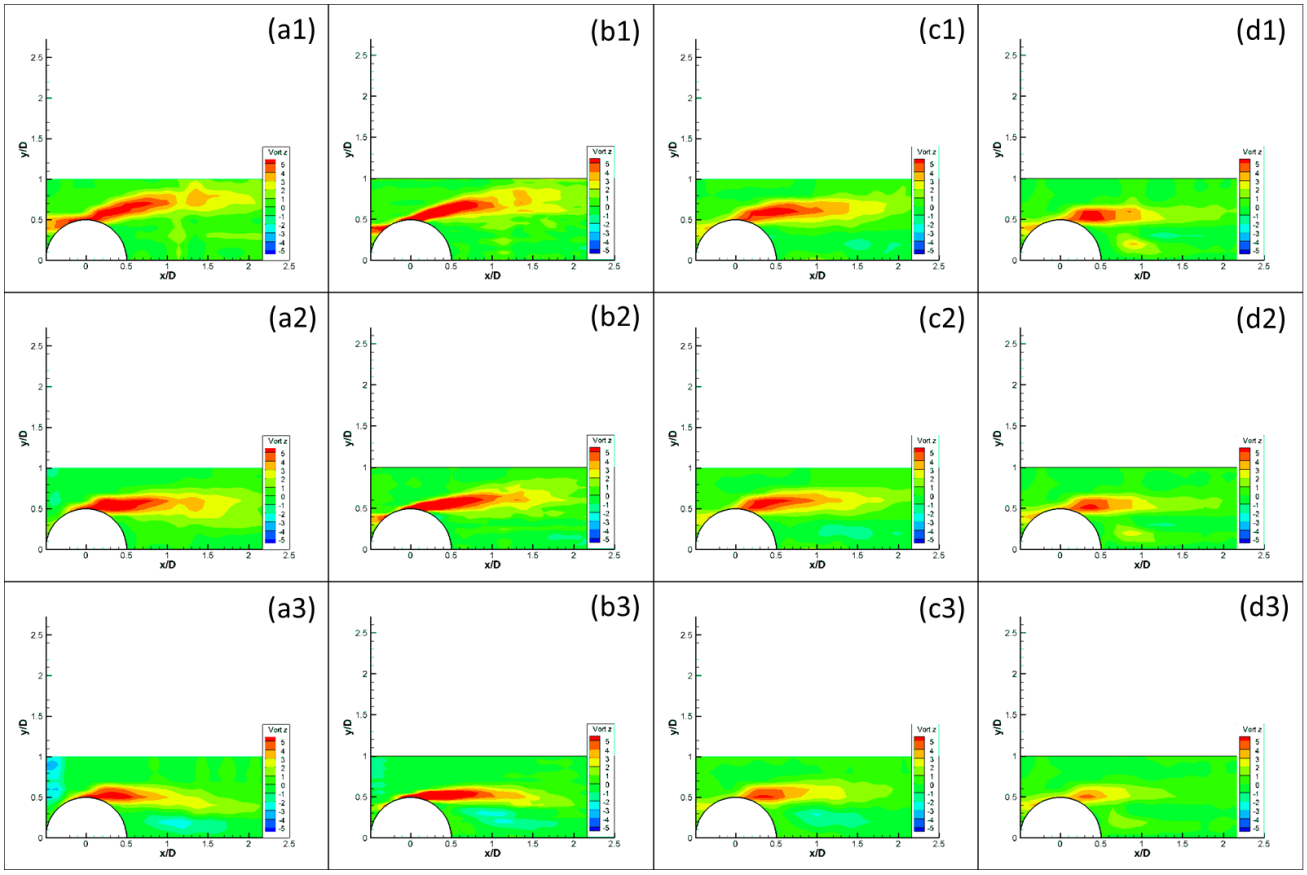

Figure 3.15.- Contours of mean vertical vorticity $\omega_z D/U$ in the horizontal planes xy at Re=43000, L/D=2.0: (a1) z/D=-0.23, (a2) z/D=-1.0, (a3) z/D=-2.0, L/D=1.0: (b1) z/D=-0.23, (b2) z/D=-0.51, (b3) z/D=-1.0, L/D=0.5: (c1) z/D=-0.23, (c2) z/D=-0.37, (c3) z/D=-0.51, L/D=0.3: (d1) z/D=-0.23, (d2) z/D=-0.3, (d3) z/D=-0.37.

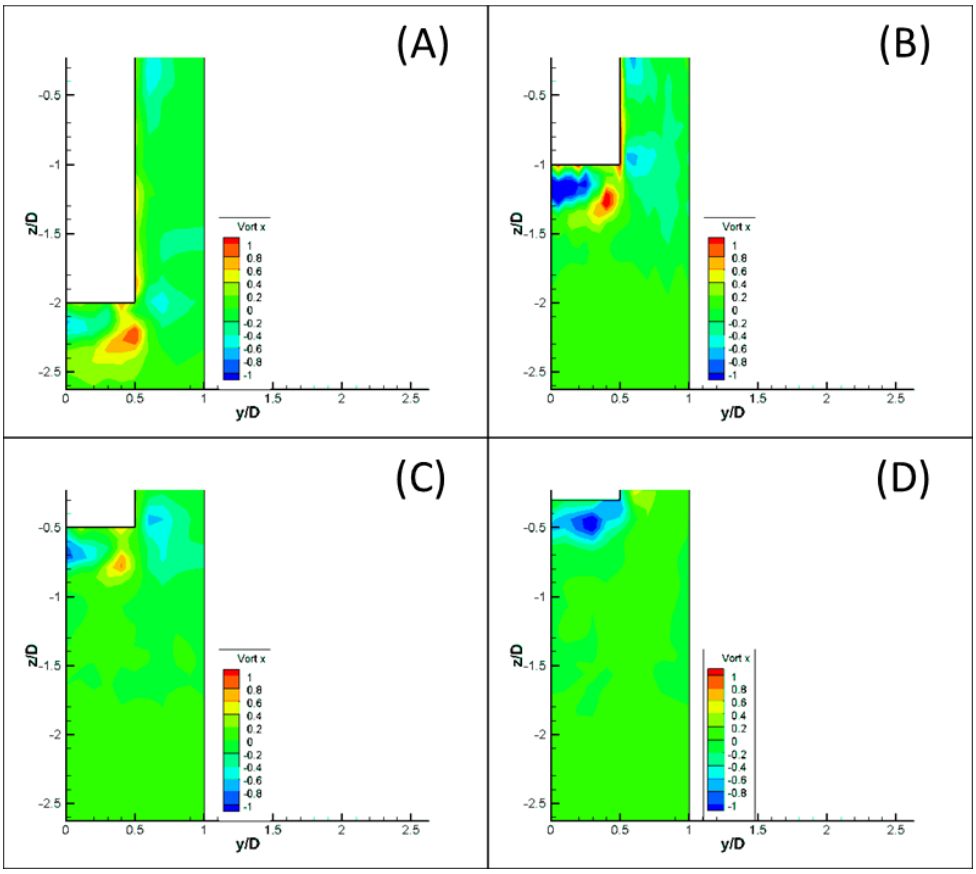

Figure 3.16.- Contours of mean streamwise vorticity $\omega_x D/U$ in the horizontal planes yz (x/D=0) at Re=43000 for (A) L/D=2.0, (B) L/D=1.0, (C) L/D=0.5 and (D) L/D=0.3.

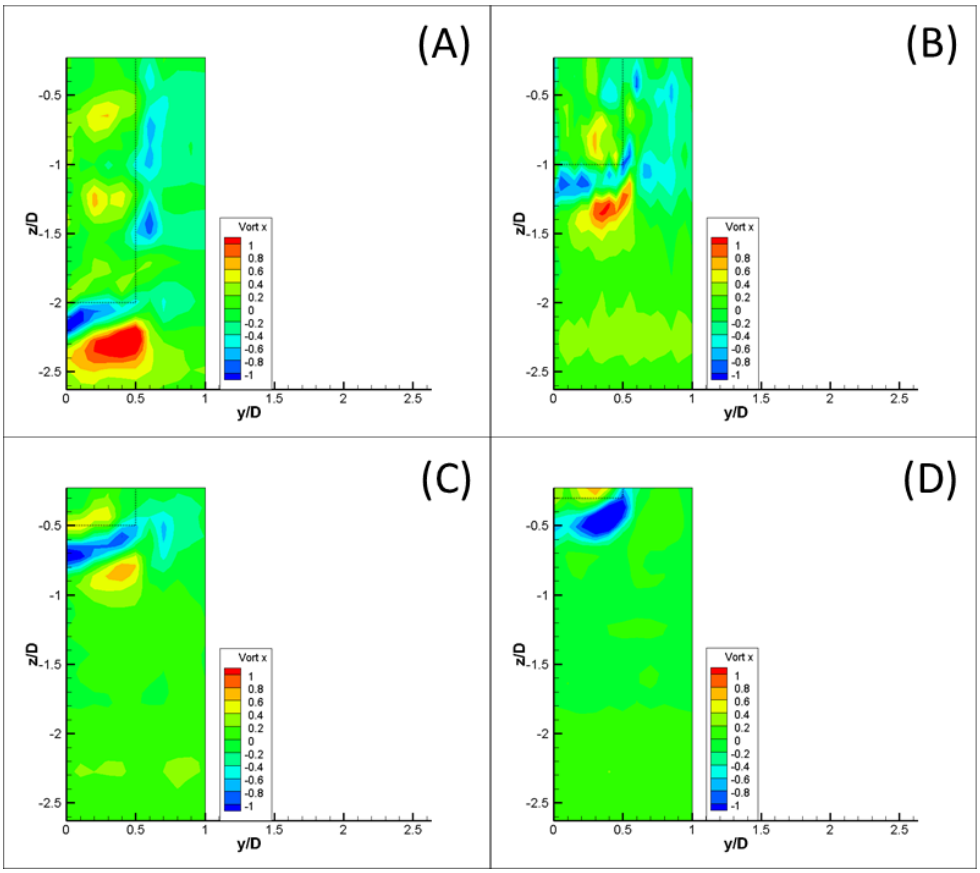

Figure 3.17 - Contours of mean vertical vorticity $\omega_x D/U$ in the horizontal planes yz (x/D=0.5) at Re=43000 for (A) L/D=2.0, (B) L/D=1.0, (C) L/D=0.5 and (D) L/D=0.3

3D flow structures

Since each vertical PIV plane has three velocity components, three-dimensional flow fields can be constructed. However, each plane was measured independently, and three-dimensional flow fields are time-averaged fields.

Figure 3.18 shows iso-surfaces of non-dimensionalized mean vorticity magnitude at 3.5 for L/D=2.0. Inside the green color area, the dimensionless vorticity is bigger than 3.5. Figure 3.19 shows iso-surfaces of non-dimensionalized mean vorticity magnitude at 3.5 for L/D=1.0. Inside the light blue color area, the dimensionless vorticity is bigger than 3.5. Figure 3.20 shows iso-surfaces of non-dimensionalized mean vorticity magnitude at 3.5 for L/D=0.5. Inside the yellow, green color area, the dimensionless vorticity is higher than 3.5. Figure 3.21 shows iso-surfaces of non-dimensionalized mean vorticity magnitude at 3.5 for L/D=0.5. Inside the yellow, green color area, the dimensionless vorticity is higher than 3.5. For all aspect ratio cases, separation and the arch-type vortex structure were confirmed.

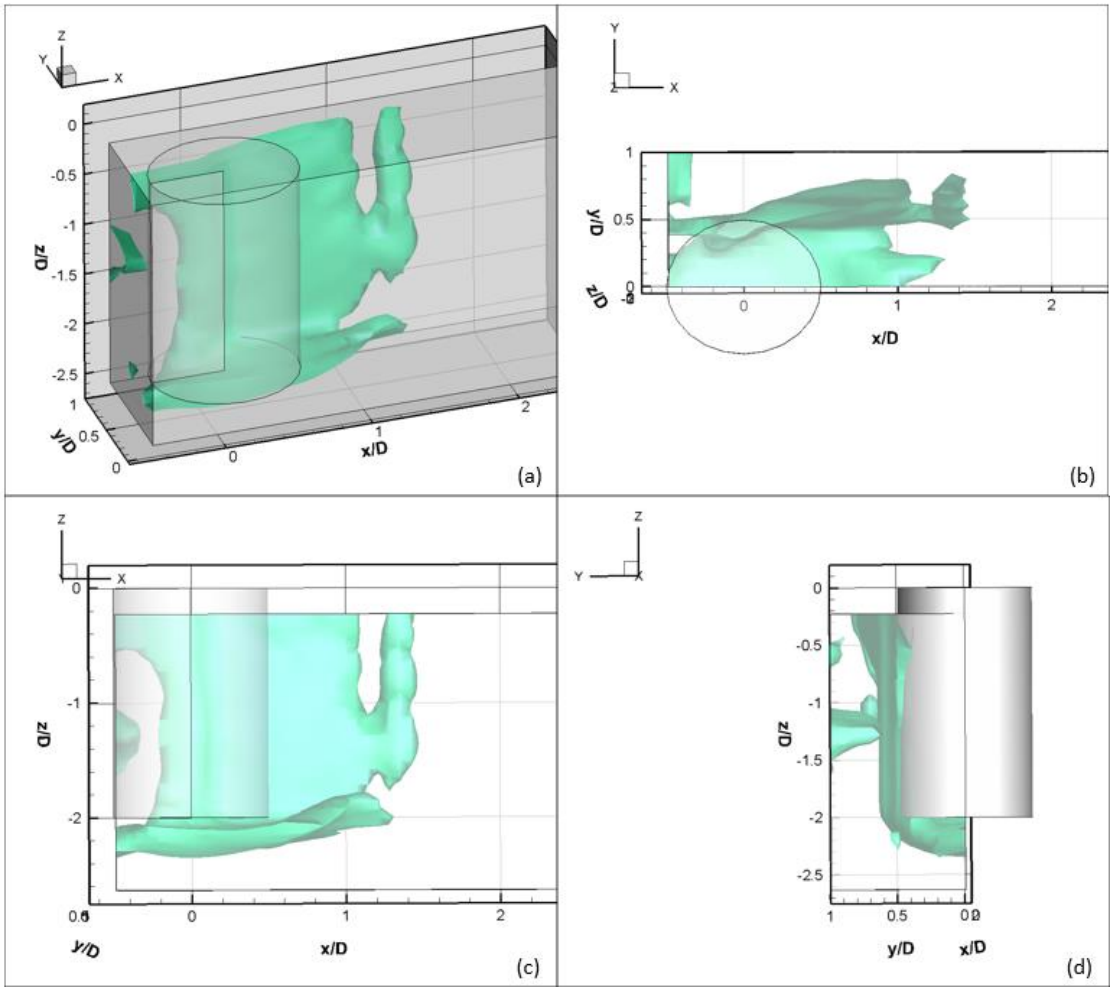

Figure 3.18.- Iso-surfaces of non-dimensionalized mean magnitude of vorticity vector at 3.5 for Re=43000, L/D=2.0: (a) 3D (b) top view (c) side view and (d) front view.

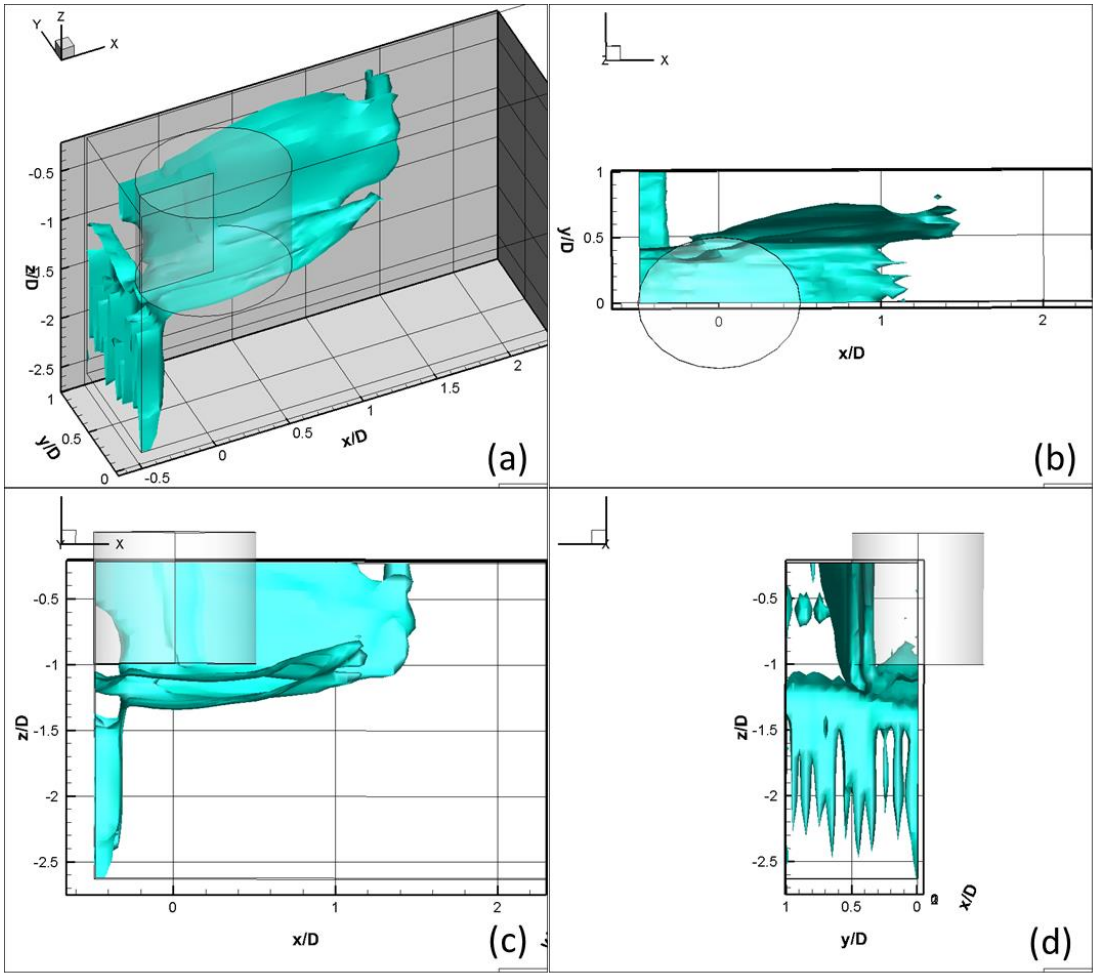

Figure 3.19 - Iso-surfaces of non-dimensionalized mean magnitude of vorticity vector at 3.5 for Re=43000, L/D=1.0: (a) 3D (b) top view (c) side view and (d) front view.

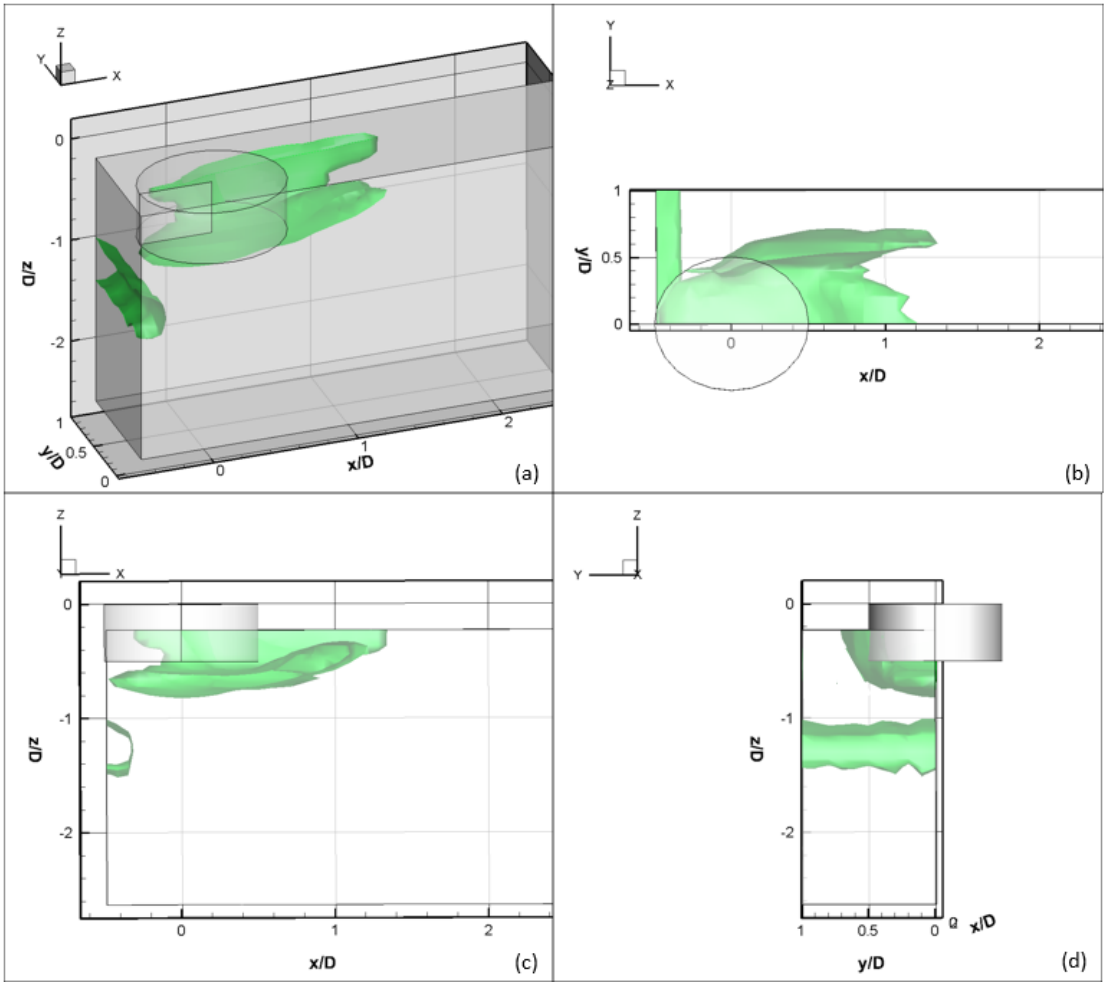

Figure 3.20.- Iso-surfaces of non-dimensionalized mean magnitude of vorticity vector at 3.5 for Re=43000, L/D=0.5: (a) 3D (b) top view (c) side view and (d) front view.

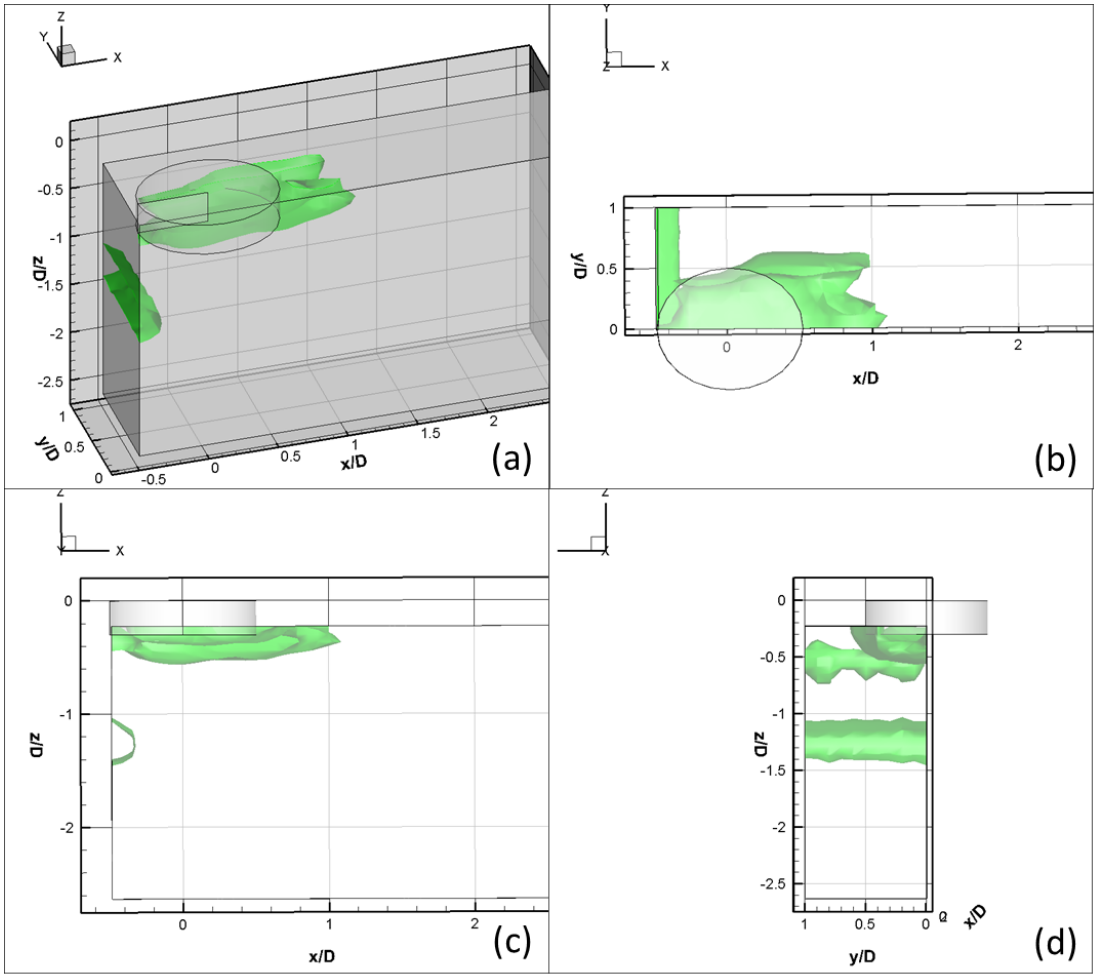

Figure 3.21 - Iso-surfaces of non-dimensionalized mean magnitude of vorticity vector at 3.5 for Re=43000, L/D=0.3: (a) 3D (b) top view (c) side view and (d) front view.

Figure 3.22 shows iso-surfaces of non-dimensionalized mean streamwise vorticity at 1 for (A) L/D=2.0 and at 0.6 for (B) L/D=1.0, (C) L/D=0.5, and (D) L/D=0.3. Inside the blue color area, the dimensionless vorticity is bigger than each value. This streamwise vortex is supposed to be the trailing vortex, and it seems remarkable for L/D=2.0. However, the value at x/D>1 is supposed to be caused by the elevated RMS Vz/U in Figure 3.14. The value of L/D=0.3 is small as mentioned earier.

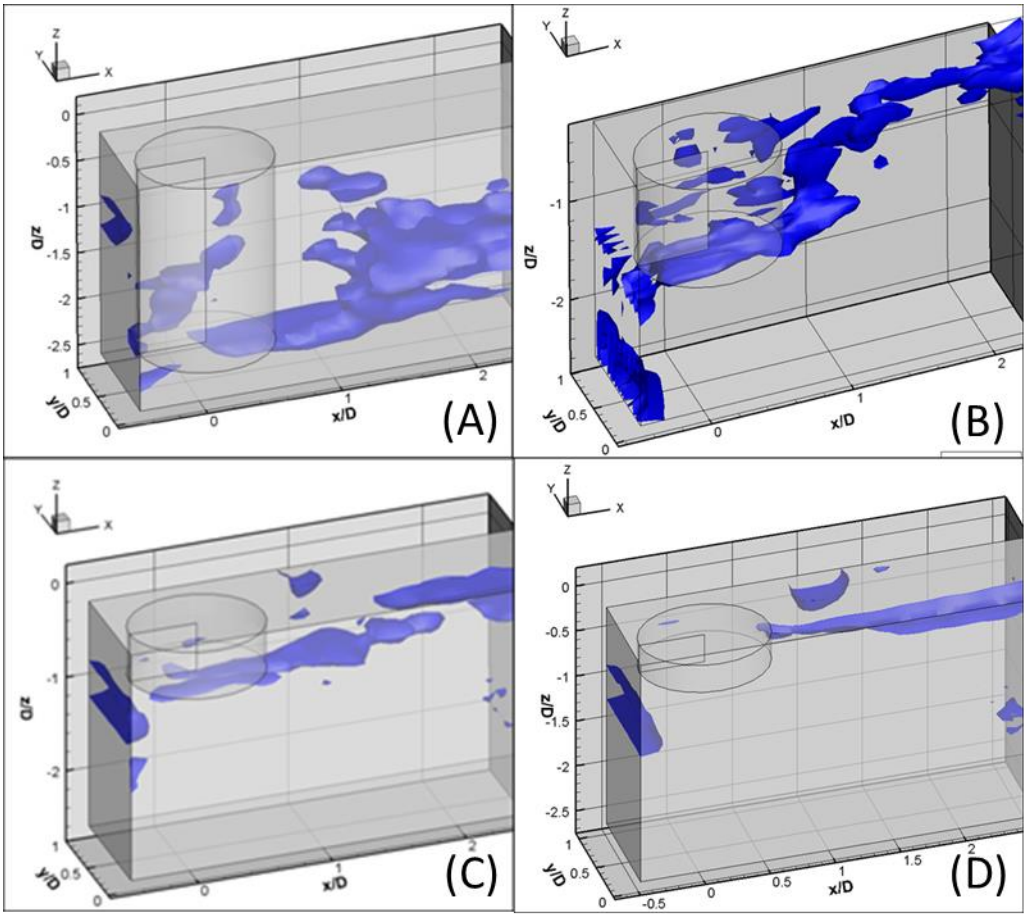

Figure 3.22.- Iso-surfaces of non-dimensionalized mean streamwise vorticity at 1 for (A) L/D=2.0 and at 0.6 for (B) L/D=1.0, (C)L/D=0.5, (D)L/D=0.3.

Fast Fourier Transformation analysis

To better understand the dynamics of the wake, FFT analysis was conducted. Vortex shedding frequency cannot be evaluated correctly only by this PIV measurement. Instead of evaluating time series vorticity directly, streamwise velocity is processed by FFT, and 'f' is defined as the frequency.

Figure 3.23 shows the power spectrum densities of the streamwise velocity of the non-dimensionalized streamwise velocity at different z/D positions as a function of non-dimensionalized frequency fD/U at x/D=2.5, |y/D|=0.6, for (A) L/D=2.0, (B) L/D=1.0, (C) L/D=0.5, (D) L/D=0.3. This frequency can be regarded as that of von Karman vortex shedding from the side of the cylinder. The positions of velocity processed by FFT is presented in Figure 3.24.
The case of L/D=2.0 has a strong peak around fD/U=0.13 at z/D>-0.6, which frequency is supposed to correspond to the von Karman vortex shedding from the side. And the strong peak gradually disappears alongside z/D<-0.6. This is because of the free-end effect. On the other hand, the case of L/D=0.5 has a very weak peak around fD/U=0.18 at z/D>-0.5. This suggests that for L/D=0.5, the von Karman vortex shedding cannot be confirmed clearly, affected by the flow from the free end. This frequency is considered to be the result of interference by both separation from the side of the cylinder and the vortex shedding from the bottom. This is also true of L/D=1.0. For L/D=0.3, there is quite a little peak and no periodic vortex shedding.

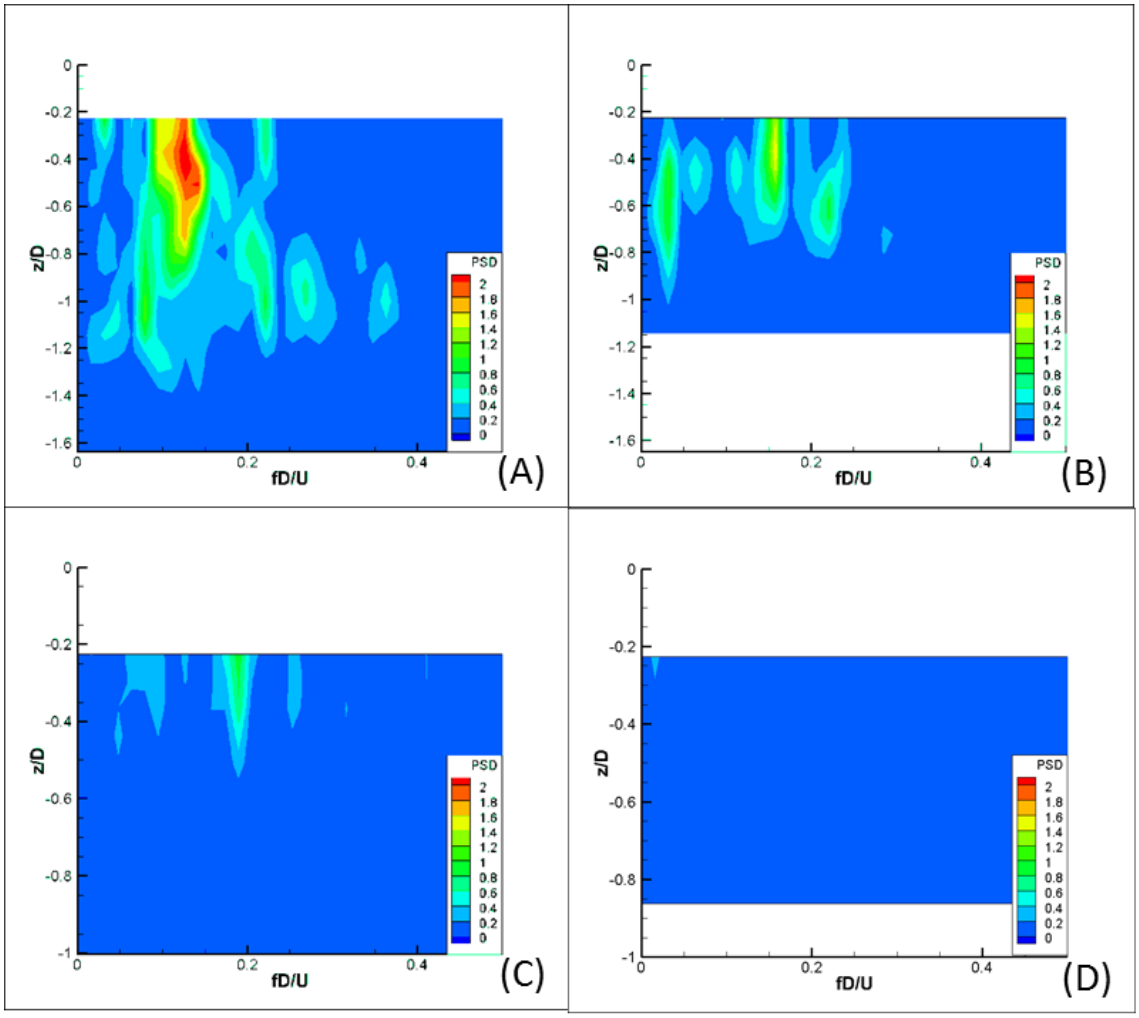

Figure 3.23.- PSD of the non-dimensionalized streamwise velocity as a function of fD/U at x/D=2.5, |y/D|=0.6, (A) L/D=2.0, (B) L/D=1.0, (C) L/D=0.5, (D) L/D=0.3

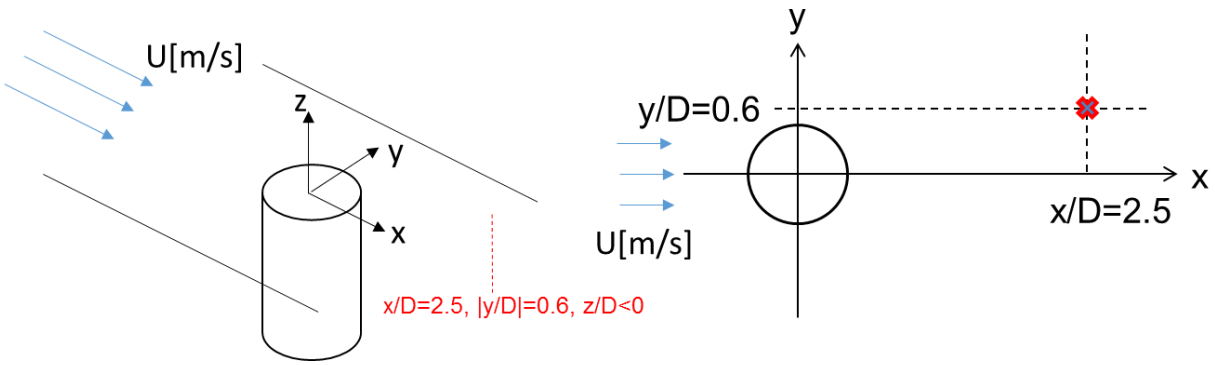

Figure 3.24 - Points at x/D=2.5, |y/D|=0.6

Figure 3.25 shows the power spectrum densities of the streamwise velocity of the non-dimensionalized streamwise velocity at different y/D positions as a function of non-dimensionalized frequency fD/U at x/D=2.5, z/D=-0.3 (near the free surface), for (A) L/D=2.0, (B) L/D=1.0, (C) L/D=0.5, (D) L/D=0.3. The positions of velocity processed by FFT is presented in Figure 3.26. At |y/D|>0.5, there are strong peaks for L/D=2.0 and weak peaks for L/D=0.5. This means that at |y/D|>0.5, there is the von Karman vortex shedding for L/D=2.0 and 1.0, but it cannot be concluded that there is also the von Karman vortex shedding for L/D=0.5 and 0.3.

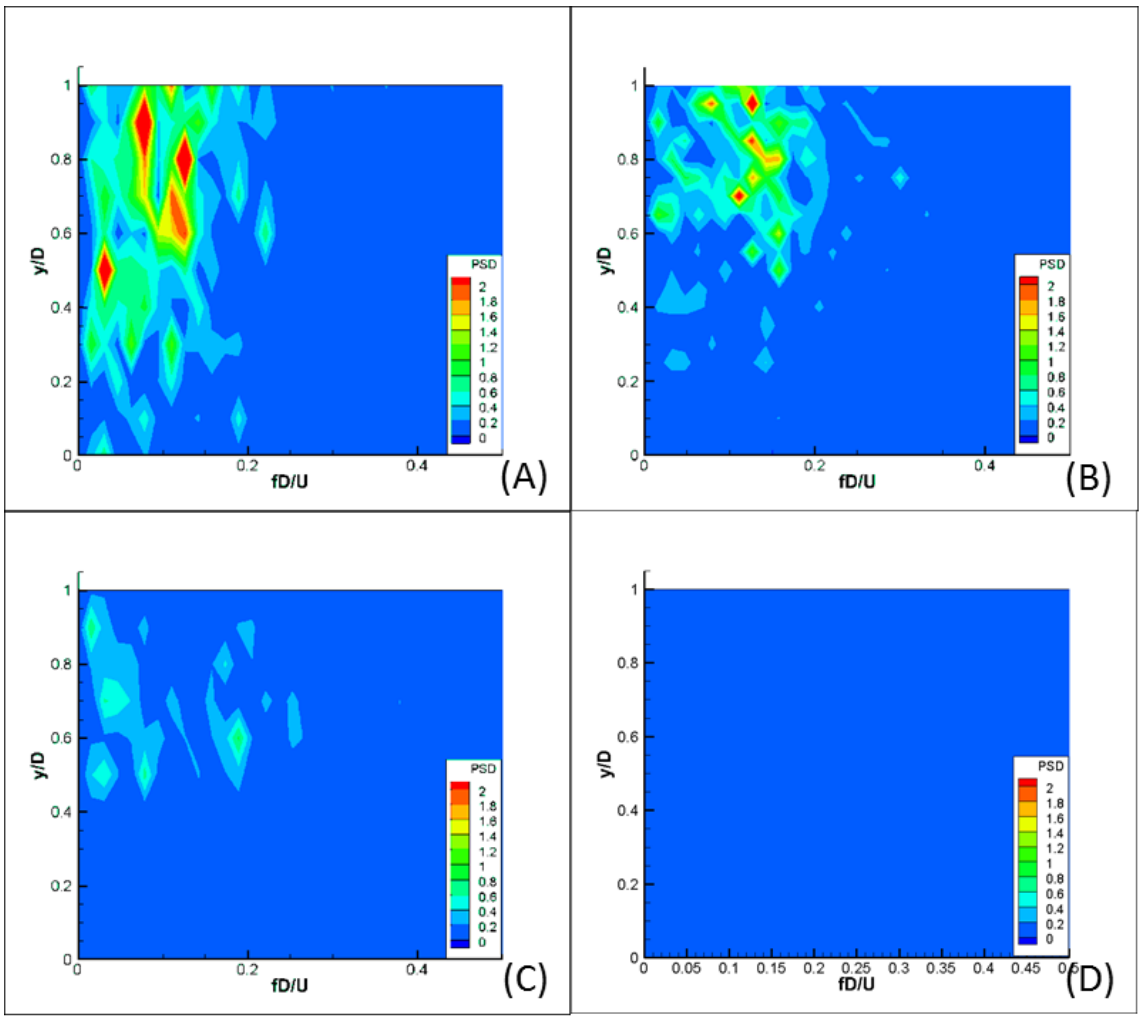

Figure 3.25.- PSD of the non-dimensionalized streamwise velocity as a function of fD/U at x/D=2.5, z/D=-0.3, (A) L/D=2.0, (B) L/D=1.0, (C) L/D=0.5, (D) L/D=0.3

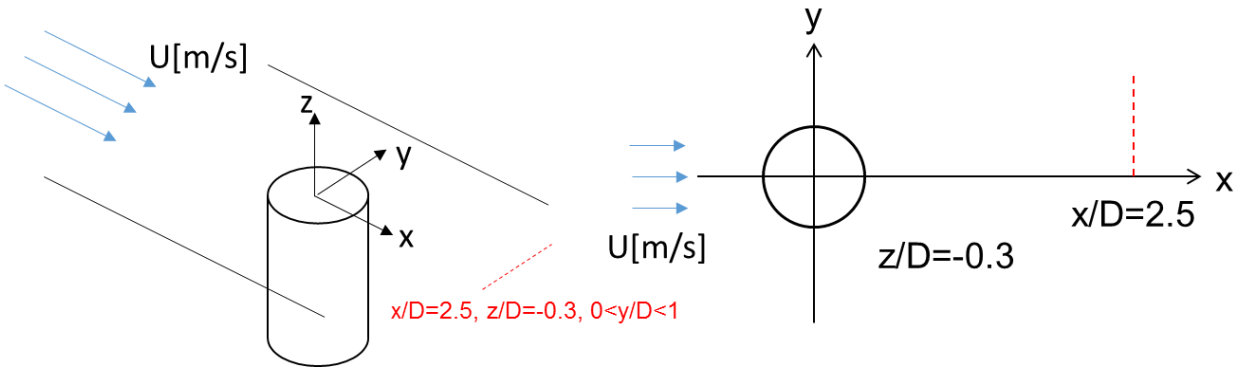

Figure 3.26 - Points at x/D=2.5, z/D=-0.3

3.3 Horizontal PIV measurements

Selected flow fields for Re=23000 for each aspect ratios are presented from Figure 3.27 to Figure 3.30. In these figures, both the mean velocity field and the mean vorticity field are made dimensionless with the uniform flow velocity U=0.329m/s and the cylinder diameter D=0.07m. The white circle means the position of the cylinder.

For all aspect ratios, the direction of separation of each plane goes inward as the z/D is smaller, that is, near the free end. Though the separation can be confirmed for all planes in Figure 3.30, near the free end, the vortex shedding from the side of the cylinder is thought to be suppressed by the free end. We can see the reason from Figure 3.28 and Figure 3.29. The red contour area implies the relatively high fluctuation of the velocity due to the von Karman vortex shedding, but it almost disappears near the free end such as z/D≦-1.75 for L/D=2.0, z/D≦-0.75 for L/D=1.0, and z/D≦-0.25 for L/D=0.5. In these areas, two counter vortex pairs of the arch-type vortex contribute the elevation of RMS Vx/U and RMS Vy/U.

Further investigations are tried in next sections using by POD and DMD.

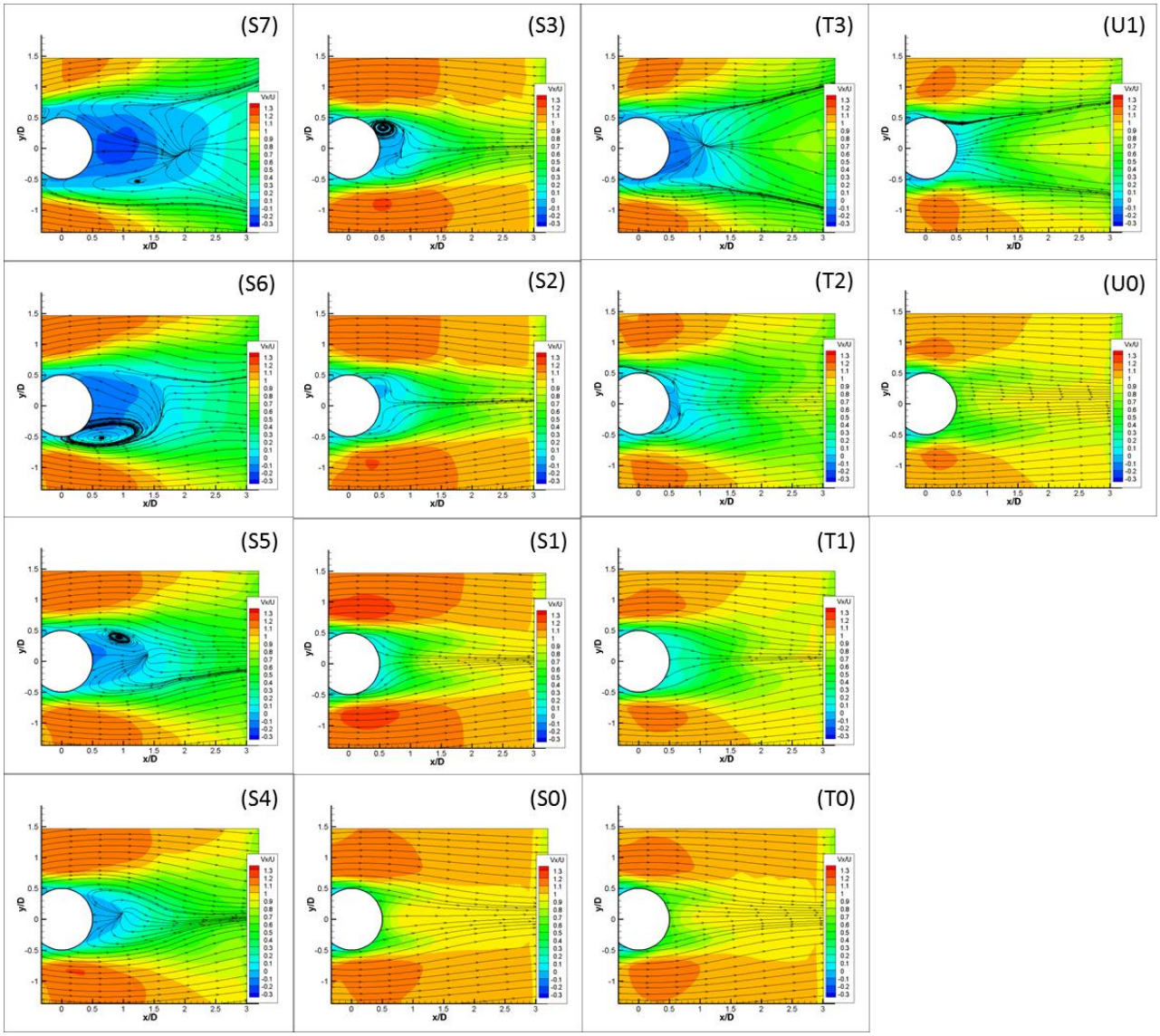

Figure 3.27 - Time-averaged streamlines and contours of mean velocity component Vx/U in the horizontal planes xy at Re=23000, L/D=2.0: (S7) z/D=-0.25, (S6) z/D=-0.5, (S5) z/D=-0.75, (S4) z/D=-1.0, (S3) z/D=-1.25, (S2) z/D=-1.5, (S1) z/D=-1.75, (S0) z/D=-2.0, L/D=1.0: (T3) z/D=-0.25, (T2) z/D=-0.5, (T1) z/D=-0.75, (T0) z/D=-1.0, L/D=0.5: (U1) z/D=-0.25, (U0) z/D=-0.5

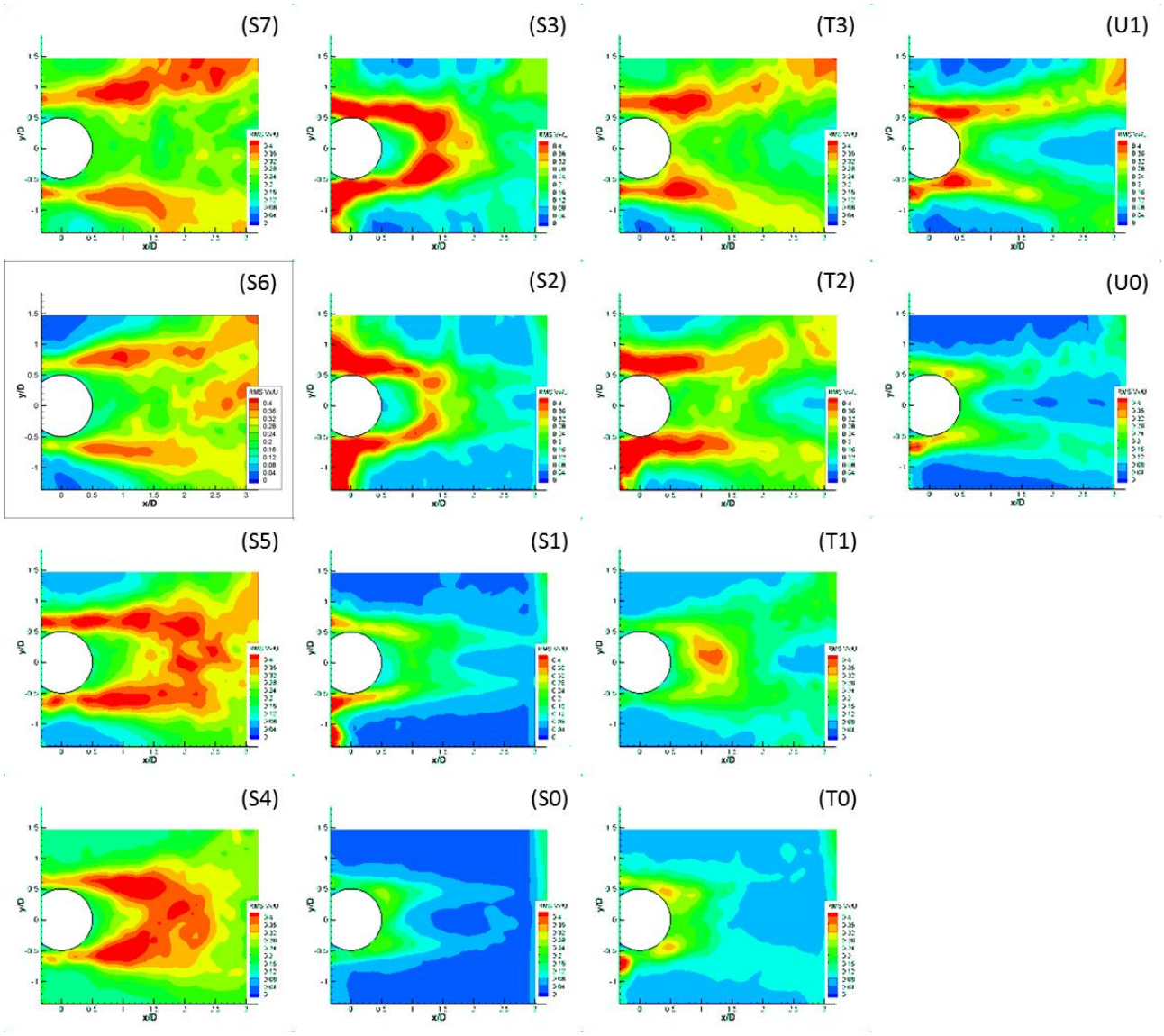

Figure 3.28 - Contours of root mean square of streamwise fluctuations RMS Vx/U in the horizontal planes xy at Re=23000, L/D=2.0: (S7) z/D=-0.25, (S6) z/D=-0.5, (S5) z/D=-0.75, (S4) z/D=-1.0, (S3) z/D=-1.25, (S2) z/D=-1.5, (S1) z/D=-1.75, (S0) z/D=-2.0, L/D=1.0: (T3) z/D=-0.25, (T2) z/D=-0.5, (T1) z/D=-0.75, (T0) z/D=-1.0, L/D=0.5: (U1) z/D=-0.25, (U0) z/D=-0.5

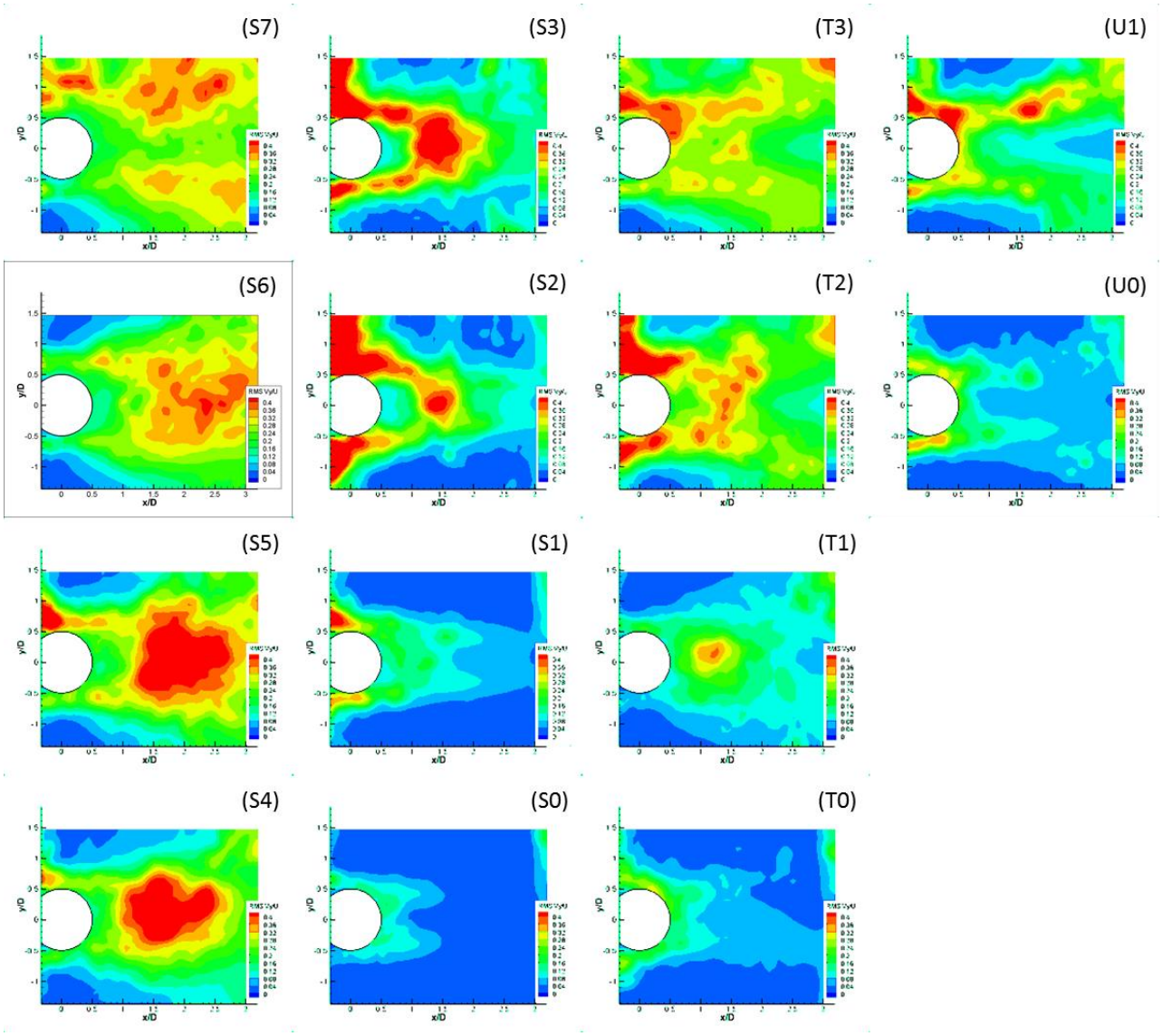

Figure 3.29 - Contours of root mean square of vertical fluctuations RMS Vz/U in the horizontal planes xy at Re=23000, L/D=2.0: (S7) z/D=-0.25, (S6) z/D=-0.5, (S5) z/D=-0.75, (S4) z/D=-1.0, (S3) z/D=-1.25, (S2) z/D=-1.5, (S1) z/D=-1.75, (S0) z/D=-2.0, L/D=1.0: (T3) z/D=-0.25, (T2) z/D=-0.5, (T1) z/D=-0.75, (T0) z/D=-1.0, L/D=0.5: (U1) z/D=-0.25, (U0) z/D=-0.5

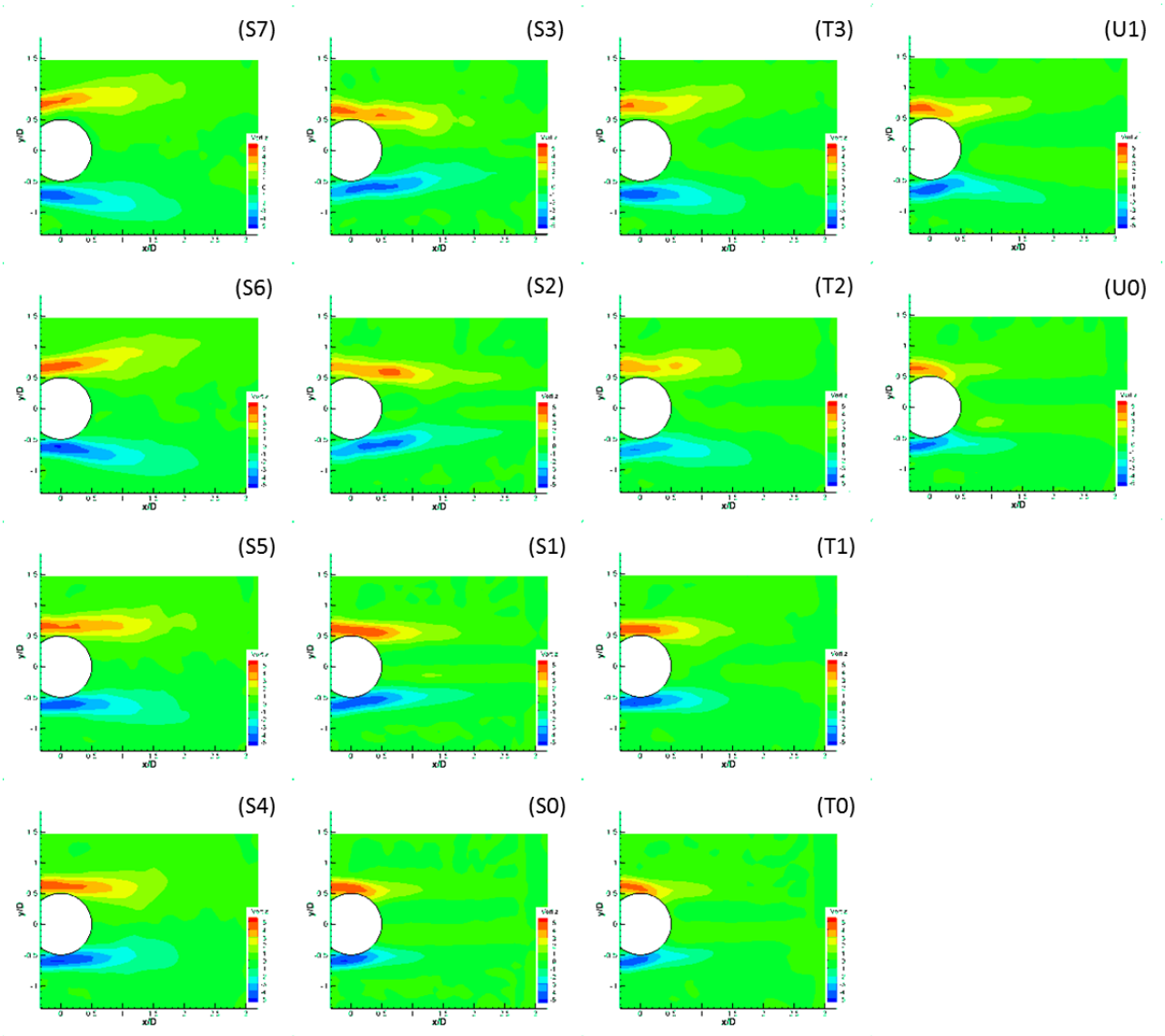

Figure 3.30 - Contours of mean vertical vorticity $\omega_z D/U$ in the horizontal planes xy at Re=23000, L/D=2.0: (S7) z/D=-0.25, (S6) z/D=-0.5, (S5) z/D=-0.75, (S4) z/D=-1.0, (S3) z/D=-1.25, (S2) z/D=-1.5, (S1) z/D=-1.75, (S0) z/D=-2.0, L/D=1.0: (T3) z/D=-0.25, (T2) z/D=-0.5, (T1) z/D=-0.75, (T0) z/D=-1.0, L/D=0.5: (U1) z/D=-0.25, (U0) z/D=-0.5

3.4 Proper Orthogonal Decomposition (POD) analysis

Proper Orthogonal Decomposition is an analysis technique that optimally extracts spatial modes from flow data. In this section, POD technique is applied to extract the dominant flow mode.

3.4.1 POD algorithm

Assuming that $\{v_t\}$ is a physical quantity data (space information) at the certain time t, the time-space information Z^T in this experiment is defined as below. The subscript T denotes the transpose operator.

$$Z^T = \{v_1, v_2, \dots, v_{345}\ \}$$

The idea of POD is to find the linear sum of empirical functions φ_k which are orthogonal, i.e.,

$$Z = \sum_{t=1}^{345} (\langle v_t, \varphi_1 \rangle \varphi_1 + \langle v_t, \varphi_2 \rangle \varphi_2 + \langle v_t, \varphi_3 \rangle \varphi_3 + \cdots + \langle v_r, \varphi_r \rangle \varphi_r)$$

$\langle , \rangle$ is inner product. r is selected to satisfy

$$\frac{\sum_{k=1}^{r} s_k}{\sum_{k=1}^{345} s_k} \approx 1$$

In short, POD is to decompose Z into the sum of the product of time information and space information. To achieve this decomposition, the following steps are taken. The detail theory is referred to Sakai *et al.* (2014). First, the autocovariance matrix A is created by

$$\mathrm{A} = ZZ^T$$

Second, the above eigenvalue problem is solved by

$$\mathrm{A}e_k = s_k e_k$$

where s_k is the eigenvalue and e_k is the eigenvector.. The calculated eigenvalues are ordered from big to small and e_k are standardized. Finally, POD modes φ_k are calculated by

$$\varphi_k = Z^T e_k / \sqrt{s_k}$$

$\langle v_t, \varphi_k \rangle$ is called mode coefficient and changes over time. In other words, if it is processed by FFT, the period of the mode can be found.

3.4.2 Results and discussion

The time series streamwise vorticity field at L/D=2.0 and z/D=-0.25 was processed by POD.

Figure 3.31 shows the PSD of mode coefficient for mode1 and 2 and 3.

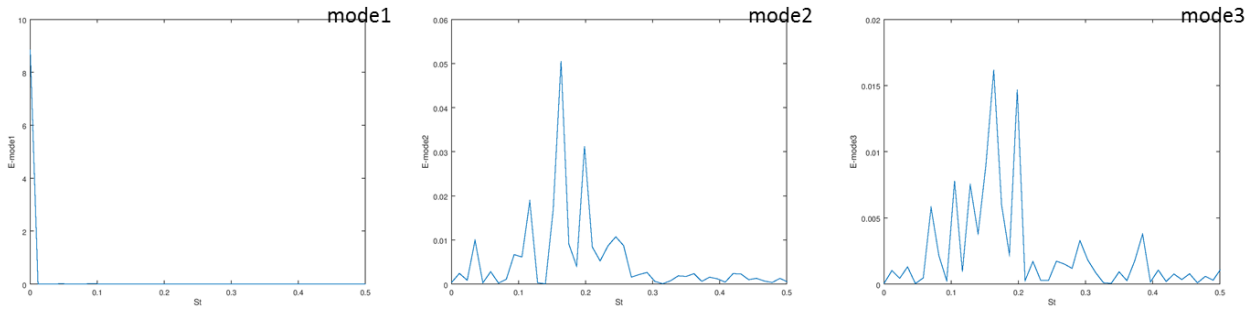

Figure 3.31 - PSD of the mode coefficient for streamwise vorticity field at L/D=2.0 and z/D=-0.25

Mode 1 means the mean field. Mode 2 and 3 captured the vortyex shedding frequency, fD/U～0.17. The fields for each mode are presented in Figure 3.32. Mode 2 and 3 looks a pair mode.

Figure 3.33 shows the energy rate that each mode has. Accumlative energy rate is the sum of the energy rate from mode1 to mode N. Mode1 occupied about 33% of the vorticity field. In the long time span, the modes which has high energy rate are essential and the modes which has low energy rate are not. The reconstruction of the flow field will be left to the future.

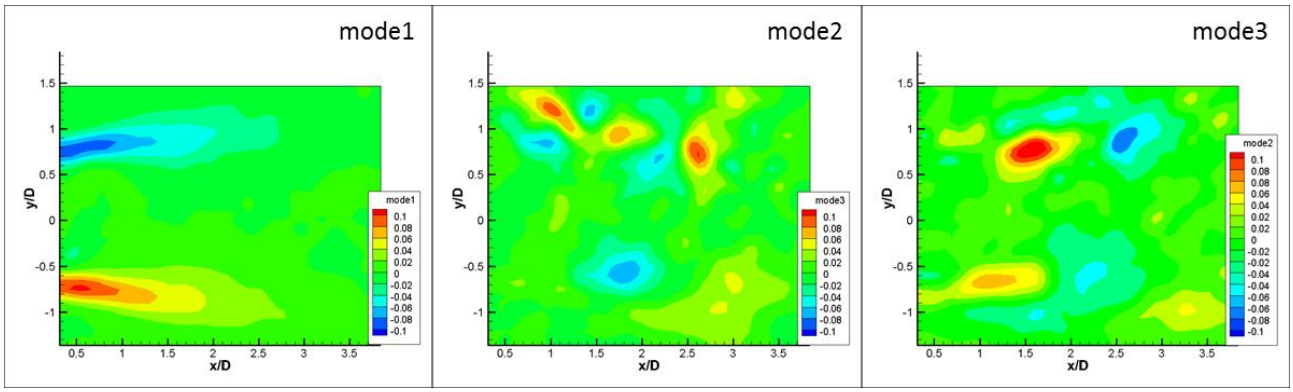

Figure 3.32 - POD mode for streamwise vorticity field at L/D=2.0 and z/D=-0.25

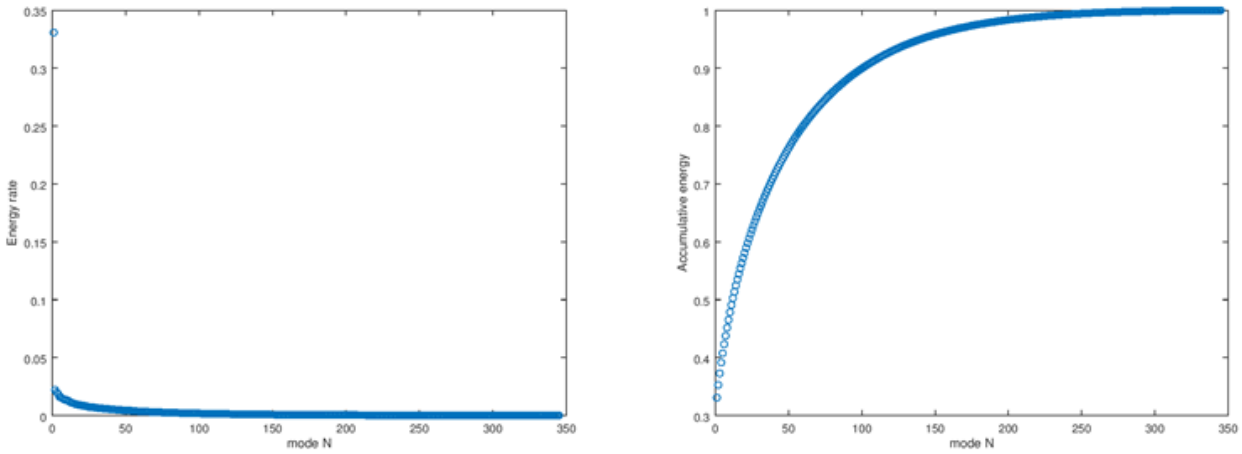

Figure 3.33 – Energy rate of each mode (left) and accumlative energy rate (right) at L/D=2.0 and z/D=-0.25

The time series streamwise vorticity field at L/D=2.0 and z/D=-2.0 was processed by POD.

Figure 3.34 shows the PSD of mode coefficient for mode1 and 2 and 3. In this case, the measurement plane was at the end of the cylinder and the free-end effect was remarkable. Mode 2 and 3 have the energy at the low frequency, fD/U<0.5. Mode 2 and 3 in Figure 3.35 were considered to capture the arch-type vortex around the free end. Figure 3.36 shows the energy rate and accumlative energy rate. Mode1 occupied about 75% of the vorticity field which were much more than 33% in Figure 3.33. This suggests that the vorticity fluctuation was lower near the free end.

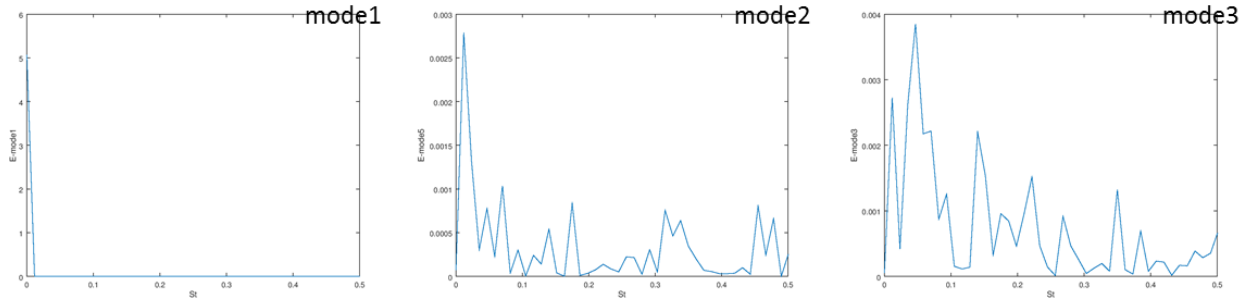

Figure 3.34 - PSD of the mode coefficient for streamwise vorticity field at L/D=2.0 and z/D=-2.0

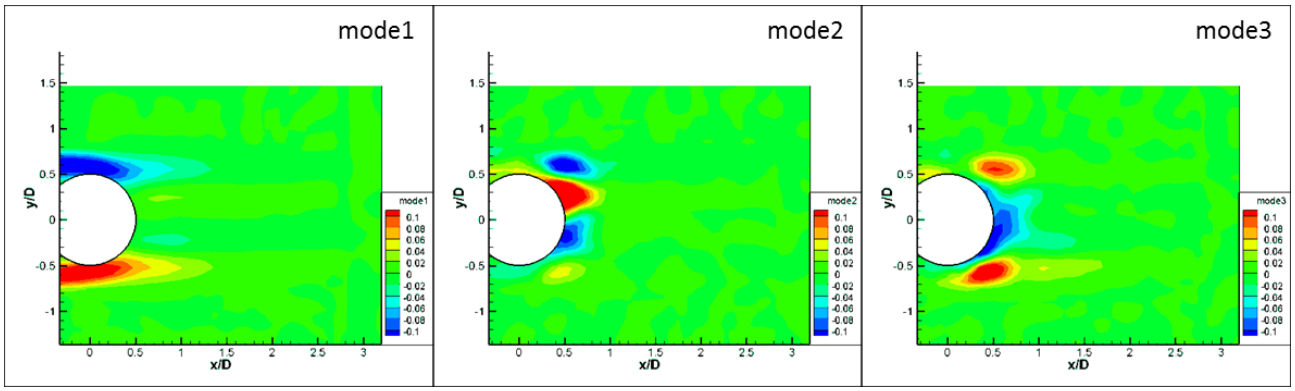

Figure 3.35 - POD mode for streamwise vorticity field at L/D=2.0 and z/D=-2.0

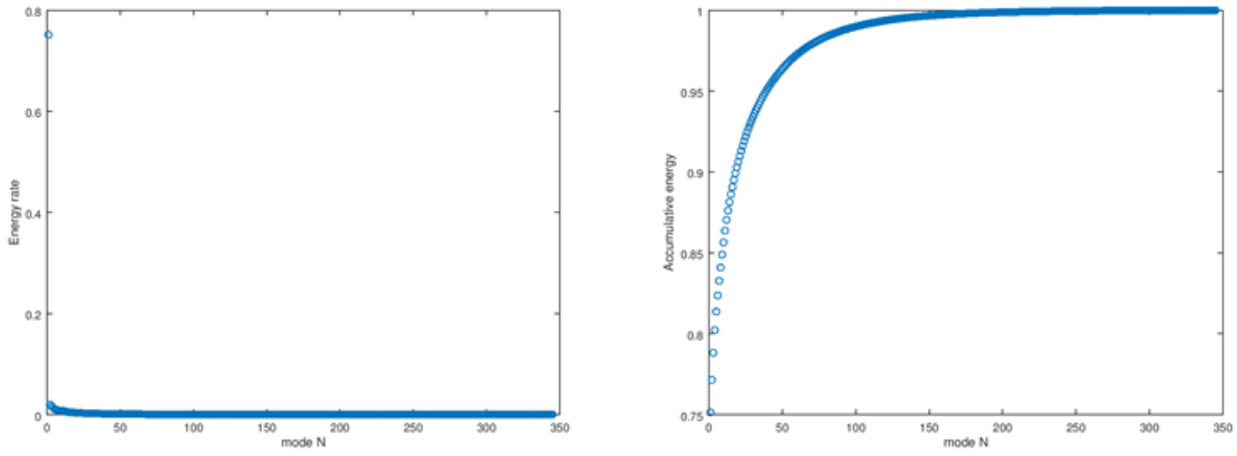

Figure 3.36 - Energy rate of each mode (left) and accumlative energy rate (right) at L/D=2.0 and z/D=-2.0

3.5 Dynamic Mode Decomposition (DMD) analysis

As above mentioned, the order of snapshots is not considered in the POD analysis. Thus, the POD analysis in this study is not better to extract temporal variations. On the other hand, DMD is an analysis technique to cope with relationships between two continuous data and to extract dynamic information and corresponding modes at a specific frequency.

3.5.1 DMD algorithm

Assuming that $\{v_t\}$ is a physical quantity data at the certain time t, the basic premise of DMD is that $\{v_{t+1}\}$ is obtained by a linear dynamical system,

$$v_{t+1} = Av_t$$

where the matrix A is not a function of time t. When the time-space information X_1^m is expressed as bellows,

$$X_1^m = [v_1, v_2, \cdots, v_m]$$

the following formula is fulfilled.

$$AX_1^m = X_2^{m+1}$$

Although DMD modes are eigenvectors of the matrix A, it will take very long time to calculate them directly from this equation. Therefore, the eigenvalues and eigenvectors are calculated by singular value decomposition in DMD analysis. Singular value decomposition is to decompose X_1^m into three matrices $U, \Sigma, and\ V$, as

$$X_1^m = U\Sigma V^T$$

where U and V are matrices in which columns have orthonormality and Σ is a diagonal matrix. V^T is the adjoint matrix of V. As $X_2^{m+1}, U, \Sigma, and\ V$ are already known, S is defined as follows to fulfill $AU=US$,

$$S = U^T AU = U^T X_2^{m+1} V \Sigma^{-1}$$

Eigenvalues of A can be approximately found as those of S. Eigenvectors of A, i.e. DMD modes, are calculated from eigenvectors of S as

$$\xi_i = U\varphi_i$$

where $\{\varphi_i\}_{i=1}^m$ are eigenvectors of S. Then, $\{v_t\}$ can be expressed as follows by using eigenvalues $\{\kappa_i\}_{i=1}^m$ and DMD modes $\{\xi_i\}_{i=1}^m$,

$$v_t = A^{t-1} v_1 = \sum_{i=1}^{m} c_i {\kappa_i}^{t-1} \xi_i$$

where c_i is the coefficient decided for each mode and is not a function of time. The value of κ_i determines amplification or attenuation of the flow structure in DMD mode. $|\kappa_i| < 1$ means that the observed flow is attenuated. $|\kappa_i| = 1$ means that the observed flow is periodic. $|\kappa_i| > 1$ means that the observed flow is amplified. At this time, c_i denotes the degree of contribution, and ${\kappa_i}^{t-1}$ denotes the temporal phase.

A mode energy of the DMD mode is defined as

$$F_i = |c_i|^2$$

Strouhal number of the jth mode is

$$St_j = \frac{f_j R}{U} = \frac{\omega_j R}{2\pi U} = \frac{Im\{\ln(\kappa_j)\} R}{2\pi \Delta t U} = \frac{\arg(\kappa_j)\, R}{2\pi \Delta t U}$$

3.5.2 Results and discussion

The time series streamwise velocity field at L/D=2.0 and z/D=-0.25 was processed by DMD. When the fields are processed for snapshot number 1~344, eigenvalues are presented in Figure 3.33. The attenuation value appears, but this is thought to be a fake due to the lack of space information. Then, we reduce the number of snapshots processed and obtained Figure 3.34. Future work will seek to understand this cause. Results presented in

the Appendix might be a clue.

Figure 3.35 shows therelationship between Strouhal number and Energy which each modes have. There is a peak around 1.7, the same peak as POD results above. Figure 3.36 shows the DMD mode at this peak. It was considered to capture the vortex shedding frequency. However, the characteristic of the flow was not clarified. This might be because the space resolution of the PIV was low.

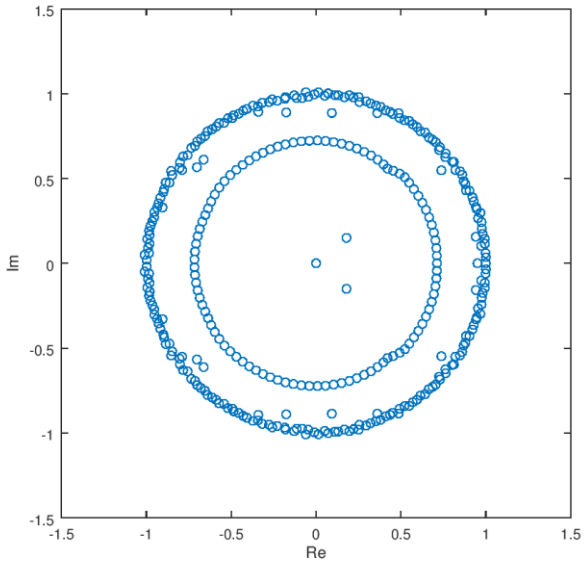

Figure 3.37 - Eigenvalues of the time series streamwise velocity field at L/D=2.0 and z/D=-0.25 by DMD (snapshot number: 1~344)

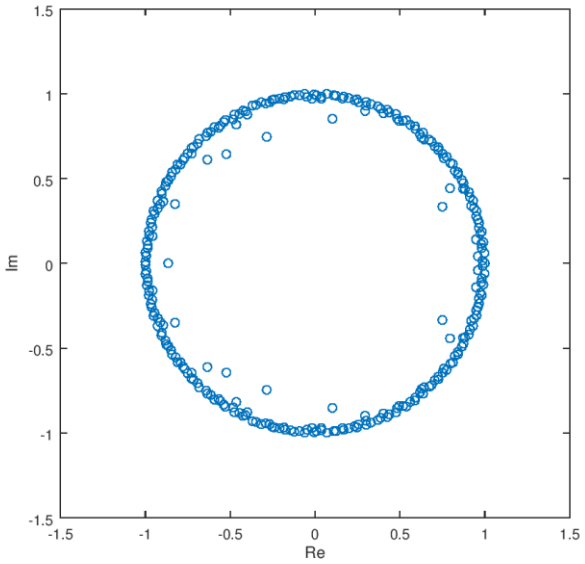

Figure 3.38 - Eigenvalues of the time series streamwise velocity field at L/D=2.0 and z/D=-0.25 by DMD (snapshot number: 1~291)

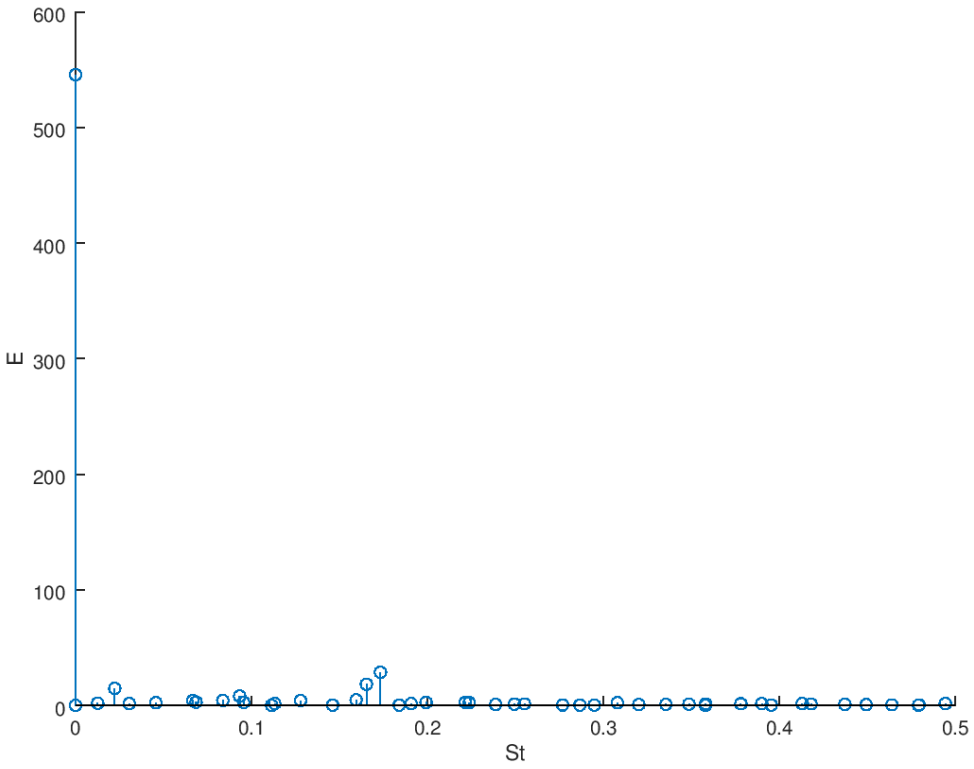

Figure 3.39 - Relationship between Strouhal number and Energy of the time series streamwise velocity field at L/D=2.0 and z/D=-0.25 by DMD

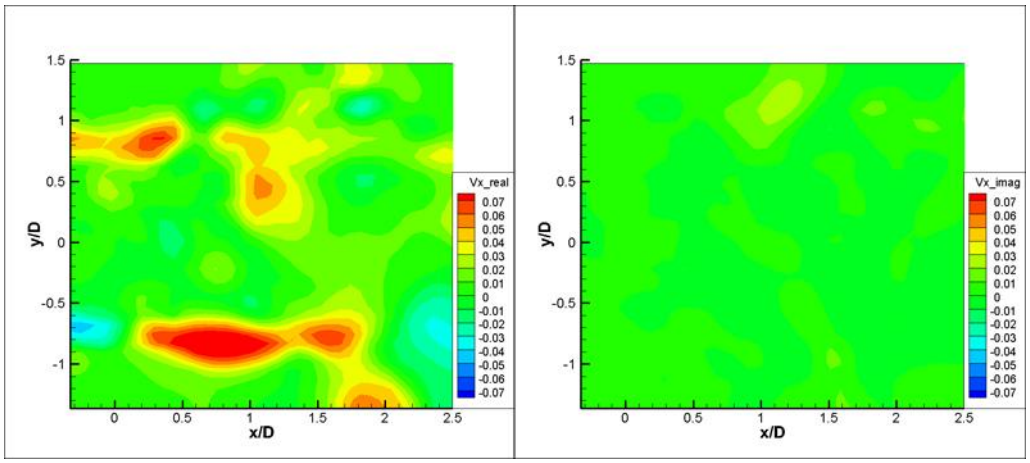

Figure 3.40 - DMD modes (real part (left) and imaginary part (right))of the highest energy frequency for time series of the streamwise velocity field at L/D=2.0 and z/D=-0.25

Chapter 4 Force measurement

4.1 Experimental setup

Experiments were mainly carried out in the towing tank at the University of Tokyo Hongo Campus, Tokyo, Japan. The scale of the test section is 85.0m x3.5m x 2.4m (length x wide x depth). Experimental settings are illustrated in Figure 4.1. A half-submerged cylinder was towed and forces in the streamwise and the transverse directions were measured. Two experimental runs were performed for each conditions.

Nine cylinders with different diameters in Figure 4.2 were used and their diameters are 0.07, 0.1, 0.125, 0.13, 0.2, 0.25, 0.3, 0.4, 0.6m, respectively. Table 4.1 shows conditions for each cylinder. Four different aspect ratios namely, AR=0.5, 1.0, 1.5, 2.0 were tested mainly. As for the cylinder with D=0.1m, tested aspect ratios were up to 14 and only AR effect was focused on with the constant values, Re=43000 and Fr=0.311. Since the diameters were different, the effect of Re on hydrodynamic forces was also investigated with the same Froude number, 0.311. The conditions are presented in Table 4.2.

Two load cells (A. LMC-3506-200N, B. LMC-3504-20N NISSHO-ELECTRIC-WORKS CO., LTD.) were employed to acquire the hydrodynamic forces. Load cell A has a sensing capacity of 200N in the Fx and Fy with a resolusion of 0.4N. Load cell B has a sensing capacity of 20N in the Fx and Fy with a resolusion of 0.04N. Load cell A was used to 0.07, 0.1, 0.125, 0.13, 0.6m diameter cylinders and load cell B was used to 0.2, 0.25, 0.3, 0.4, 0.6m diameter cylinders. The reason why two different load cells were adopted is explained below. The data was acquired in the towing tank with 70m of towing distance with the sampling frequency of 100Hz.

Furthermore, for some cases, the water position around cylinders were recorded by a video camera as shown in Figure 4.3. Scales were drawn on the surface of the cylinders at 45 degree intervals from the front stagnation point to the back stagnation point.

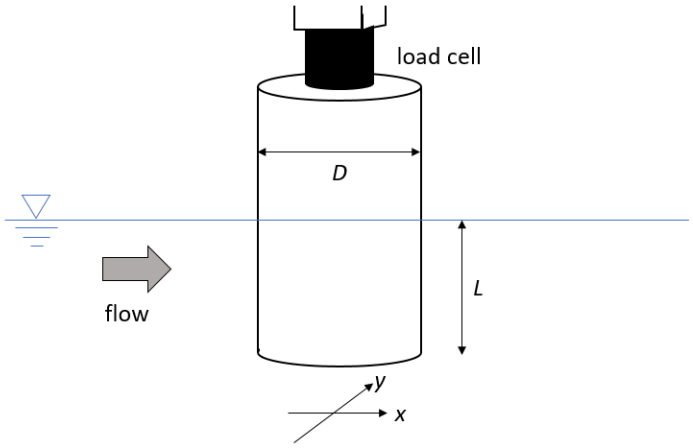

Figure 4.1 - Schematic diagram of the force measurement

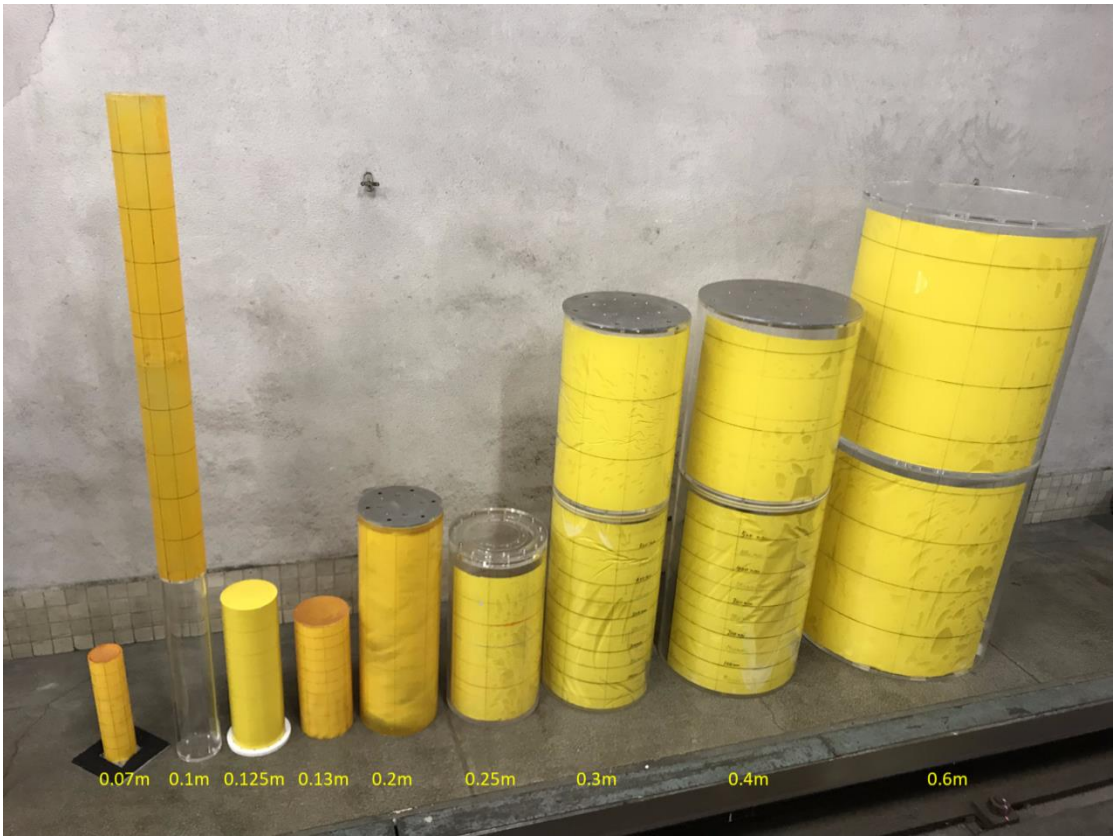

Figure 4.2 – Cylinders for experimentwith decreasing St

Table 4.1 – Re fixed cases (Re=43000)

D[m]	Fr	AR
0.07	0.742	0.5, 1.0, 1.5, 2.0, 2.5, 3.0
0.1	0.434	0.5, 1.0, 1.5, 2.0, 3.0–14.0
0.125	0.311	0.5, 1.0, 1.5, 2.0, 2.5, 3.0
0.13	0.293	0.25, 0.5, 1.0, 1.5, 2.0
0.2	0.154	0.25, 0.5, 1.0, 1.5, 2.0
0.25	0.11	0.5, 1.0, 1.5
0.3	0.0836	0.25, 0.5, 1.0, 1.5, 2.0, 2.5, 3.0
0.4	0.0543	0.25, 0.5, 1.0, 1.5, 2.0, 2.5
0.6	0.0296	0.25, 0.5, 1.0, 1.5, 2.0

Table 4.2 – Fr fixed cases (Fr=0.311)

D[m]	Re	AR
0.13	45606	0.25, 0.5, 1.0, 1.5, 2.0
0.2	87026	0.25, 0.5, 1.0, 1.5, 2.0
0.3	159877	0.25, 0.5, 1.0, 1.5, 2.0
0.4	246147	0.25, 0.5, 1.0, 1.5, 2.0
0.6	452200	0.25, 0.5, 1.0, 1.5, 2.0

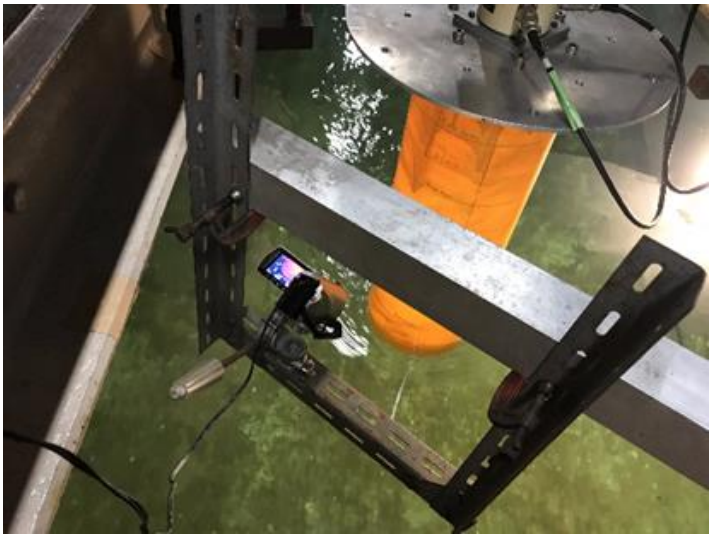

Figure 4.3 - A scene of force and water position measurement

In this experiment, there was a danger that the inertial force would be too large for large diameter models. See the example of force time series in Figure 4.4. This is the case of D=0.6m, Re=43000, AR=2.0. The velocity of the towing car was zero for the first 40 seconds, and then the car started accelerate and reach a constant velocity. The range for the statistic

calculations was the latter part as possible to use the steady state so that the range would include at least 7 cycles of Karman vortex shedding based on St=0.2 even for small U/D cases. The length of the tank is limited and this is the limitation of the experiment. The maximum force reached 100N and there would be a possibility to break the 20N load cell. That was why 200N load cell was adopted for larger diameter cylinders. To measure the small forces, the calibration of load cells was conducted by using balanced weights and the accuracy was confirmed. The results are presented in Figure 4.5 and show the accuracy. Figure 4.5 shows the ratio between force[N] and volt[V] for each weight[g]. The weights are 1, 2, 3, 50, 51, 52, 53, 100, 101, 102, 103g. If the weight is heavier than 2g, the ratio is almost the same. If the weight is lighter than 1g, the accuracy is not always guaranteed. Fortunately, in this study, the target forces are more than 2g for most cases. For the other cases, we need to bear in mind that there is maximum about 20% measurement error. Another consideration is sloshing. Some cases included water inside the cylinder. However, the low-pass filtered frequency range was very low ($fD/U<0.5$). Figure 4.6 shows the non-dimensionalized PSD of zero condition, which means the towing car did not start yet. The sloshing frequency is much higher than our interest frequency range. Therefore, forces caused only by fluid phenomenon were able to be extracted. To make sure these concerns, two load cells were applied to 3cases, D=0.6m, Re=43000, AR=0.25, 0.5, 1.0. For 20N load cell, the ballast weights (maximum 160kg) were loaded in place of water to suppress the inertial forces at the beginning of the acceleration. Results are the ends of error bars presented in Figure 4-6. For most cases, the results were similar and had the same order.

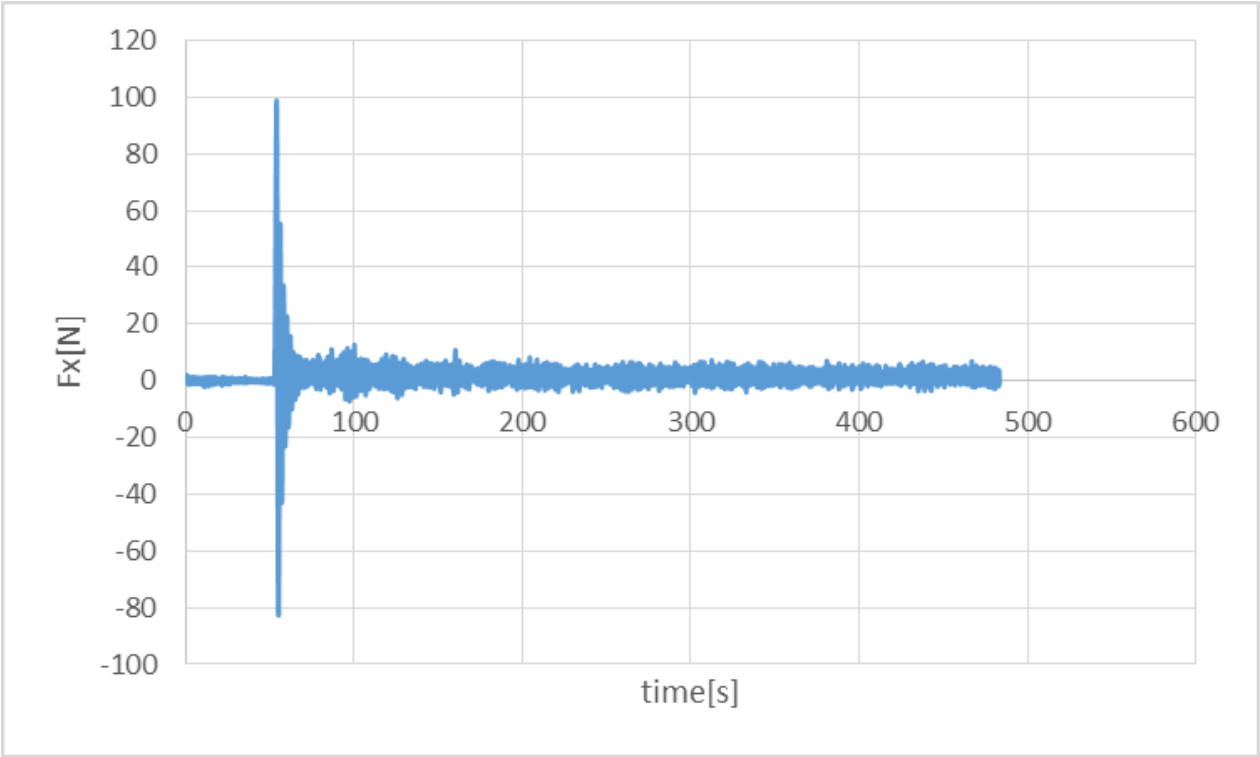

Figure 4.4 - Time series drag force Fx[N] (D=0.6m, Re=43000, AR=2.0)

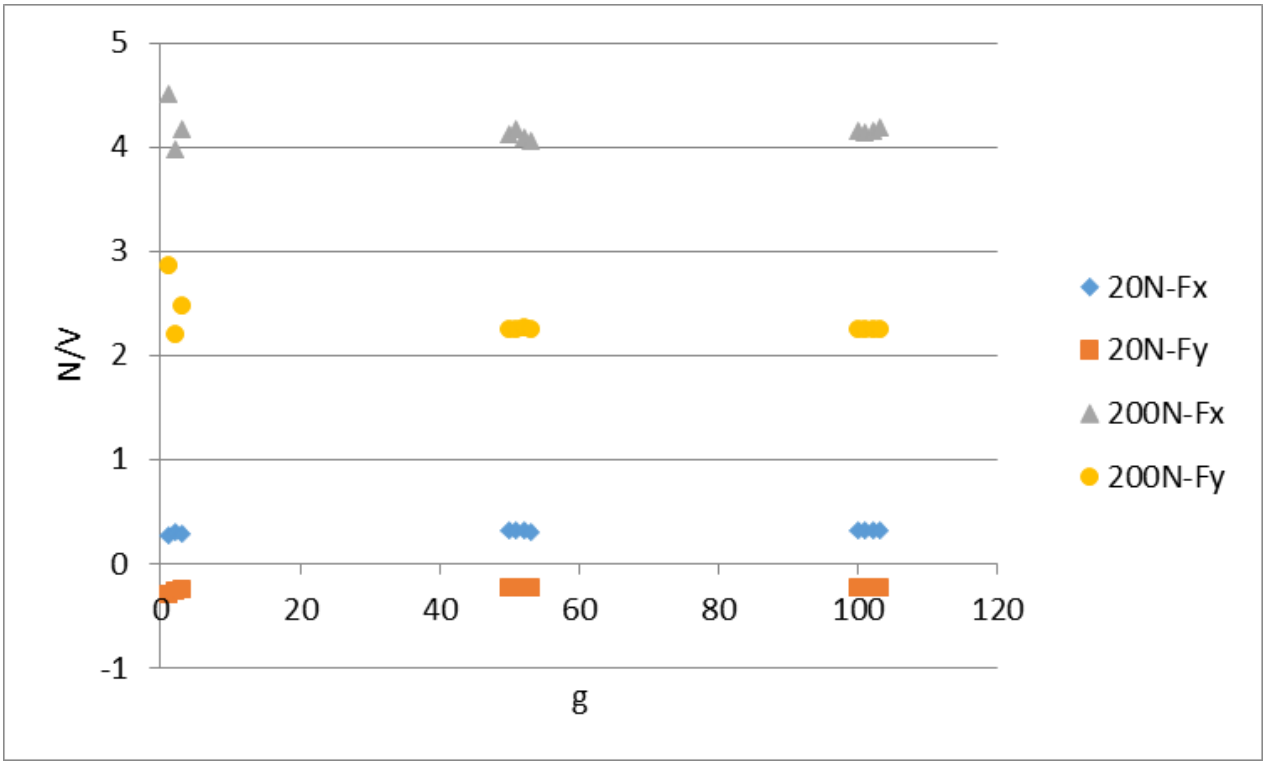

Figure 4.5 - Calibration of load cells (the ratio between force[N] and volt[V] for each weight[g])

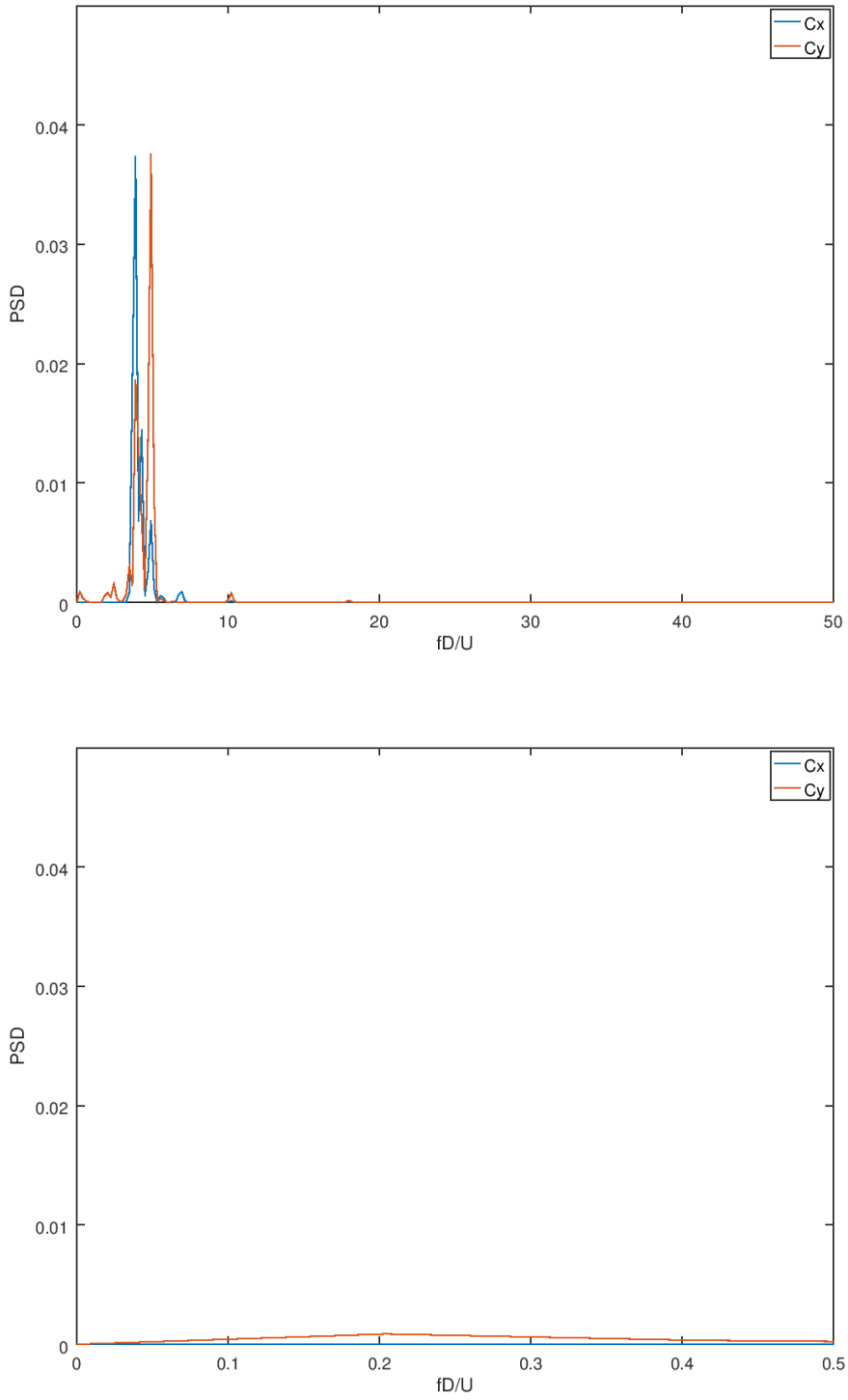

Figure 4.6 - Non-dimensionalized PSD of zero condition (D=0.6m, Re=43000, AR=1.5)

The other experiments to compare the free-surface conditions and 'no-slip' conditions were performed in a recirculating water channel (see Figure 4.28 in section 4.6) at the University of Tokyo Hongo Campus, Tokyo, Japan. The scale of the test section is 1840mm x 500mm x 700mm (length x wide x depth). Experimental settings were the same as Figure 4.1. A half-submerged cylinder was fixed in uniform flow and forces in the streamwise direction and the transverse direction were measured for each conditions. The no-slip conditions were realized by fixing the board on the water surface and fixing it by the tape, see Figure 4.29 in section 4.6. The board was placed so as not to touch the cylinder and not to generate air bubbles. The water between the wall of the cylinder and the hall of the board covered very small area of the cylinder surface and the effect was neglected here. Results are included in section 4.6.

4.2 Analysis methodology

Time-series of forces were made dimensionless to the drag coefficient, Cx and the lift coefficient, Cy as shown in Equation (1). Time-series Cx and Cy were processed by Fast Fourier Transformation and low-pass filtered at the threshold of which non-dimensionalized frequency, fD/U is 0 up to 0.5. Mean (time-averaged) and RMS (root-mean-square) value in this frequency range were calculated following Equation (2) and (3). PSD-power spectrum density of Cx and Cy was also calculated by multiplying hamming window to the time-series data and the value of PSD[s] was made dimensionless by multiplying U/D to n-PSD[-].

$$C_x = \frac{2F_x}{\rho LDU^2}, C_y = \frac{2F_y}{\rho LDU^2} \quad (1)$$

$$C_{x\_mean} = \frac{1}{m}\sum_{i=1}^{m} C_{x,i}\,, C_{y\_mean} = \frac{1}{m}\sum_{i=1}^{m} C_{y,i} \quad (2)$$

$$C_{x\_rms} = \left(\frac{1}{m} \sum_{i=1}^{m} (C_{x,i} - C_{x\_mean})^2 \right)^{\frac{1}{2}},$$

$$C_{y\_rms} = \left(\frac{1}{m} \sum_{i=1}^{m} (C_{y,i} - C_{y\_mean})^2 \right)^{\frac{1}{2}} \quad (3)$$

4.3 Froude number effect (free-surface vs 'free-slip' conditions)

In this thesis, error bar shows the results acquired from two runs in the experiment. Figure 4.7 shows the mean drag coefficient as a function of Fr for each AR. Cx_mean is smaller for AR≦1.0 at most Froude numbers and free-end effects are remarkable in AR≦1.0. Cx_mean decreases with AR decreasing as Gonçalves *et al.* (2015) pointed out. For AR≧0.5, the value for 0.05<Fr<0.5 is within the same range for each AR and increases as Fr increases from 0.434 to 0.742. Cx_mean increased faster when Fr increased for lower aspect ratio cases, therefore the free-surface effect was significant for Fr>0.5 and the effect was larger for the lower aspect ratio. This means free-surface effect appears around Fr>0.5 and the effect is larger in lower aspect ratio. Interestingly, Cx_mean value for AR=1.5, 2.0 at minimum Fr is larger. The reason is discussed in Chapter 5.

Figure 4.8 is the re-organized graph of Figure 4.7 and shows the mean drag coefficient as a function of AR. It is also confirmed from this figure that the case of 0.05<Fr<0.5 has the similar tendency and the case of Fr=0.0296 and.0.742 has the different tendency.

Figure 4.9 shows the RMS of drag coefficient as a function of Fr for each AR. For AR≧1.5, the tendency is almost the same. Cx_rms is larger as Fr is

smaller. This is because the free-surface motion becomes bigger with the increase of Fr and the vortex-shedding from the side of the cylinder is disturbed as pointed out in Chapter 2. Another reason is the decrease of vortex shedding region from the side of the cylinder. As Fr increases, the depression of water position at the rear of the cylinder occurs. For AR≦1.0, Cx_rms value is bigger than that of AR≧1.5 at many Froude numbers because of the free-end effect.

Figure 4.10 shows the RMS of lift coefficient as a function of Fr for each AR. Cy_rms at AR=0.5 is the largest among all aspect ratios. The reason is discussed in Chapter 5. Comparing maximum Fr cases to minimum Fr cases at 0.5≦AR≦2, Cy_rms decreases. This can be explained by the same reason as Cx_rms.

Figure 4.11 – 4.14 show the non-dimensionalized PSDs for each aspect ratio at selected Froude numbers. For lower aspect ratio cases, AR=0.5 and AR=1.0, with increasing Fr, the PSDs has peaks at various non-dimensionalized frequencies. This may be because the free-surface movement is more dominant per cylinder's surface area. For AR=2.0, the frequency fD/U=0.1~0.2 at which vortex shedding from the side of the cylinder appears(Gonçalves *et al.* (2015), Sakata *et al.* (2018)), has lower energy at the largest Fr=0.742 due to the free-surface effect. For AR=0.5, the frequency fD/U=0~0.1 which means vortex shedding from the bottom of the cylinder (Gonçalves *et al.* (2015), Sakata *et al.* (2018)), has also lower energy at the largest Fr=0.742 due to the free-surface effect. Since this figures intend to compare cases with different U/D, we expressed the vertical axis notation by 'n-PSD', but 'PSD' in this chapter basically stands for 'n-PSD' in Equation (3).

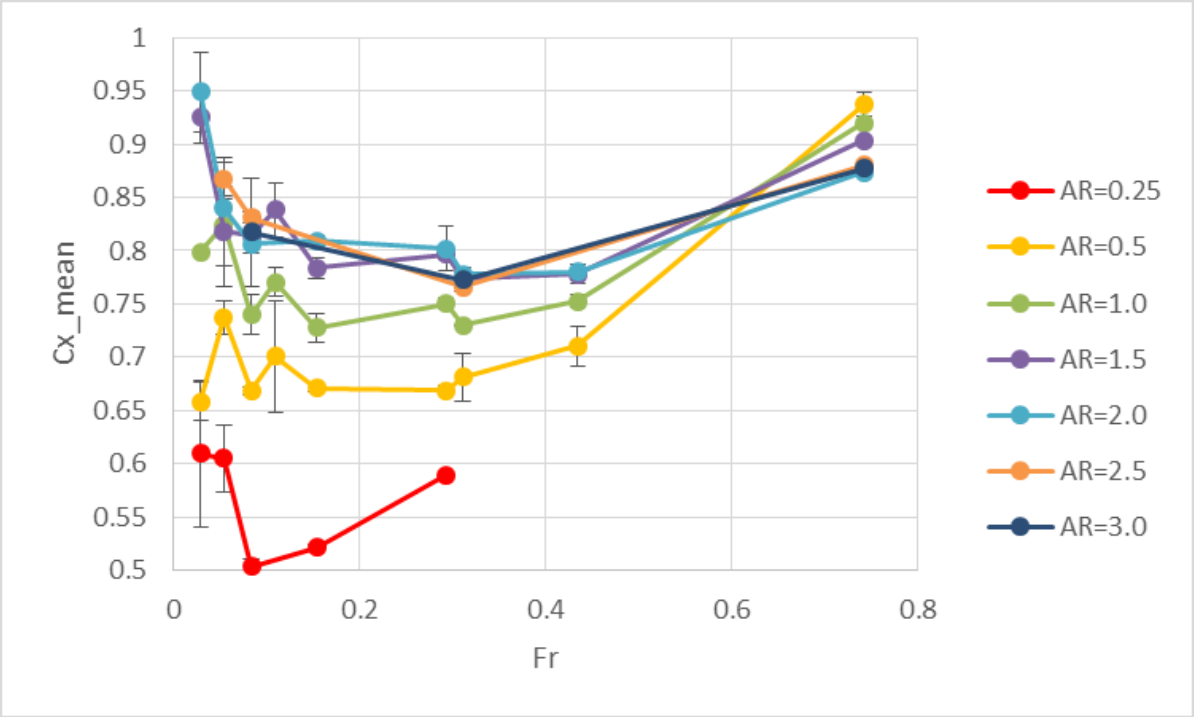

Figure 4.7 – Mean drag coefficient as a function of Froude number for each aspect ratio

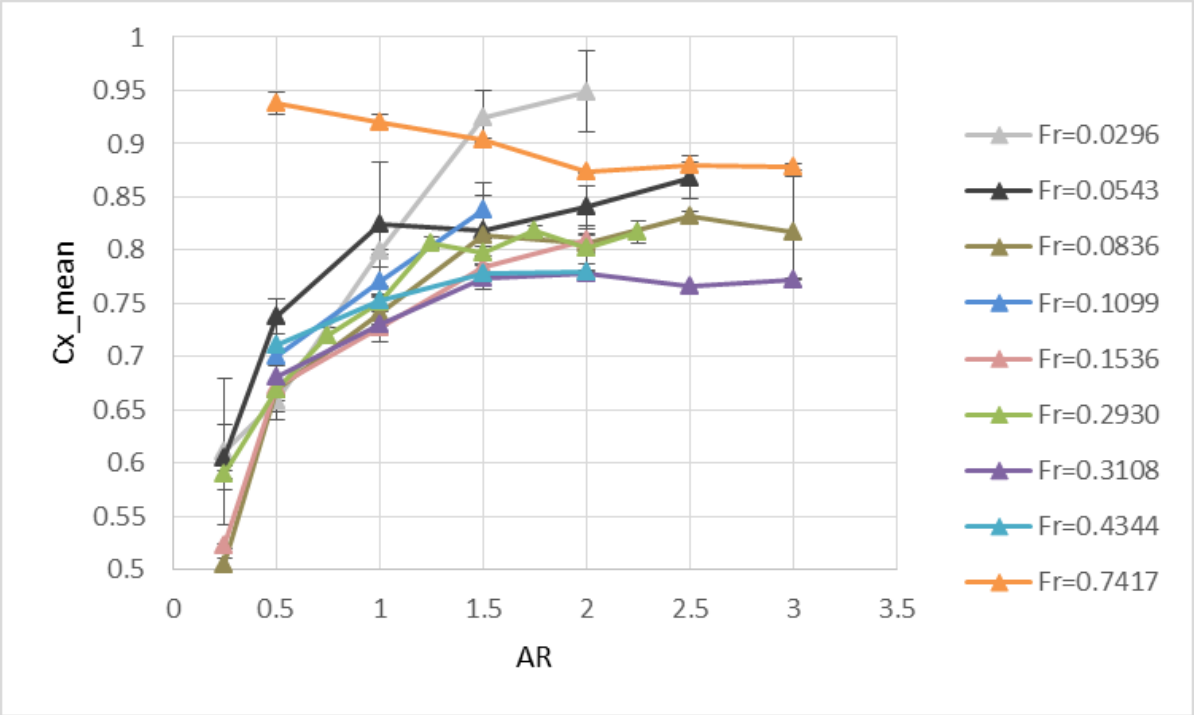

Figure 4.8 – Mean drag coefficient as a function of Froude number for each Froude number

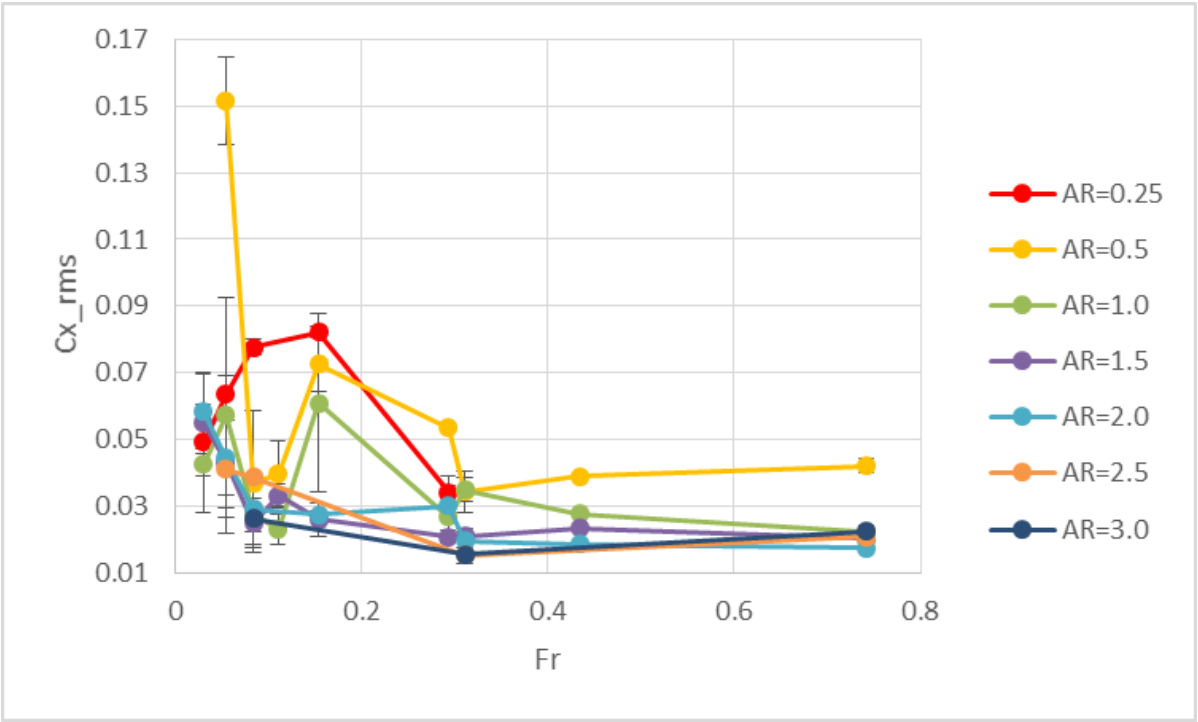

Figure 4.9 – RMS of drag coefficient as a function of Froude number for each aspect ratio

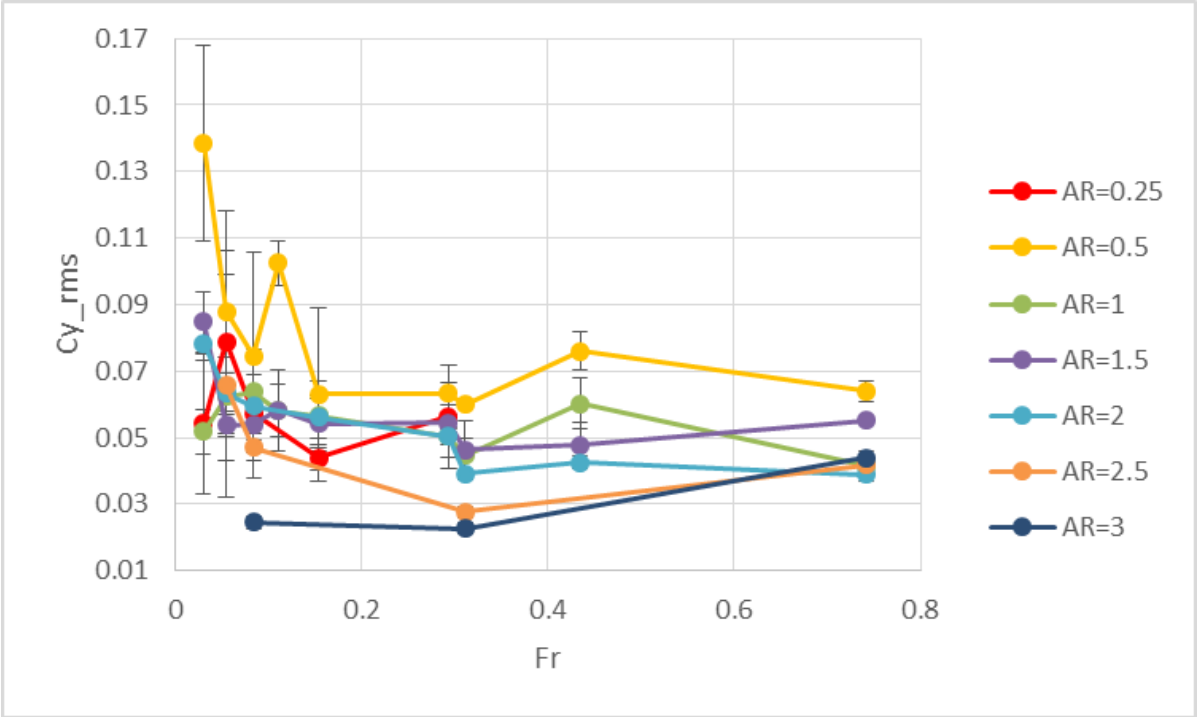

Figure 4.10 – RMS of lift coefficient as a function of Froude number for each aspect ratio

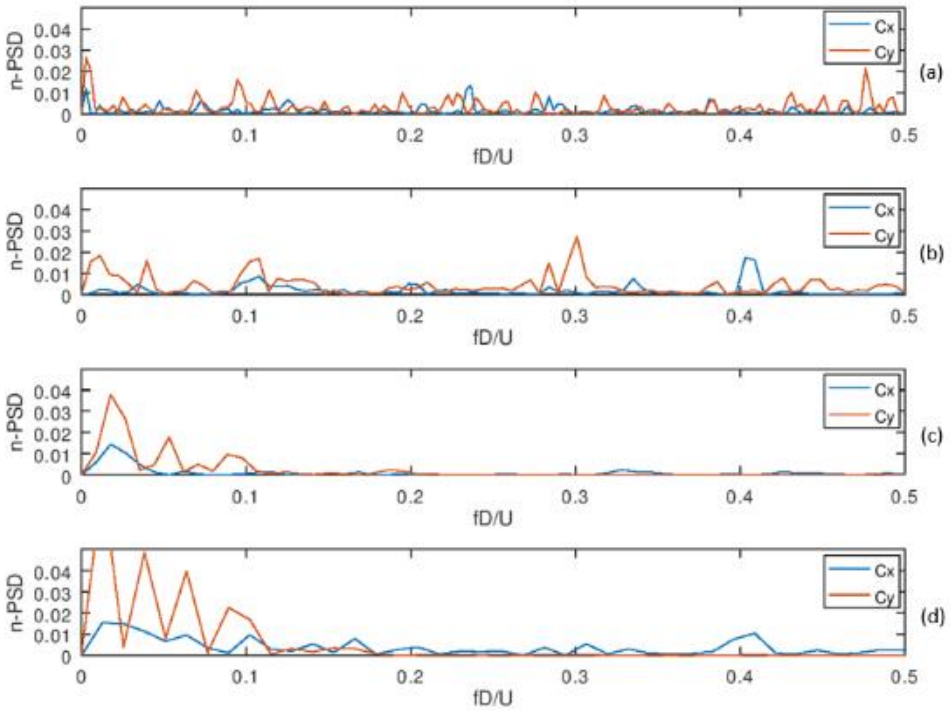

Figure 4.11 – Non-dimensionalized PSD for AR=0.5 (a)Fr=0.742, (b)Fr=0.434, (c)Fr=0.311, (d)Fr=0.0296

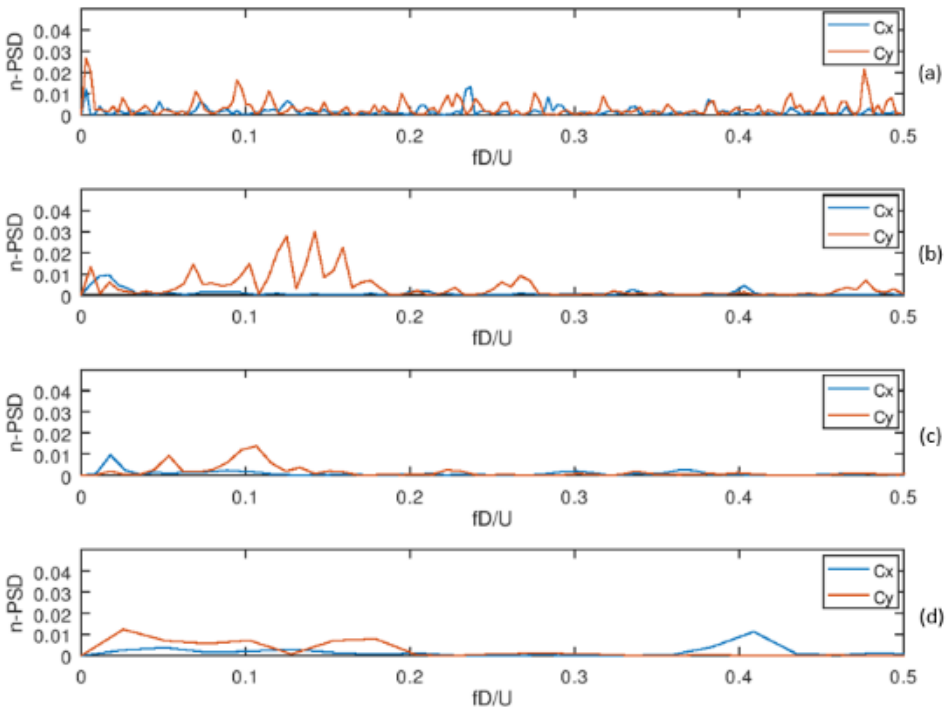

Figure 4.12 – Non-dimensionalized PSD for AR=1.0 (a)Fr=0.742, (b)Fr=0.434, (c)Fr=0.311, (d)Fr=0.0296

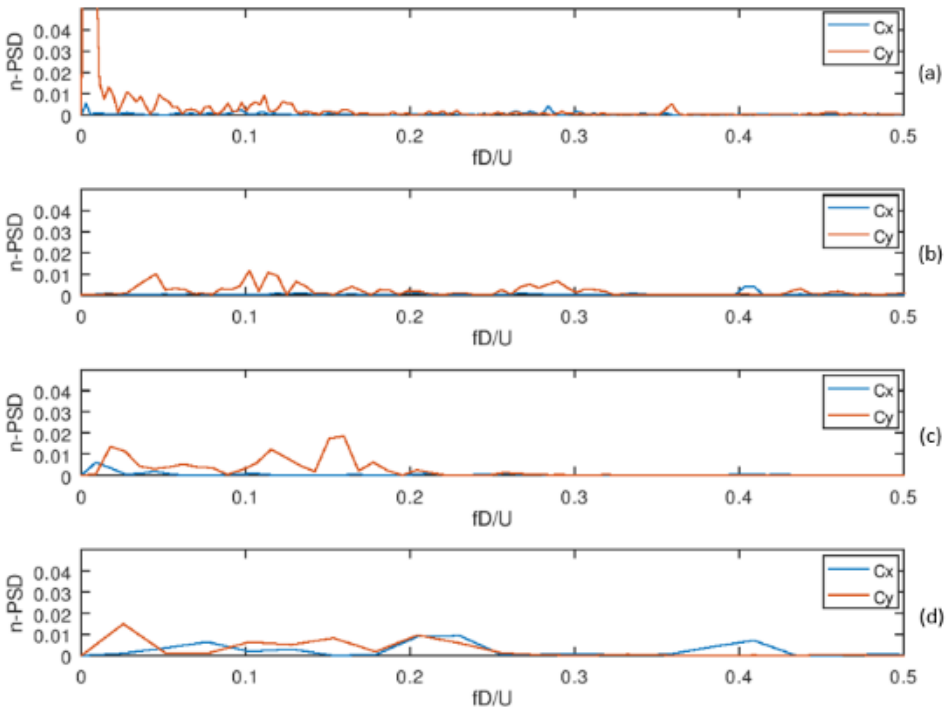

Figure 4.13 – Non-dimensionalized PSD for AR=1.5 (a)Fr=0.742, (b)Fr=0.434, (c)Fr=0.311, (d)Fr=0.0296

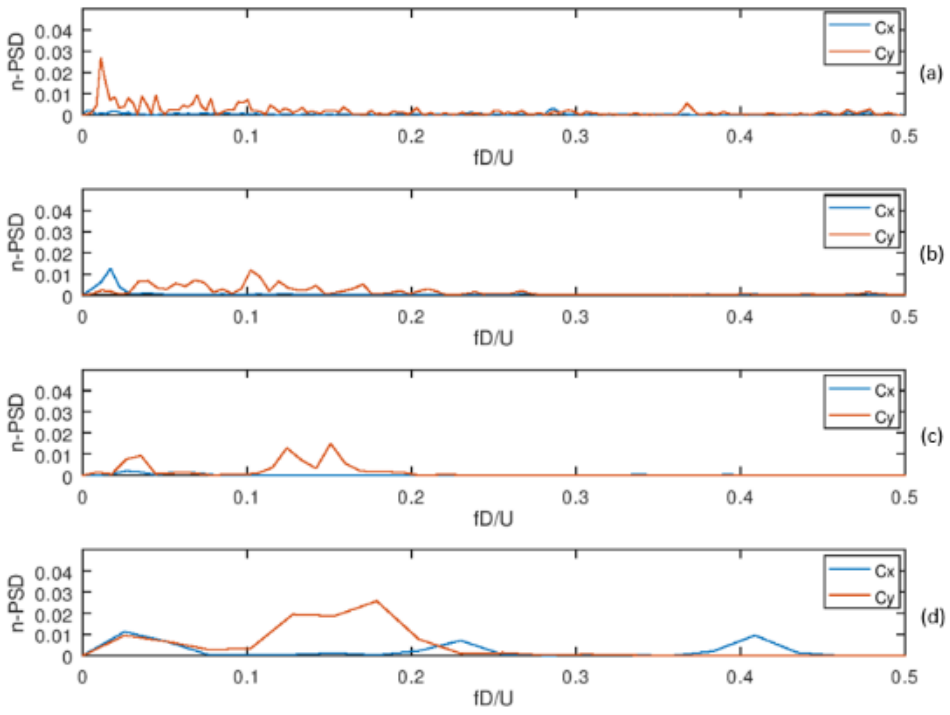

Figure 4.14 – Non-dimensionalized PSD for AR=2.0 (a)Fr=0.742, (b)Fr=0.434, (c)Fr=0.311, (d)Fr=0.0296

Figure 4.15 and 4.16 shows the positions of water surface around cylinder for each AR. 0 degree is the front stagnation position and 180 degree is the back stagnation position. The position H from still water level is non-dimensionalized with cylinder diameter D to h=H/D. The effect of AR on h looks small. Thus, the still water pressure on the cylinder is not affected by the interaction between free surface and free end. The wave run-up heights h(0) have good agreement with the Bernoulli's equation.

$$\frac{1}{2}mU^2 = \mathrm{mgH}$$

$$\therefore \mathrm{h(0)} = \frac{\mathrm{H}}{\mathrm{D}} = \frac{{V_x}^2}{2gD} = \frac{Fr^2}{2}$$

At Fr=0.742, $Fr^2/2$ is 0.275. At Fr=0.293, $Fr^2/2$ is 0.043.

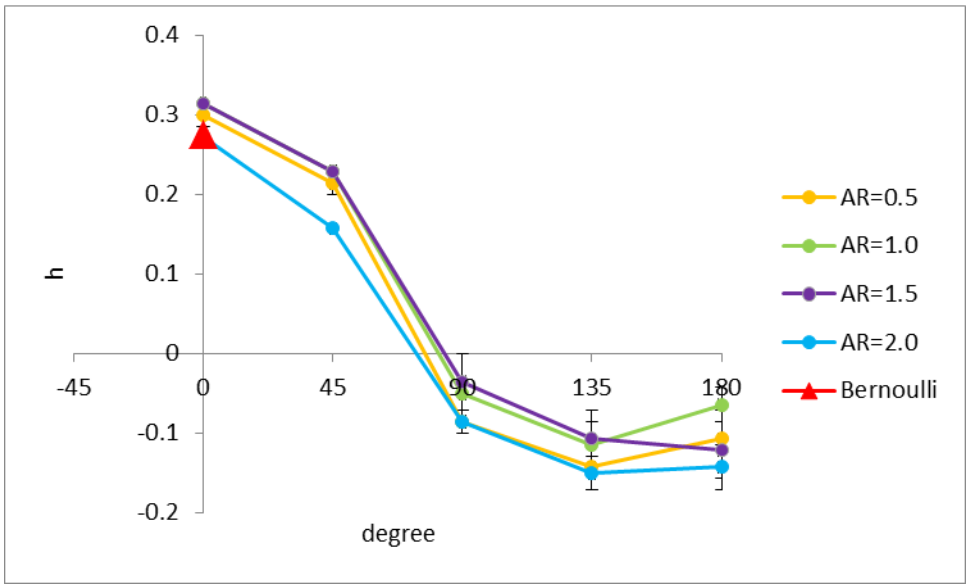

Figure 4.15 - Water positions around cylinder (Re=43000, Fr=0.742)

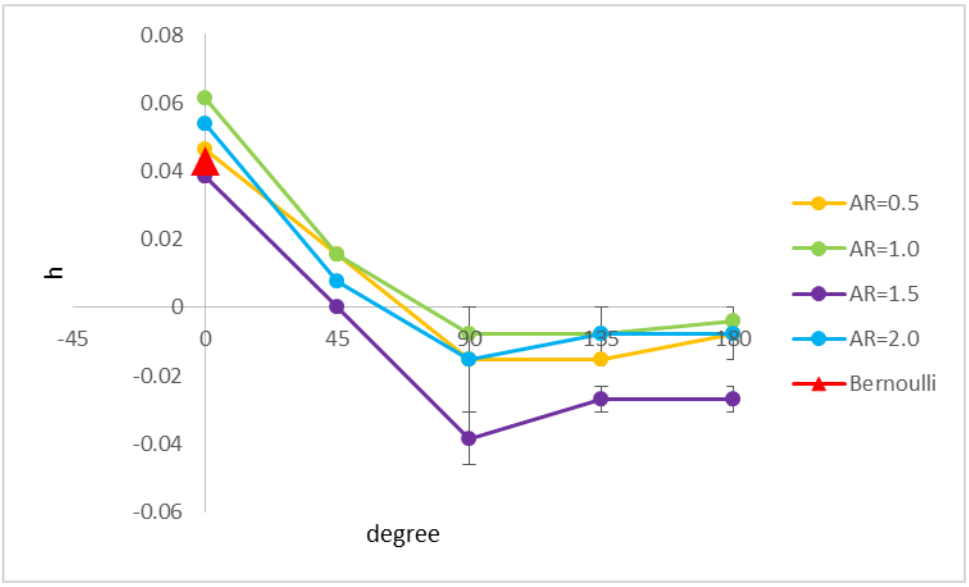

Figure 4.16 - Water positions around cylinder (Re=43000, Fr=0.293)

4.4 Reynolds number effect

Figure 4.17 – 4.19 show the mean drag coefficient, the RMS of drag coefficient, and the RMS of lift coefficient as a function of Re for each AR.
As it is widely known, for infinite circular cylinders, super-critical flow occurs at Re>4000000 and mean drag coefficient sharply decreases and the

Strouhal number increases. The mean drag coefficient at low aspect ratios also shows the decrease with Re increasing. This is clear for relatively larger aspect ratios, AR=1.5 and 2.0 due to the less free-end effect. For AR≧1.0, the decrease stops. This suggests that super-critical flow does not occur because the AR is small and the area of Kármán vortex shedding becomes smaller. This can be confirmed by PSD in Figure 4.20. There is the increase of Strouhal number to 0.2 for AR=2.0, but not for AR=1.0. Conversely, for Cx_rms and Cy_rms, there is a tendency that the force fluctuation increases as Re increases for AR=1.5 and 2.0. For relatively smaller aspect ratios, AR≦1.0, the force fluctuation is not so much changed over the range of Re in this experiment.

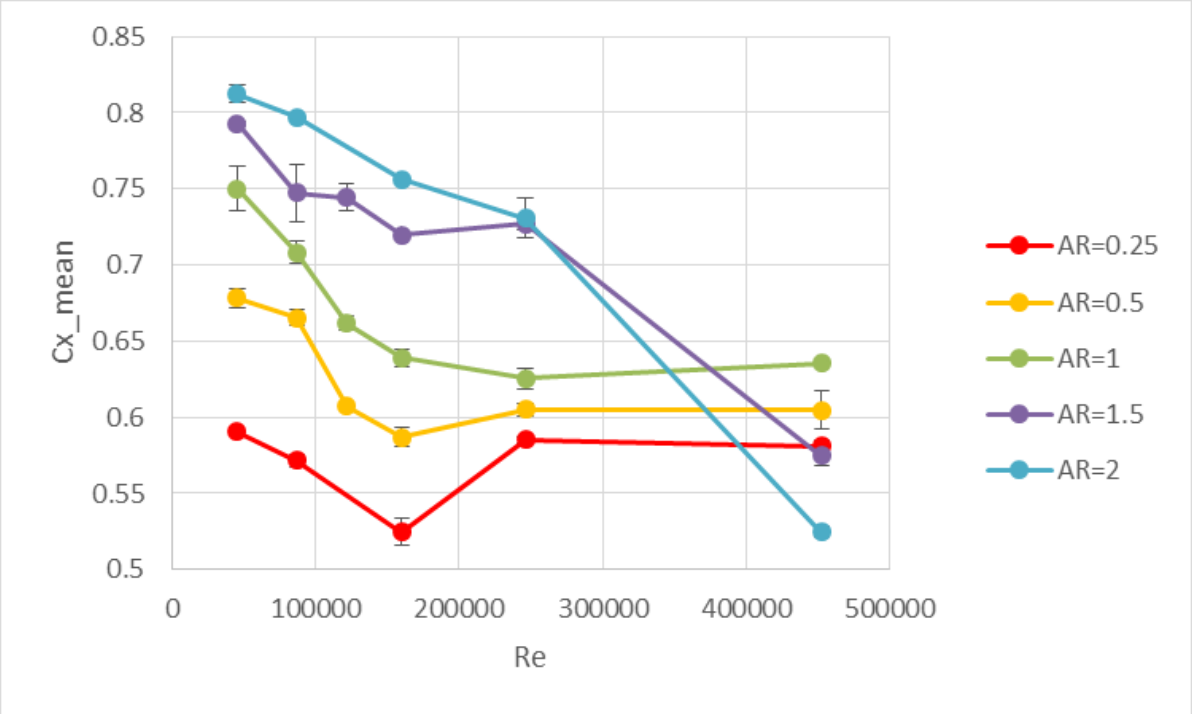

Figure 4.17 – Mean drag coefficient as a function of Reynolds number for each aspect ratio

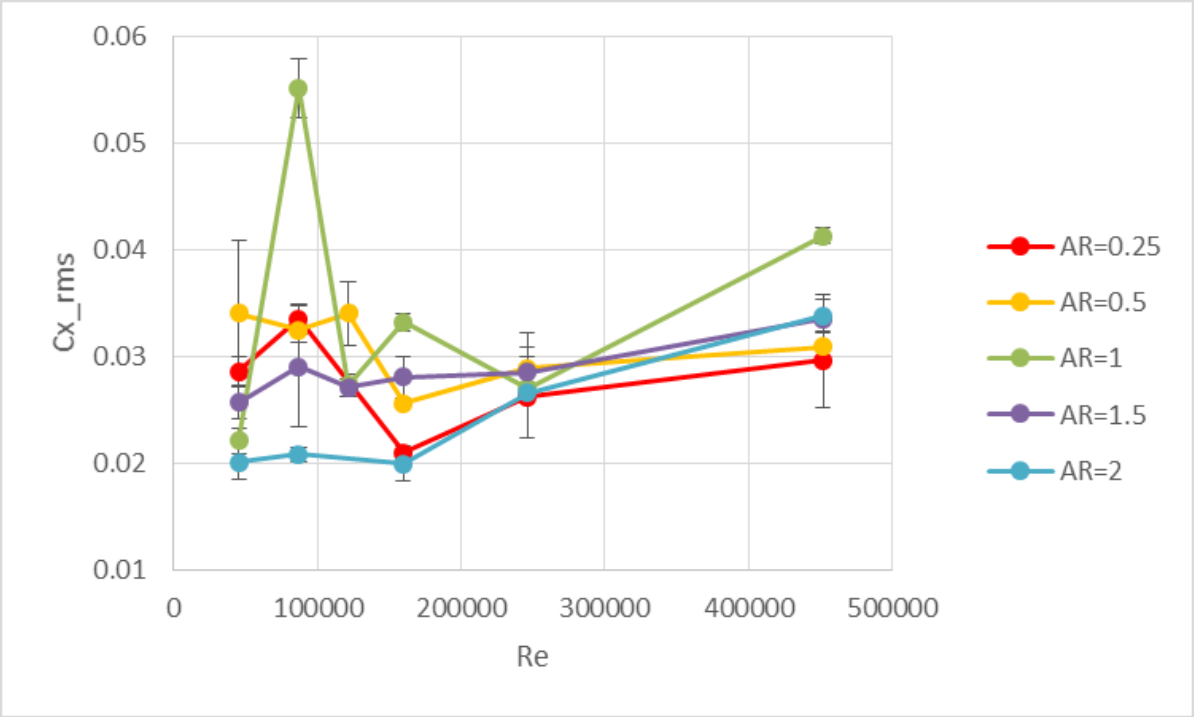

Figure 4.18 – RMS of drag coefficient as a function of Reynolds number for each aspect ratio

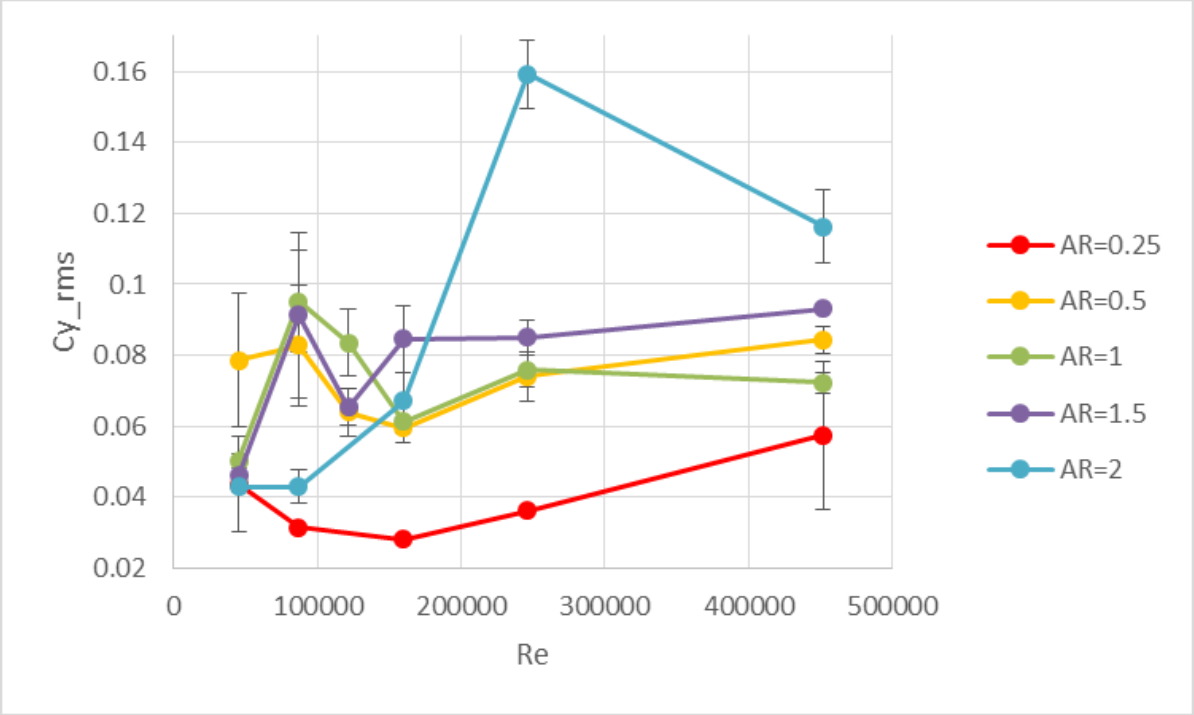

Figure 4.19 – RMS of lift coefficient as a function of Reynolds number for each aspect ratio

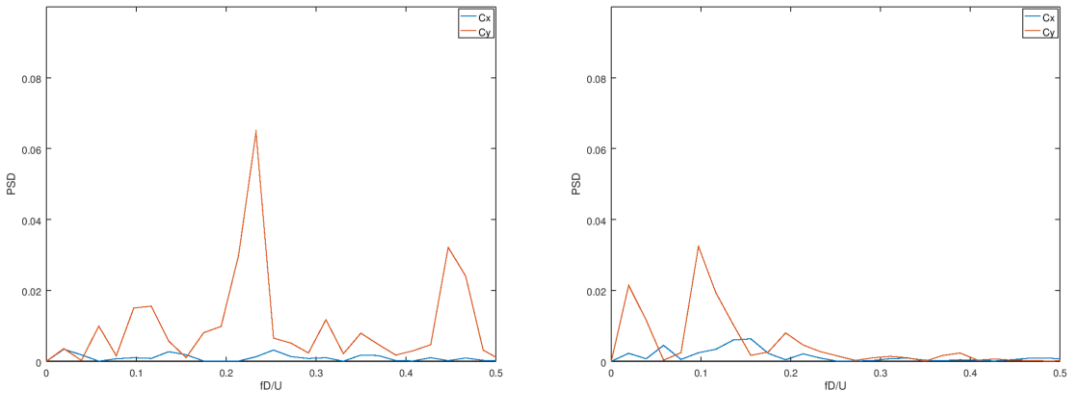

Figure 4.20 - Non-dimensionalized PSD of drag and lift coefficient at Re=452200 for AR=2.0 (left) and AR=1.0 (right)

4.5 Aspect ratio effect

In this section, we deal with the cases of D=0.1m. While Re and Fr are fixed, only AR is changed. Figure 4.21 shows the mean drag coefficient as a function of aspect ratio. As pointed out in the preceding studies, Cx_mean basically decreases with decreasing AR. This is because the recirculation from the bottom as shown in Figure 3.6 -3.9 contributes to the decrease of drag force.

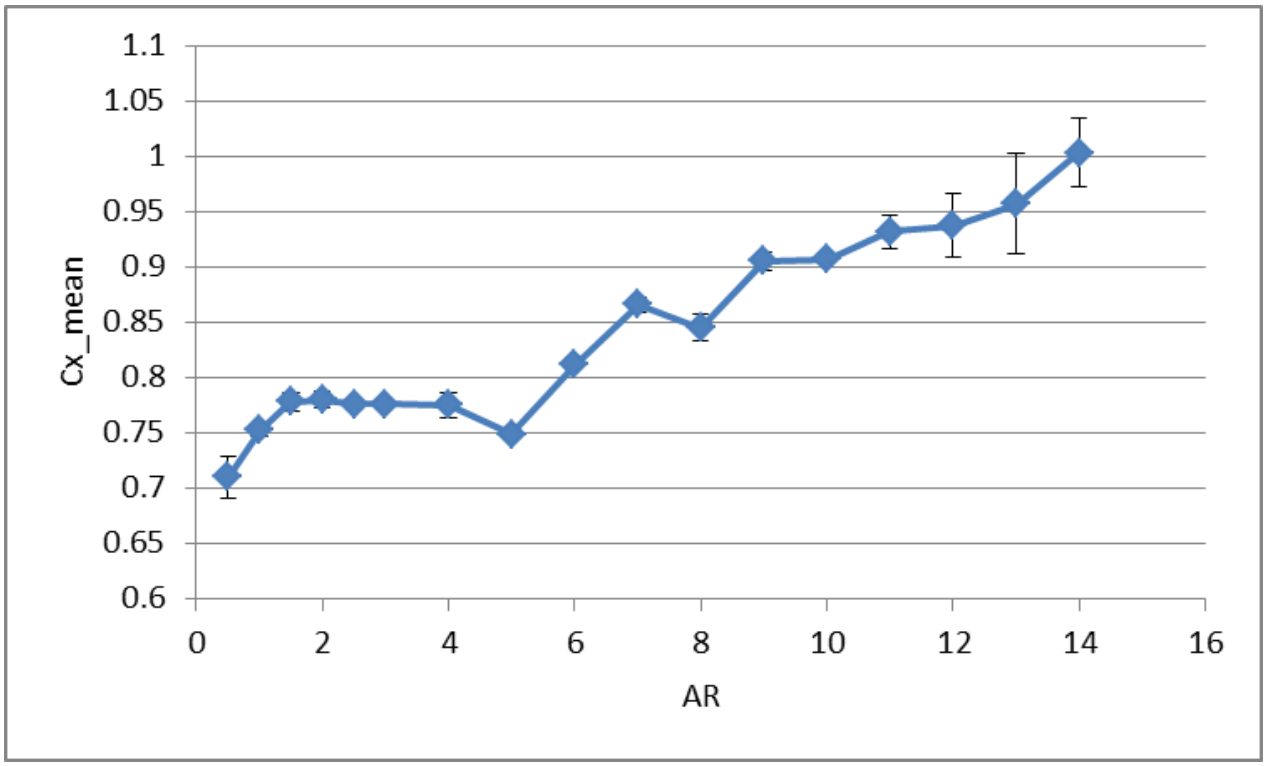

Figure 4.21 - Mean drag coefficient as a function of aspect ratio

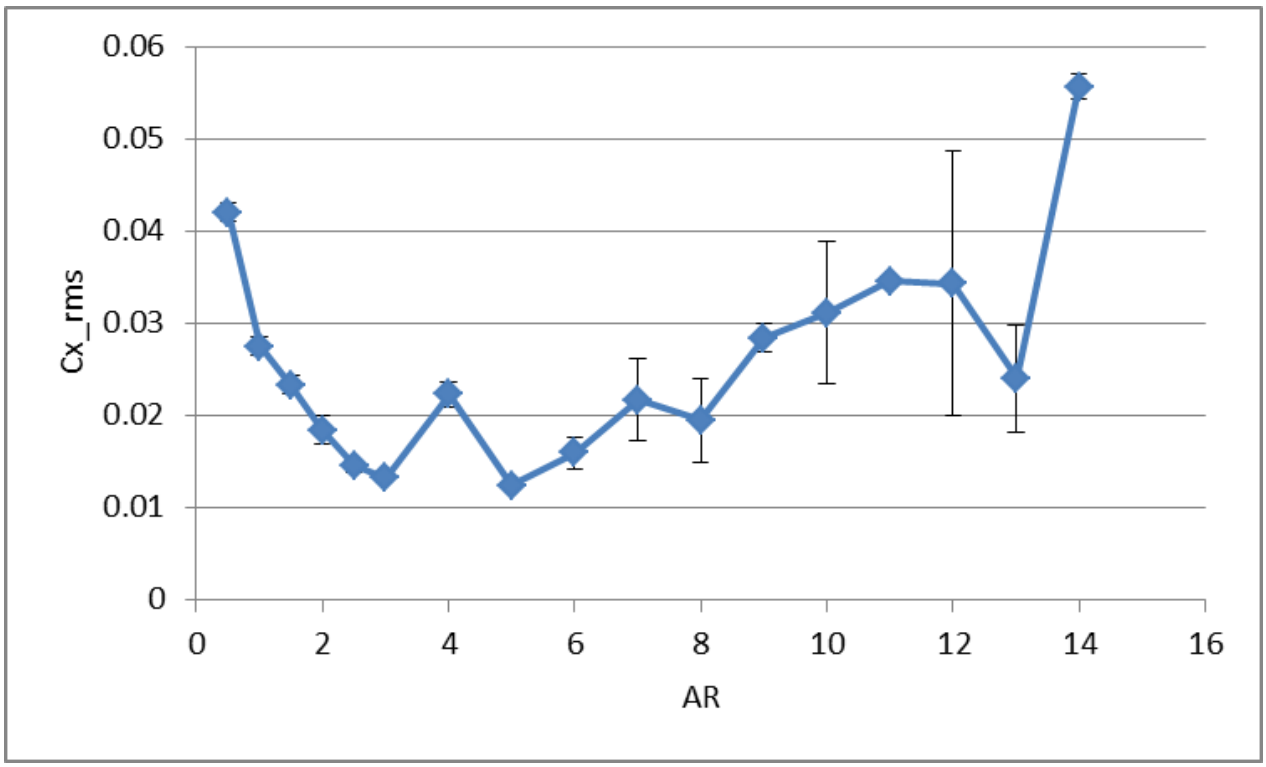

Figure 4.22 - RMS of drag coefficient as a function of aspect ratio

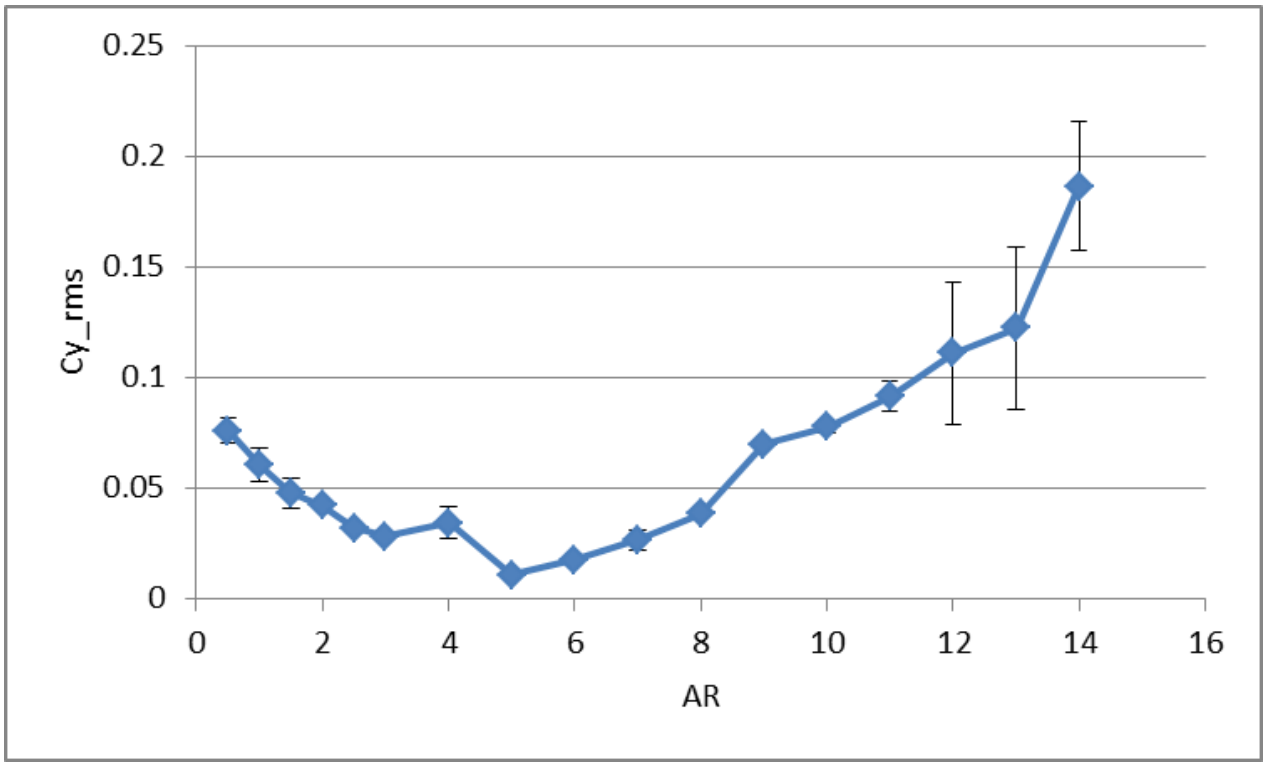

Figure 4.23 - RMS of lift coefficient as a function of aspect ratio

Figure 4.22 and 4.23 shows the RMS of drag and lift coefficient respectively. As AR increases, both decrease at AR<5 and increase at AR>5. This is because free-end effect decreases and the von Kármán vortex sheet develops gradually. Non-dimensionalized PSDs are presented in Figure 4.25 – 4.27. In figure 4.25, to see the small peaks clearly, we dare to limit the range of vertical axis. For high aspect ratio cases, there is a predominant peak at fD/U=0.2, the frequency of which means von Kármán vortex shedding. There is also a peak at fD/U=0.06~0.07, the end-cell induced vibration frequency mentioned in Chapter 2. As for middle and low aspect ratio cases, there is not a standing peak at fD/U=0.06~0.07. But there is energy around fD/U=0~0.1. This is considered that the three-dimensional properties are stronger as the AR becomes lower where free-surface and free-end effects become stronger. For very low ARs, AR≦1.5, PSDs include various range of frequencies, fD/U=0~0.5. This is because PSDs catch the frequencies by the free-surface motion. Benitz *et al.* (2016) stated that PSD does not have energy at AR<3. The difference is caused by the Fr value. In their experiment, Fr is 0.65 and there might be vortex attenuation by free-surface effect.

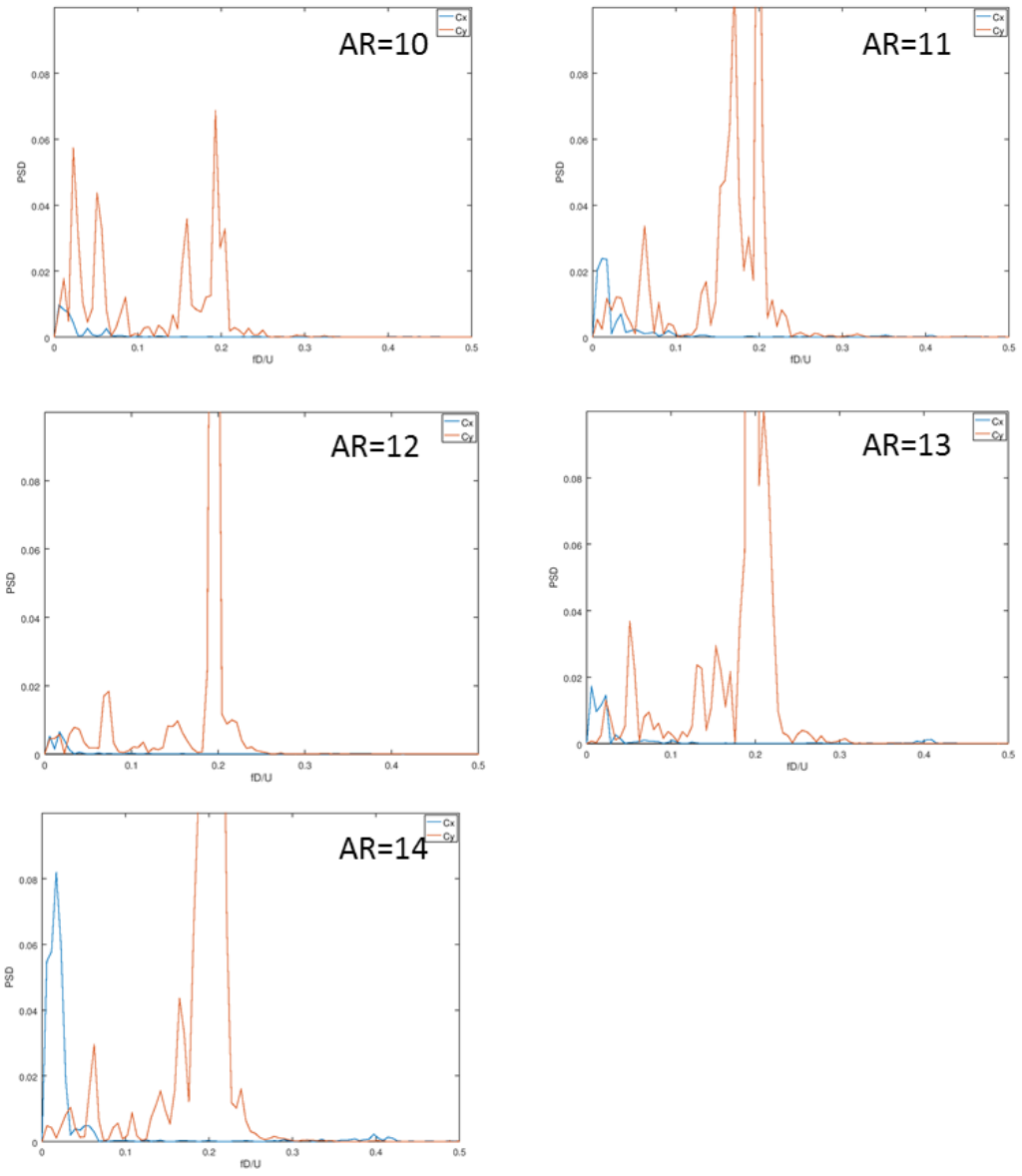

Figure 4.24 - Non-dimensionalized PSD of drag and lift coefficient at Re=43000 for high aspect ratios

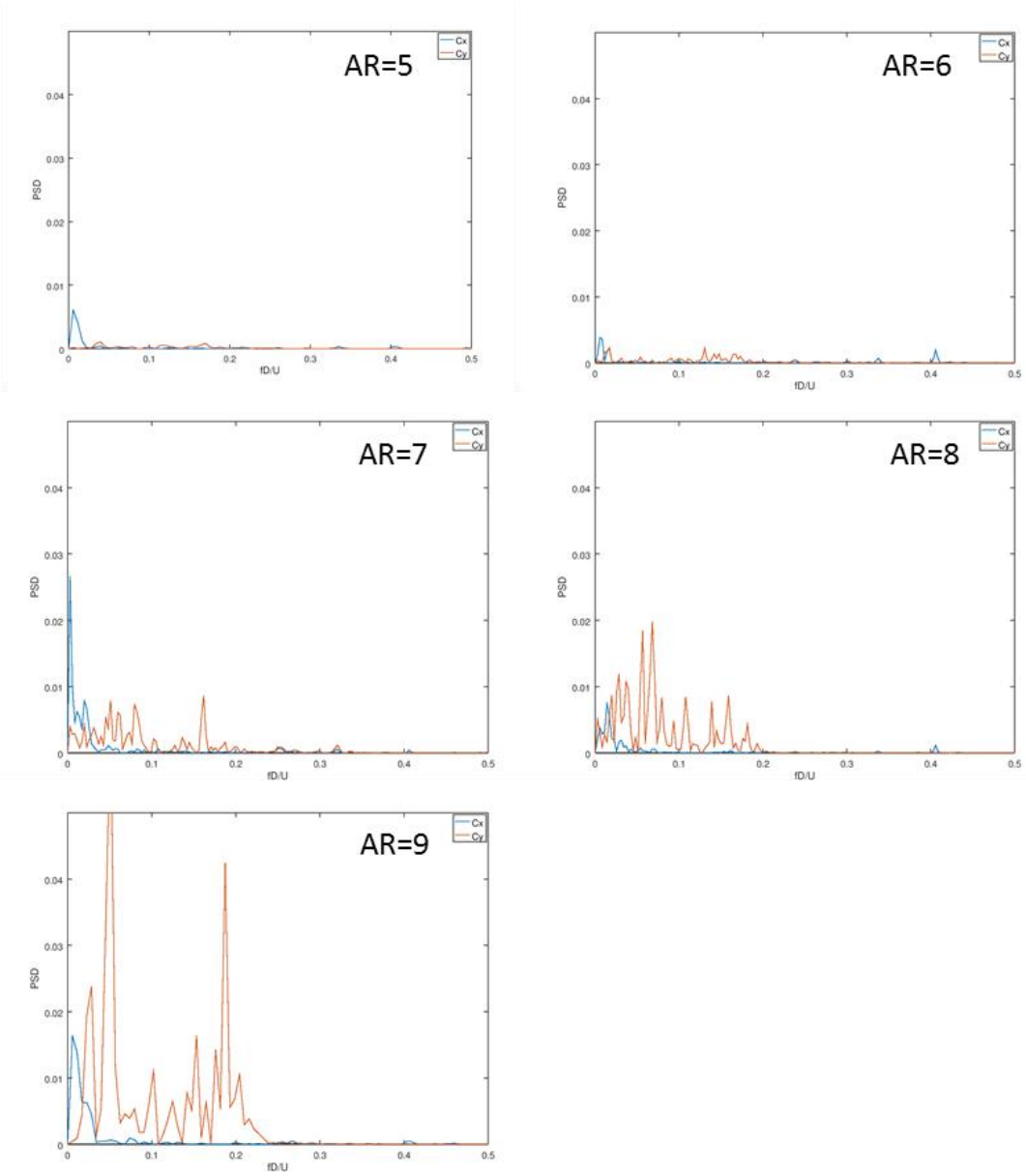

Figure 4.25 - Non-dimensionalized PSD of drag and lift coefficient at Re=43000 for middle aspect ratios

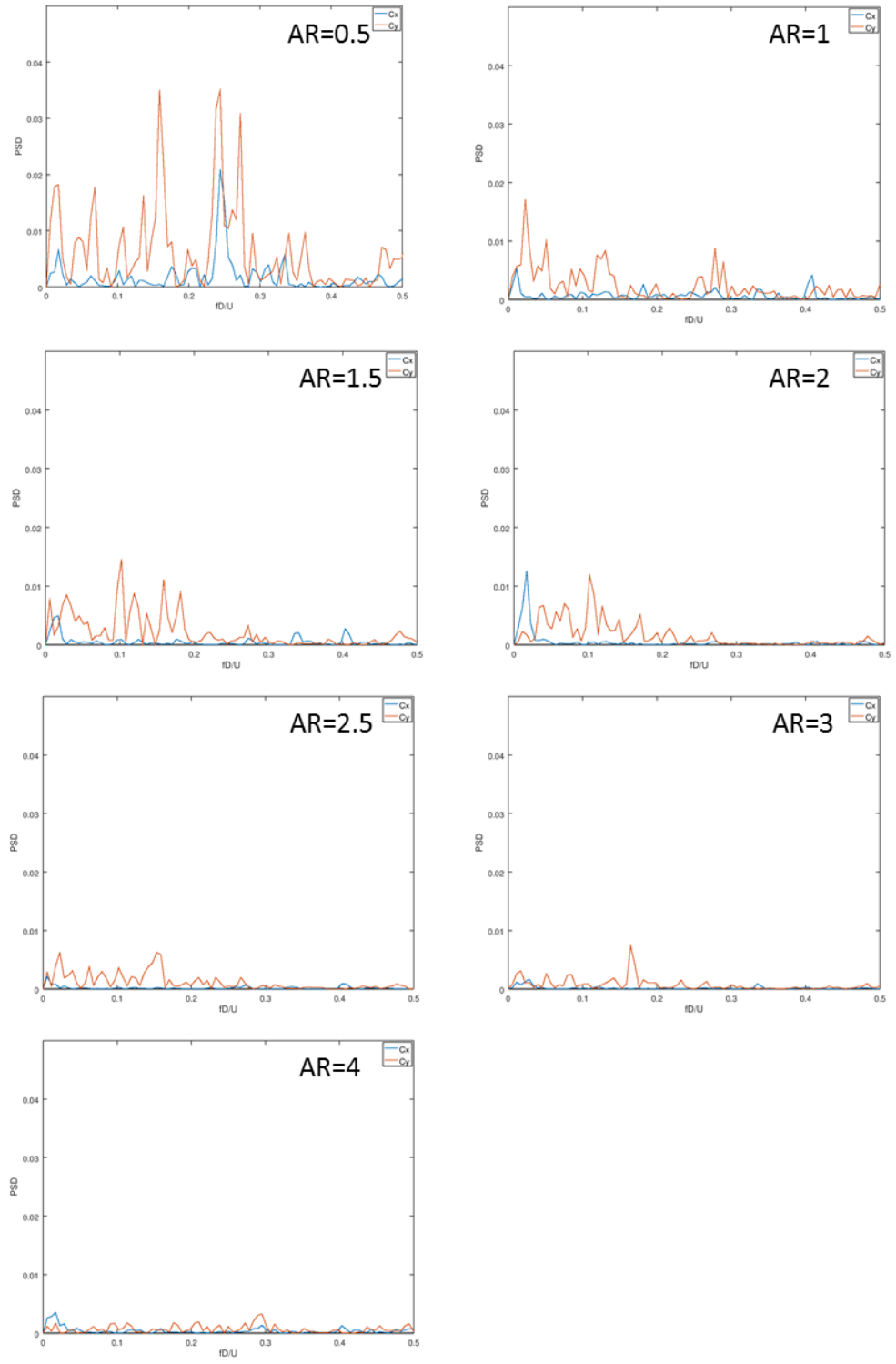

Figure 4.26 - Non-dimensionalized PSD of drag and lift coefficient at Re=43000 for low aspect ratios

4.6 Froude number effect (free-surface vs no-slip conditions)

As shown in Figure 4.30, flow velocity profile at the centerline of a water channel was measured by a velocimeter for both free-surface conditions and no-slip conditions at the depth of 25mm, 50mm, and 100mm from the still water level. The results are presented in Figure 4.30 and 4.31. At this recirculating water channel, the velocity[m/s] is set as frequency[Hz] by an inverter.. The tendency that the velocity is higher as the depth is deeper can be found for both cases. Figure 4.33 - 4.35 are the re-organized graphs of Figure 4.31 & 4.32 for each depths. The difference of the velocity between free-surface and no-slip conditions is larger as the depth is shallower and near the board. Although this is the wall effect, the effect on the velocity is very small. In this experiment, the inverter frequency was adopted corresponding to the free-surface conditions for both boundary conditions.

Figure 4.27 - Recirculating water channel at UTokyo, Hongo

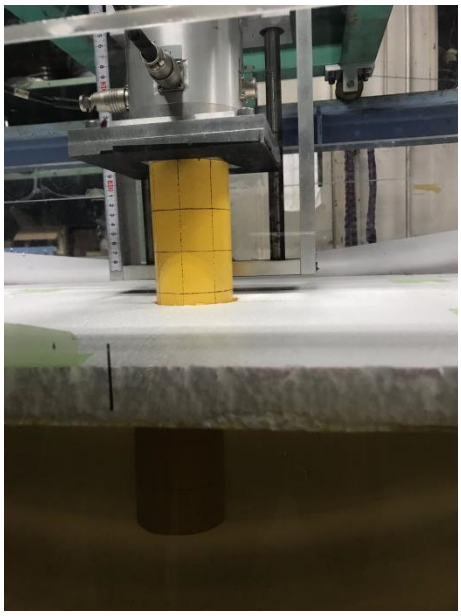

Figure 4.28 – A scene of force measurement in a circulating water channel

Figure 4.29 - Scenes of velocity profile measurement by an anemometer in a circulating water channel

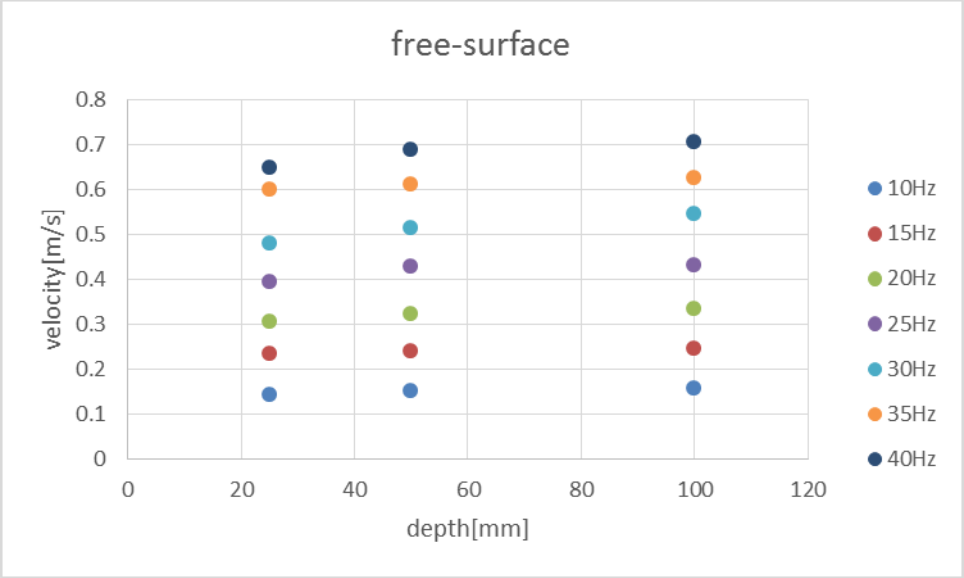

Figure 4.30 - Flow velocity corresponding to each inverter frequency at different depths (free-surface conditions)

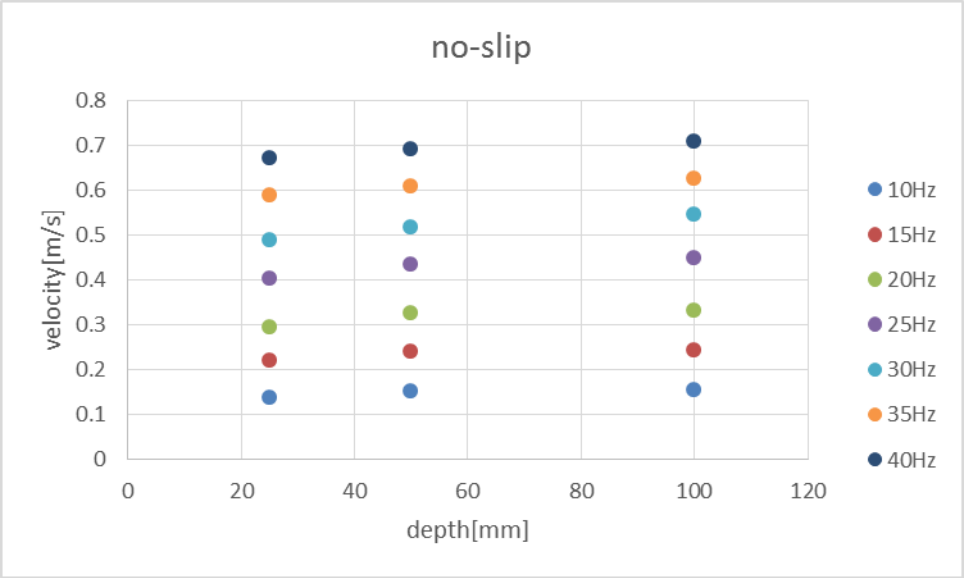

Figure 4.31 - Flow velocity corresponding to each inverter frequency at different depths (no-slip conditions)

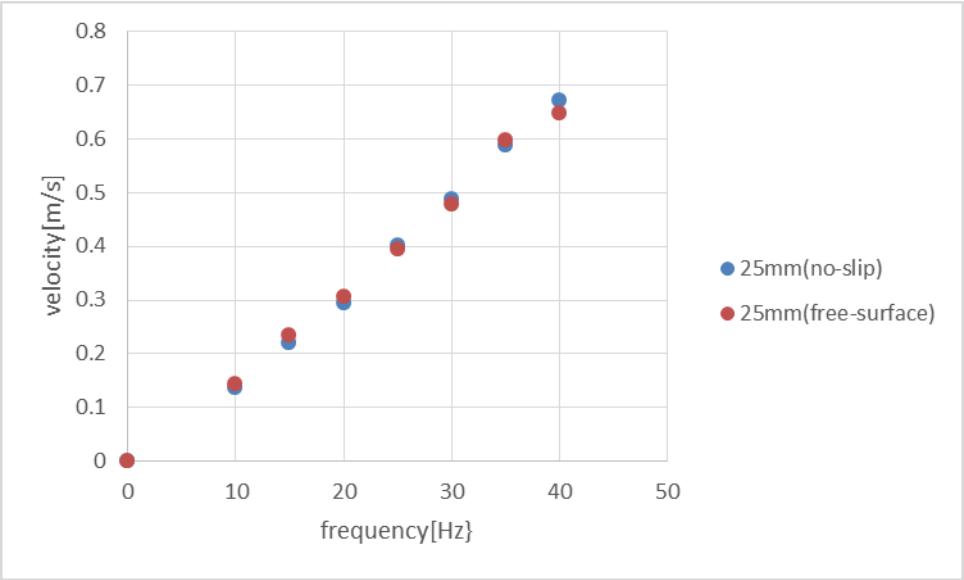

Figure 4.32 - Flow velocity corresponding to each inverter frequency at the depth of 25mm

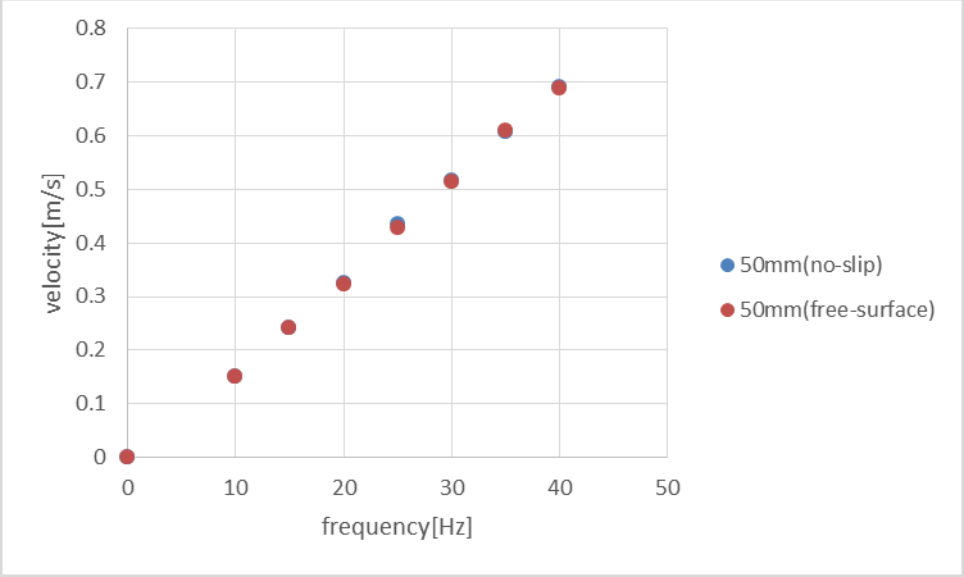

Figure 4.33 - Flow velocity corresponding to each inverter frequency at the depth of 50mm

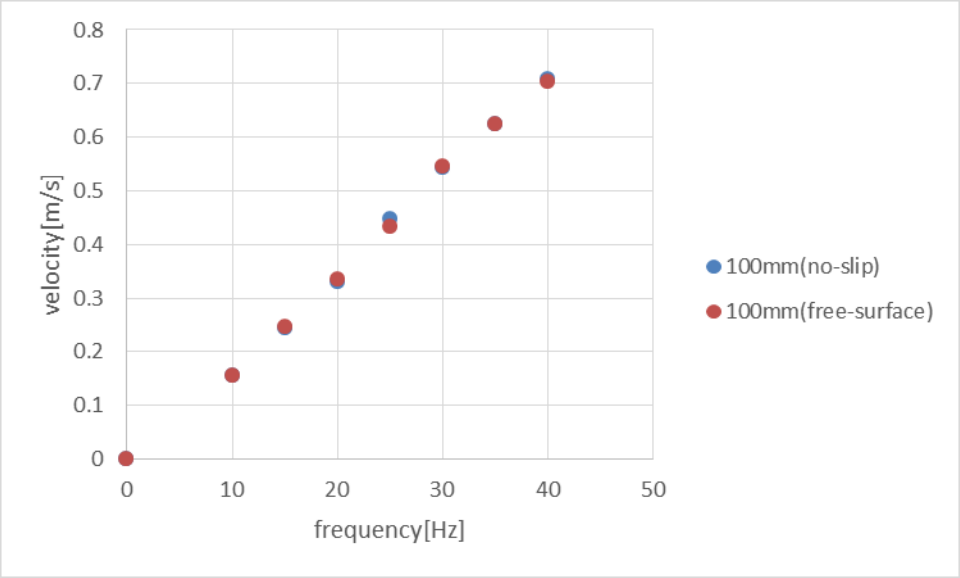

Figure 4.34 - Flow velocity corresponding to each inverter frequency at the depth of 100mm

Table 4.3 - Experimental conditions in a recirculating water channel

D[m]	Fr	AR
0.07	0.742	0.5, 1.0, 1.5, 2.0
0.13	0.293	0.5, 1.0, 1.5, 2.0

The experimental conditions are listed in Table 4.3. Two Froude numbers were tested at the same Re of 43000. Results are presented in Figure 4.36 – 4.41. There is little difference between Fr=0.293 and no-slip cases for each values, Cx_mean, Cx_rms and Cy_rms. On the other hand, the difference is remarkable between Fr=0.742 and no-slip cases. Similar to the results in section 4.3, Cx_mean is larger and Cx_rms and Cy_rms are smaller at Fr=0.742. Basically the up and down mechanism is considered to be the same. As mentioned above, the wall effect on the velocity is thought to be small. However, we need to consider that there is a possibility that the horseshoe vortex affects the results in no-slip conditions as shown in Chapter 2.

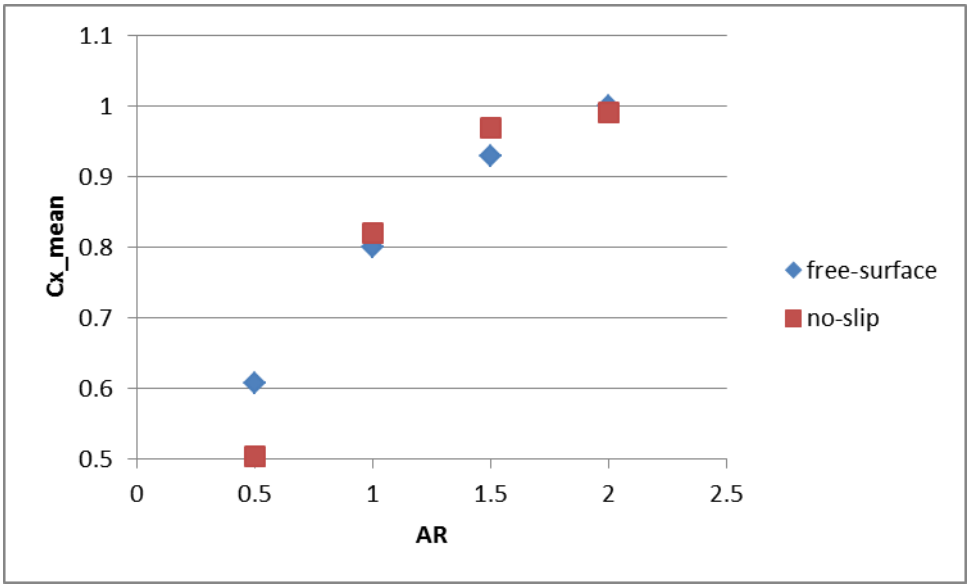

Figure 4.35 - Mean drag coefficient as a function of aspect ratio at Fr=0.293 for free-surface and no-slip conditions

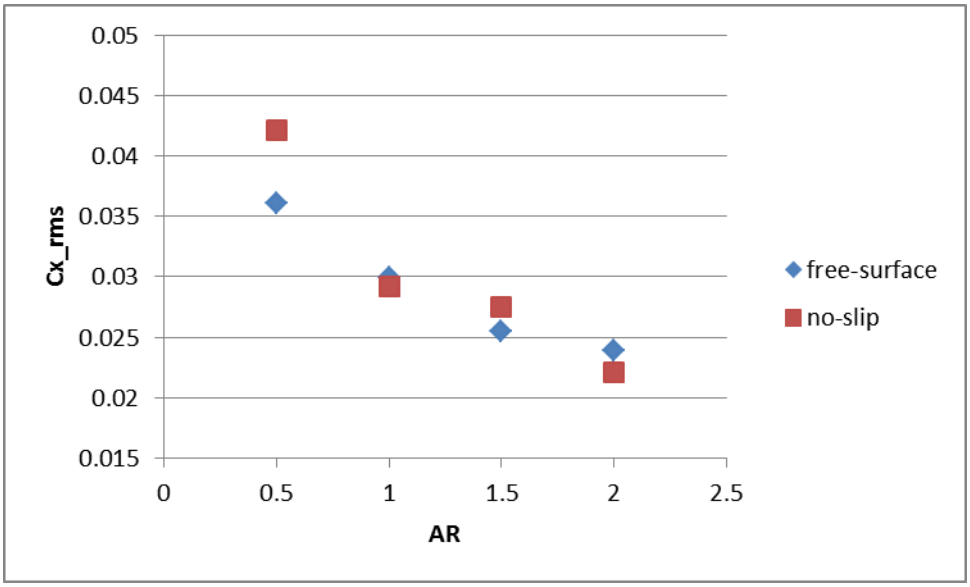

Figure 4.36 - RMS of drag coefficient as a function of aspect ratio at Fr=0.293 for free-surface and no-slip conditions

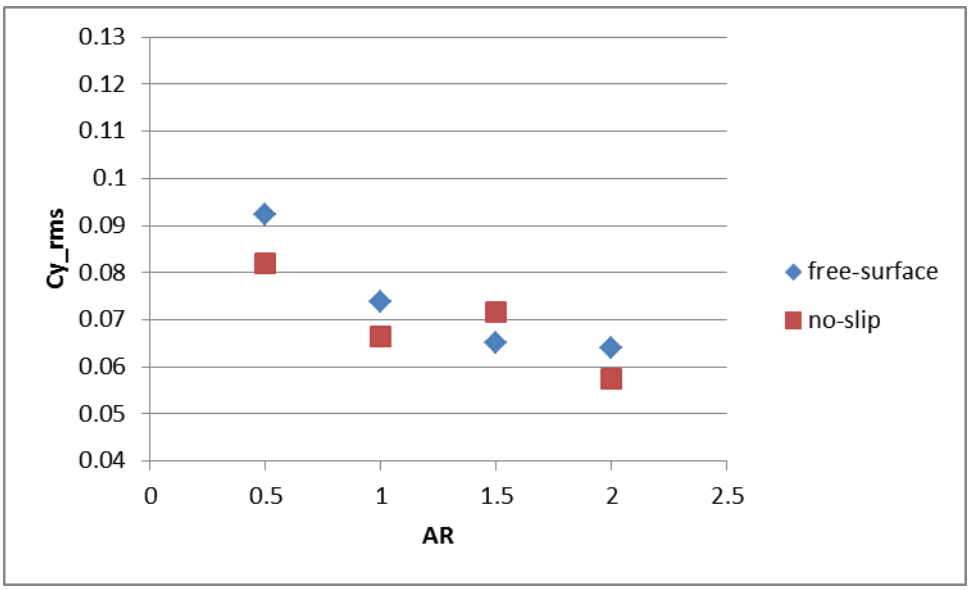

Figure 4.37 - RMS of lift coefficient as a function of aspect ratio at Fr=0.293 for free-surface and no-slip conditions

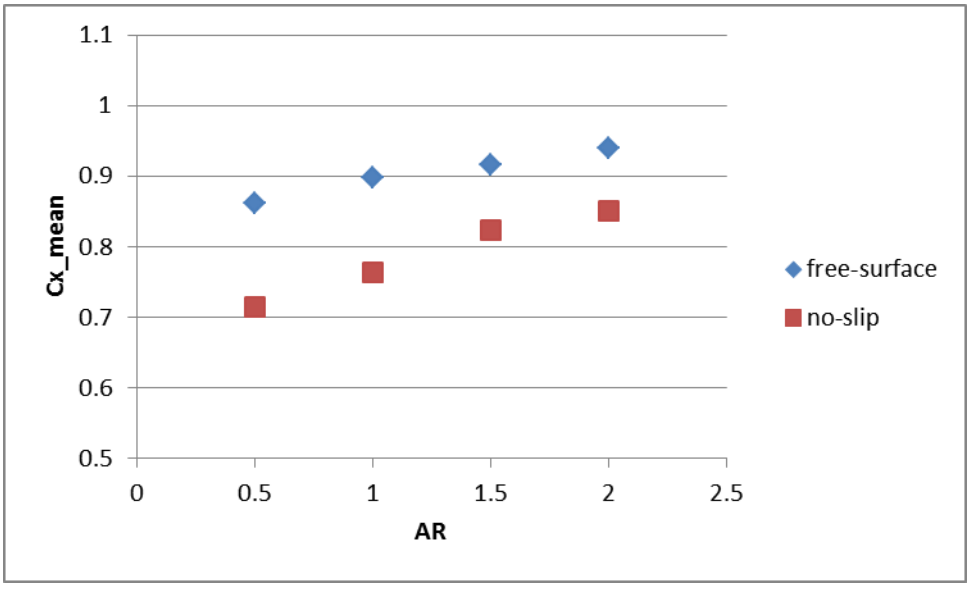

Figure 4.38 - Mean drag coefficient as a function of aspect ratio at Fr=0.742 for free-surface and no-slip conditions

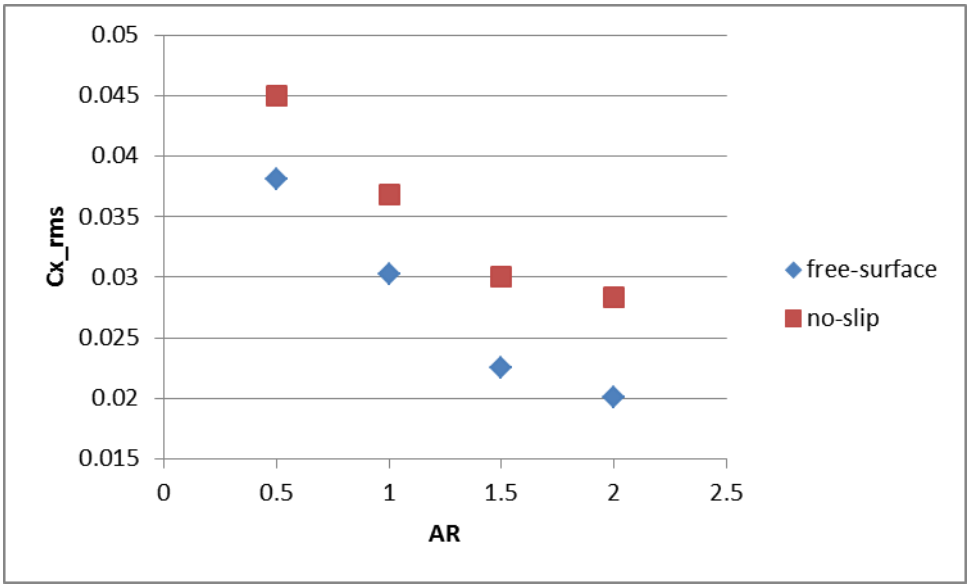

Figure 4.39 - RMS of drag coefficient as a function of aspect ratio at Fr=0.742 for free-surface and no-slip conditions

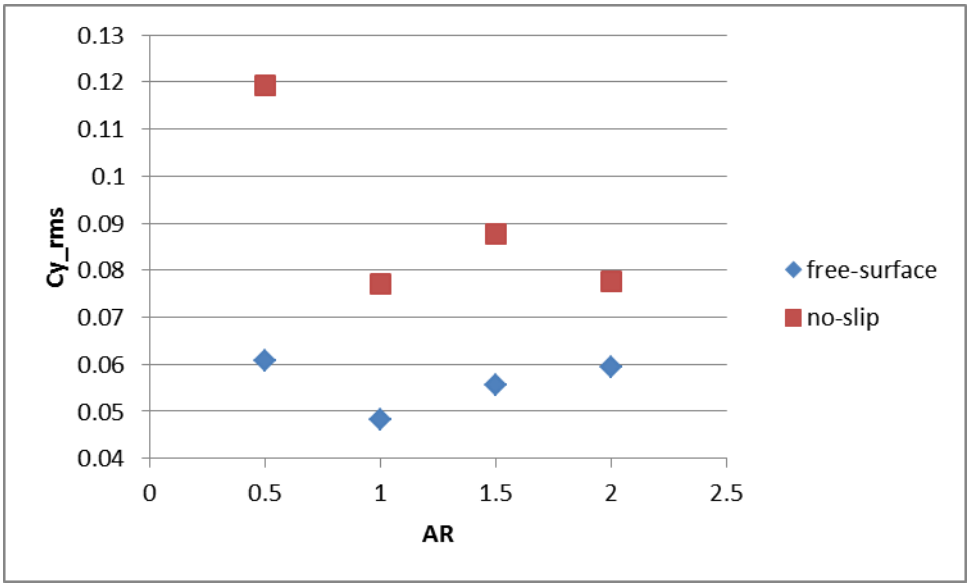

Figure 4.40 - RMS of lift coefficient as a function of aspect ratio at Fr=0.742 for free-surface and no-slip conditions

Chapter 5 Discussions

In this chapter, we try to expand discussions based on two experiments results.

5.1 AR effects

AR effect is mentioned in section 4.5 in Chapter 4. As shown in Figure 4.22 and 4.23, the RMS of Cx and Cy decreases for AR<5 and increases for AR>5 with increasing AR. This can be expressed by a simple model. Assuming that the dimensionless fluctuating parts around the free end by arch type vortex etc. has the constant value C and the force fluctuation by von Kármán vortex sheet which develops from AR=a, has the constant value K per AR, the coefficient fluctuation is expressed as:

$$Cx_{rms} \ or \ Cy_{rms} = \sqrt{\left(\frac{C}{AR}\right)^2 + \left\{\frac{K}{AR}\cdot(AR-a)\right\}^2} \quad (AR > a) \quad , \quad \left|\frac{C}{AR}\right| \quad (AR > a) \quad (1)$$

where K is the coefficient for infinite length cylinder. a is the displacement length due to free-end effect. AR-a means the Kármán vortex shedding area length. C and K is the value already divided by $\frac{1}{2}\rho(UD)^2$. This behavior is presented in Figure 5.1. This is based on the premise that Kármán vortex from the side of the cylinder and arch type vortex etc. from the bottom of the cylinder can be divided, which means that they have different frequencies. As it can be seen in Figure 4.24, they can be separated for high aspect ratios. The decrease of fD/U with decreasing AR was confirmed and the border to separate the two types of vortices was not clearly. Then, this model may not be perfect but it can be practical. Kármán vortex shedding with dimensionless frequency lower than 0.2 can be confirmed for L/D=2.0 and 1.0 in PIV measurement. It can be inferred from Figure 4.22 and 4.23 results that the contribution of Kármán vortex with decreased frequency to force fluctuation is not as large as two-dimensional Kármán vortex. On the other hand, Kármán vortex, the Strouhal number of which is 0.2 has strong effect on force fluctuation.

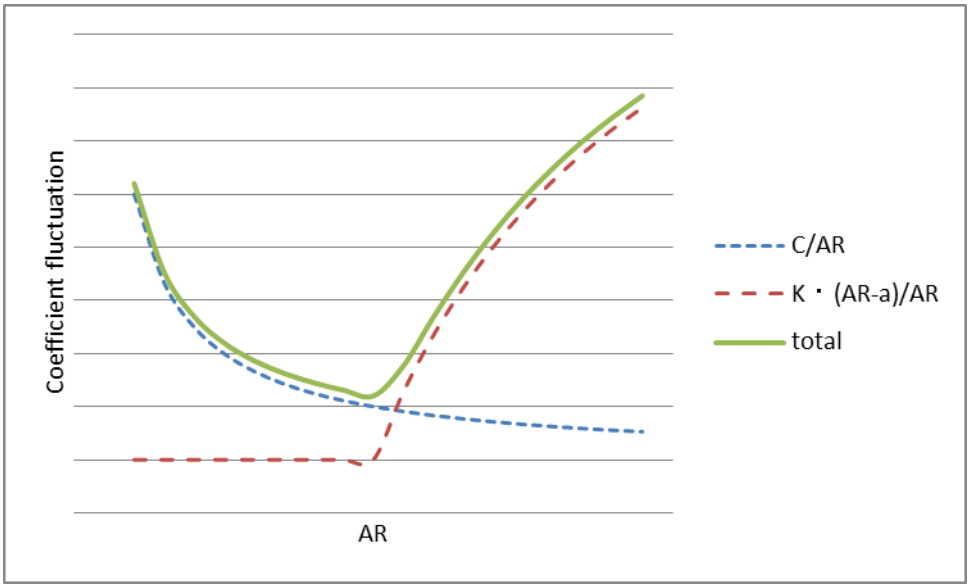

Figure 5.1 - Example of coefficient fluctuation model as a function of aspect ratio

For most cases of Re=43000 and AR≦3, RMS of the lift coefficient is largest at AR=0.5 as shown in Figure 4.9 and 4.10. To compare the cases of AR=0.5 and 0.3 in PIV measurement, the trailing vortex cannot be confirmed at AR=0.3. On the other hand, it can be confirmed at AR=0.5. As Gonçalves *et al.* (2015) stated that for L/D=0.2, the free end are not able to alternating forces, the vortex around free end is weaken at L/D<0.5. This may be because the arch-type vortex penetrates the free surface because of the lower AR and loses energy.

As for mean drag coefficient, basically it increases with increasing AR and gradually at low ARs. This is due to the recirculation as shown in Figure 3.6 - 3.9.

5.2 Fr effects.

As discussed in Chapter 4, Fr effect can be considered into 3 parts namely, Fr<0.05, 0.05<Fr<0.5, 0.5<Fr..

Surprisingly, near the free-slip condition, Fr<0.05, mean drag coefficient was larger at AR≧1.5. This may be because the recirculation from the bottom

becomes weaker suppressed by the nearly free-slip condition and the drag coefficient increases. However, it is not observed for AR ≦ 1.0. This is considered the interaction effect between free end and free surface condition. That is, for AR ≦ 1.0, the free-end effect is more remarkable and the suppression effect is not changed so much even if the Fr gets closer to 0, free-slip condition. Or following the discussion above, as AR is larger, the flow does not penetrate the free surface and does not lose energy. However, Fukuoka et al. (2016) stated that the recirculation is weaken as Fr increases, and the reason is still disputable.

Within the Froude number of 0.05 to 0.5, the effect was almost the same. However, compared to Fr=0.0296, there is effect to attenuate the vortex. The inclination of the vortex rotation angle in Figure 3.11 has something to do with this. It is probable that this inclination narrows the vortex shedding area. At Fr>0.5, the forces catch the frequency by free-surface motion.

According to Hay (1947), the depression depth h(180)=H(0)/D is approximated as $0.286Fr^2$ for the range of Fr>1. Assuming that the ratio h(180)/h(0) is constant, the increase of still water force by water running up and down around the cylinder is proportional to Fr^2/AR.
Simply thinking, for the prismatic, the increase of still water force is

$$F_f = \int_{h(0)}^{h(180)} \rho g z D \ dz \ = \frac{1}{2}\rho g D (1+\alpha)^2 h(0)^2$$

where $\alpha = h(180)/h(0)$. Since h(0) is $Fr^2/2$, the dimensionless F_f, C_f is

$$C_f = \frac{F_f}{\frac{1}{2}\rho L D U^2} = \frac{(1+\alpha)^2}{4} \cdot \frac{U^2}{gL} = \frac{(1+\alpha)^2}{4} \cdot \frac{Fr^2}{AR}$$

From force measurement results, Cx_mean does not increase at 0.05<Fr<0.5 as shown in Figure 4.6. Therefore, the increase of still water force by water running up and down around the cylinder can be neglected even for low aspect ratios, AR≦3.

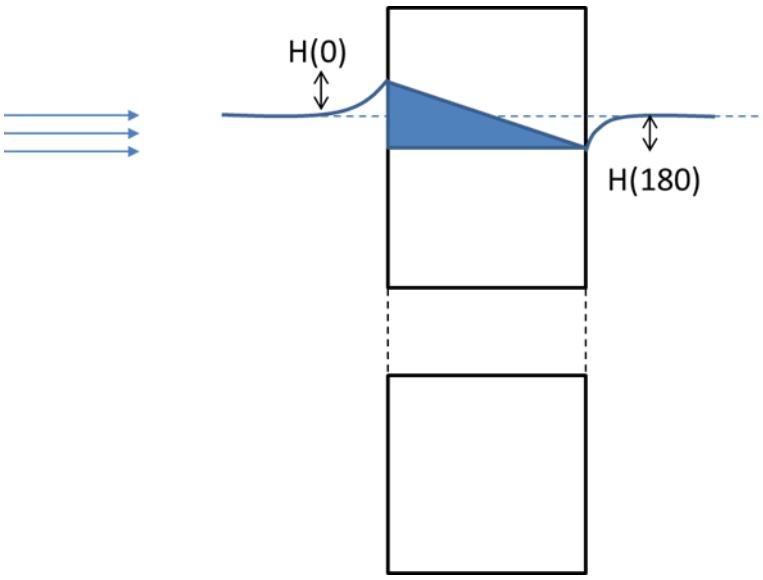

Figure 5.2 Run-up height and depression depth around the prismatic

Re effects are already discussed enough in Chapter 4.

From all discussions so far, we can sketch the flow around half-submerged cylinders with different low aspect ratios, lower than 2.0. See Figure 5.3 and 5.4.

Six important points should be noted.

A: Free-surface effect. The free-surface has an effect of attenuating the vortex below. Front run-up and rear depression is remarkable as Fr increases. The increase of still water force driven by the run-up and depression can be neglected at $0.05<Fr<0.5$.

B: The separation flow from near the free-surface is suppressed by free-surface and the rotation axis of vertical vortex is inclined. It is preeminent at $AR \geqq 1.0$.

C: Kármán vortex with decreased frequency, $fD/U=0.1\sim0.18$. This can be found at $AR \geqq 1.0$. However, at $Fr>0.5$, it is diminished.

D: Arch-type vortex. The dimensionless frequency is 0~0.1. At AR=2.0 and 1.0, as Zhu et al. (2017) pointed out, the shape is like M. At AR=0.5 and 0.3,

the shape is U. It can be found by Figure 3.11 and 3.18 – 3.21. The effects on the flow is remarkable around half diameter from the bottom.

E: Tip vortex from the front corner of the cylinder.

F: Trailing vortex. This is below the arch-type vortex. The rotating direction is opposite to tip vortex. At AR=0.3, it cannot be observed clearly.

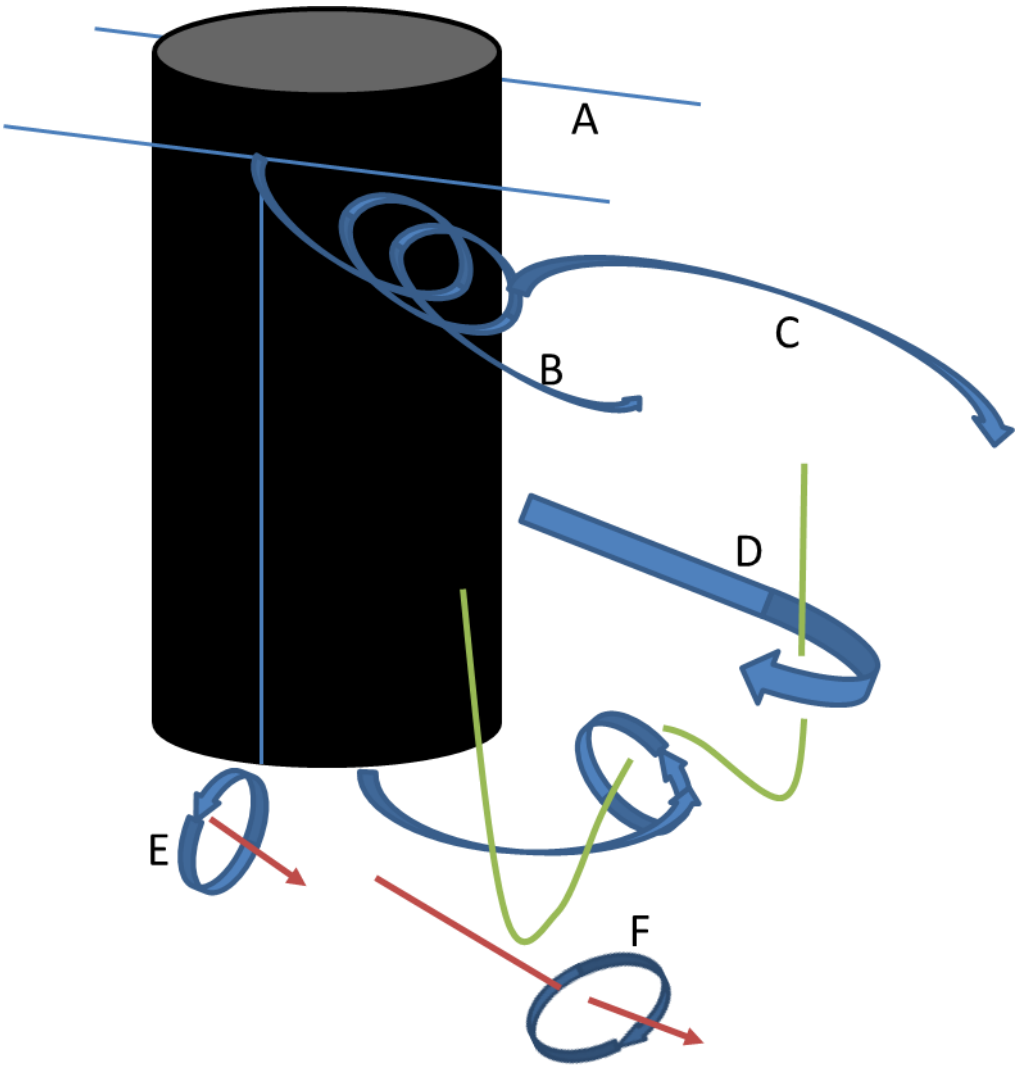

Figure 5.3 - Models of characteristic flow around half-submerged circular cylinders with aspect ratio of 2.0

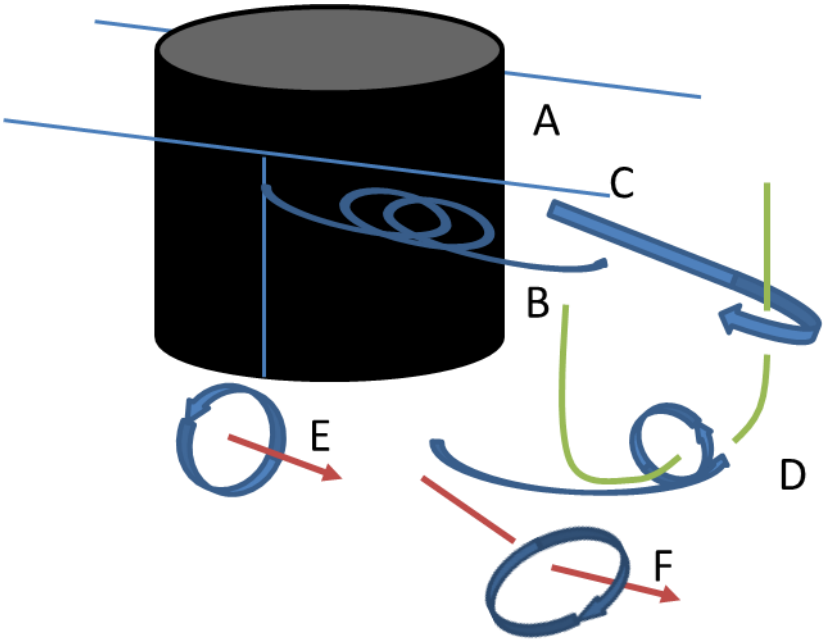

Figure 5.4 - Models of characteristic flow around half-submerged circular cylinders with aspect ratio of 0.5

Chapter 6 Conclusions

Most of the points presented in this chapter have been dealt with so far. Nevertheless, this chapter aims to summarize the main findings and contributions of this study.

This experimental study tried to figure out the free-surface and free-end effects on flow around half-submerged cylinders. To achieve this goal, two experiments were performed.

Particle image velocimetry was used to investigate the flow around the free end of the cylinders with low aspect ratio piercing the free surface. The flow fields at different vertical and horizontal planes were analyzed for L/D=2.0 , 1.0, 0.5 and 0.3.

From PIV measurement, it was newly found that:

- The core of the longitudinal recirculation region (bubbles) varied at different planes for L/D=2.0 and did not vary so much for L/D=1.0, 0.5, and 0.3.

- The trailing vortex, separation and the arch-type vortex structure were confirmed for L/D=2.0, 1.0, and 0.5. The trailing vortex was not confirmed for L/D=0.3. For L/D=2.0 and 1.0, the von Kármán vortex shedding was confirmed. For L/D=0.5 and 0.3, the von Kármán vortex is suppressed by the free-end effect and does not appear clearly. These were validated by FFT. Horseshoe vortex and tip vortex, which are characteristic for cylinders on the ground plane were not confirmed for both cases.

- The separation flow from near the free-surface is suppressed by free-surface and the rotation axis of vertical vortex is inclined.

Force measurements on stationary cylinders with low aspect ratio piercing the free surface were carried out in a towing tank and a recirculating water

channel mainly to evaluate the free-surface effect. By preparing many different diameter cylinders, the effects of each parameter (Re, AR, Fr) to govern the fluid phenomenon were investigated.

From force measurement, it was newly found that:

- Within the Froude number of 0.05 to 0.5, the effect was almost the same. On the other hand, the differences between 0.03 and 0.74 cases were remarkable. It is considered that Froude number has the positive effect on mean drag coefficient and negative effect on the drag and the lift coefficients fluctuation even at low aspect ratios.

- With decreasing aspect ratio, the free-surface motion is more dominant in terms of frequency.

- As Froude number is up to 0.74, the vortex shedding from the side and bottom of the cylinder was attenuated by the free-surface motion.

- Comparing the free-surface and no-slip conditions, the difference was remarkable at the Froude number of 0.742 and not at the Froude number of 0.293. By suppressing the water surface, mean drag coefficient decreases and RMS of the drag and lift coefficient increases. This tendency is the same as nearly free-slip conditions.

- As aspect ratio increases, RMS of the drag and lift coefficient decrease at first and increase from the middle. This is because free-end effect decreases and the von Kármán vortex sheet develops gradually.

- At super-critical Reynolds number range namely, $Re>3.8\times10^5$, the sharp decrease of drag coefficient was not confirmed at $AR\leqq1.0$ because the free-end effect is dominant and the transition of separation point does not occur at the side of the cylinder.

- At sub-critical Reynolds number range namely, $260<Re<2.8\times10^5$, mean drag coefficient at low aspect ratios decreases and the force fluctuation increases with Re increasing. It is clear for relatively larger aspect ratios,

AR=1.5 and 2.0 due to the less free-end effect.

- For the range of $0.05<Fr<0.5$, the increase of still water force by water running up and down around the cylinder can be neglected even for low aspect ratios, $AR \leqq 3$.

From both results, we can conclude that:

- A simple new model to understand aspect ratio effects are presented.

- Contribution of Kármán vortex with decreased frequency to force fluctuation is not as high as two-dimensional Kármán vortex.

- New conceptual diagrams of flow around half-submerged circular cylinders are presented.

Future work will seek to elucidate the mystery of 'free-slip' condition by CFD.

Appendix

In this section, some examples that applied DMD to another horizontal PIV data are presented.

The similar PIV measurement was carried out at the circulating water channel in Figure 4.27. 1000 snapshots were acquired at a 20Hz. The number of velocity measurement point was 75×100. Further PIV measurement details can be confirmed in Sakata *et al.* (2017).

The time series streamwise vorticity field and velocity field at L/D=2.5 and z/D=-0.5 were processed by DMD. The diameter of the cylinder D was 0.07m and the velocity of the flow was 0.4m. Therefore, the Reynolds number was 28,000.

Results are presented in Figure A.1~A.4. Energy rate was the energy divided by the sum of the energy.

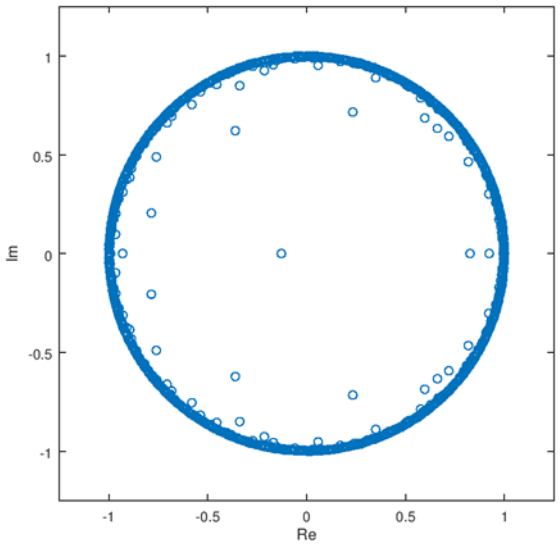

Figure A.1 - Eigenvalues of the time series streamwise vorticity field at L/D=2.5 and z/D=-0.25 by DMD (snapshot number: 1~999)

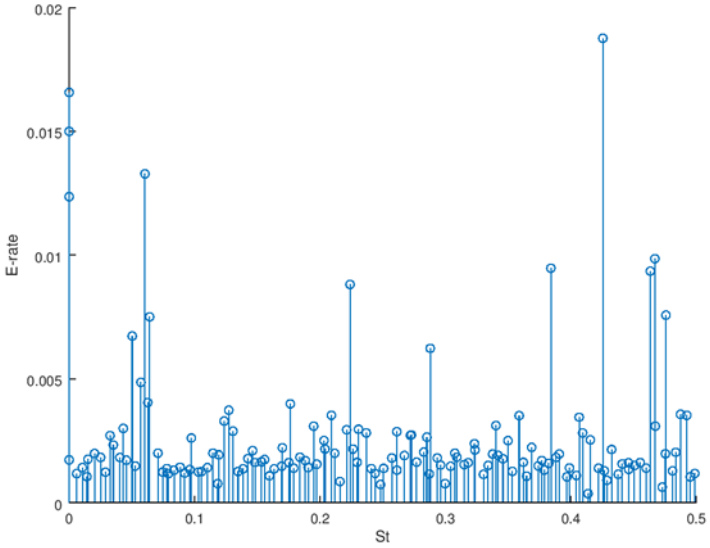

Figure A.2 - Relationship between Strouhal number and Energy rate of the time series streamwise vorticity field at L/D=2.0 and z/D=-0.25 by DMD

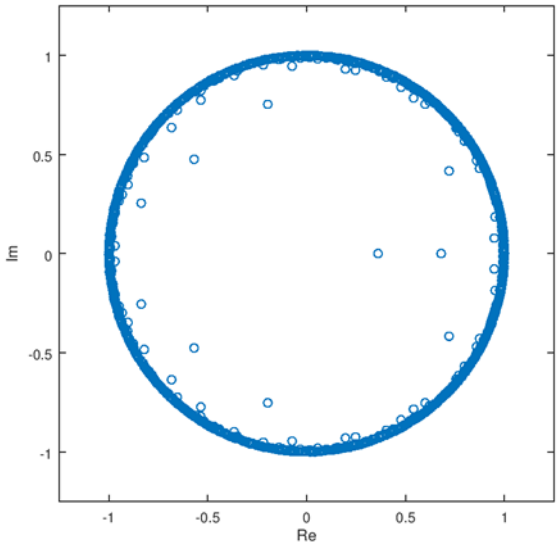

Figure A.3 - Eigenvalues of the time series streamwise vorticity field at L/D=2.5 and z/D=-0.25 by DMD (snapshot number: 1~999)

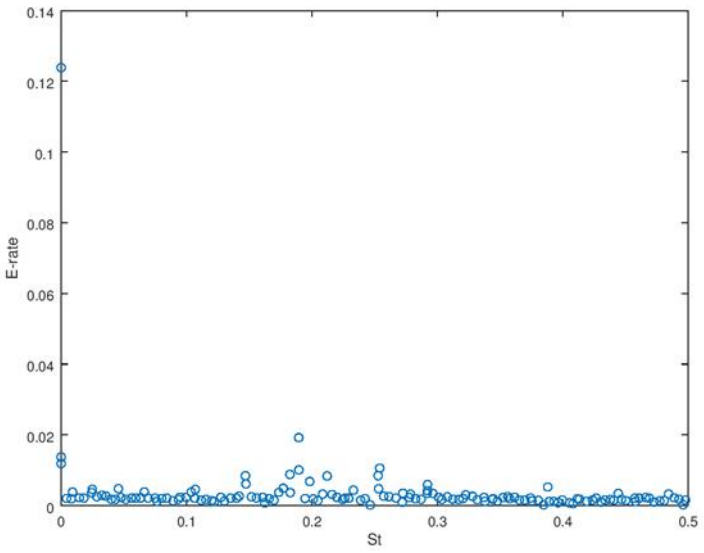

Figure A.4 - Relationship between Strouhal number and Energy rate of the time series streamwise velocity field at L/D=2.0 and z/D=-0.25 by DMD

References

Journals and conference papers

Assi, G.R.S., Meneghini, J.R., Aranha, J.A., Coleto, W.G.P. (2005) "Design, assembling and verification of a circulating water channel facility for fluid dynamics experiments," *Proc. of the ABCM 18th International Congress of Mechanical Engineering*, COBEM. Ouro Preto, Minas Gerais, Brazil.

Benitz, M. A., Carlson, D. W., Seyed-Aghazadeh, B., Modarres-Sadeghi, Y., Lackner, M. A., Schmidt, D. P. 2016. "CFD simulations and experimental measurements of flow past free-surface piercing, finite length cylinders with varying aspect ratios". *Computers & Fluids*, Vol. 136, p. 247-259.

Chaplin, J.R., Teigen, P. (2003) "Steady flow past a vertical surface-piercing circular cylinder," *Journal of Fluids and Structures*, 18 (3–4), pp. 271-285

Farviar, D. (1981) "Turbulent uniform flow around cylinders of finite length. *AIAA J*; 13(3):275-281

Fukuoka, H., Hirabayashi, S., Suzuki, H. (2016) "The effects of free surface and end cell on flow around a finite circular cylinder with low aspect ratio," *Journal of Marine Science and Technology*, Vol. 21(1), pp. 145-153, 2016.

Fujarra, A.L.C., Rosetti, G.F., Wilde, J., and Gonçalves, R.T. (2012) "State-of-art on vortex-induced motion: A comprehensive survey after more than one decade of experimental investigation," *Proc. of the ASME 31st International Conference on Ocean, Offshore and Arctic Engineering*, OMAE2012-83561, Rio de Janeiro, Brazil, 2012.

Hay, A.D. (1947) "Flow about semi-submerged cylinders of finite length," . Princeton University Report, Princeton, NJ

Iungo, G.V., Pii, L.M., Buresti, G. (2012) "Experimental investigation on the aerodynamic loads and wake flow features of a low aspect-ratio circular cylinder," *Journal of Fluids and Structures*, 28, pp. 279–291.

Gonçalves, R.T., Rosetti, G.F., Fujarra, A.L.C., Nishimoto, K. (2010) "Mitigation of vortex-induced motion (VIM) on a monocolumn platform: forces and movements," *J. Offshore Mech. Arctic Eng.*, 132, pp. 041102-1-16.

Gonçalves, R.T., Rosetti, G.F., Fujarra, A.L.C., Oliveira, A.C. (2012) "Experimental study on vortex-induced motions of a semi-submersible platform with four square columns, Part I: effects of current incidence angle and hull appendages," *Ocean Eng.*, 54, pp. 150–169.

Goncalves, R.T., Rosetti, G.F., Franzini, G.F., Fujarra, A. (2013) "Experimental study around circular cylinders with low aspect ratio," 32nd international conference on Ocean, offshore and Arctic engineering. Nantes, France

Gonçalves, R.T., Rosetti, G.F., Fujarra, A.L.C., Oliveira, A.C. (2013) "Experimental study on vortex-induced motions of a semi-submersible platform with four square columns, Part II: effects of surface waves, external damping and draft condition," *Ocean Eng.*, 62, pp. 10–24.

Gonçalves, R.T., Franzini, G.F., Rosetti, G.F., Meneghini, J.R., Fujarra, A.L.C. (2015) "Flow around circular cylinders with very low aspect ratio," *J. Fluid Struct.*, 54, pp. 122–141.

Gonçalves, R.T., Fujarra, A.L.C., Rosetti, G.F., Kogishi, A.M., Koop, A. (2018) "Experimental study of the column shape and the roughness effects on the vortex-induced motions of deep-draft semi-submersible platforms," *Ocean Eng.*, 149, pp. 127–141.

James, R., Ros, M.C. (2015) "Floating Offshore Wind: Market and Technology Review Prepared for the Scottish Government"

Kitagawa, T., Fujino, Y., Kimura, K. (1999) "Effects of free-end condition on end-cell-induced vibration," *Journal of Fluids and Structures*, 13 (1999), pp. 499-518

Koo, B., Yang, J., Yeon, S.M., Stern, F. (2014) “Reynolds and Froude number effect on the flow past an interface piercing circular cylinder,” *Int. J. Nav. Archit. Ocean Eng.*, 6, pp. 529–561.

Koo, B., Park, D., Paik, K. (2014) “A Study on Wave Run-up Height and Depression Depth around Air-water Interface-piercing Circular Cylinder,” *Journal of the Korean Society of Marine Environment & Safety*, 20, pp. 312–317.

Kawamura,T., Hiwada,M., Hibino,T., Mabuchi,I., Kumada,M. (1984) “Flow around a finite circular cylinder on a flat plate,” *Bulletin of the Japan Society of Mechanical Engineers*, 27, pp. 2142–2151.

Khalak, A. & Williamson, C. H. K. 1996 “Dynamics of a hydroelastic cylinder with very low mass and damping,” *Journal of Fluids and Structures* 10, 455-472.

Kitagawa, T., Wakahara, T., Fujino, Y., Kimura, K. (1998) “An experimental study on vortex-induced vibration of a circular cylinder tower at a high wind speed,” *Journal of Wind Engineering and Industrial Aerodynamics* 69-71, 731-744.

Korkischko, I., Meneghini, J.R. (2011) “Volumetric reconstruction of the mean flow around circular cylinders fitted with strakes,” *Experiments in Fluids*, 51, pp. 1109–1122.

Okamoto, T., Yagita, M. (1973) “The experimental investigation on the flow past a circular cylinder of finite length placed normal to the plane surface in a uniform stream,” *Bulletin of the Japan Society of Mechanical Engineers*, 16, pp. 805-814.

Pattenden, R.J., Turnock, S.R., Zhang, X. (2005) “Measurements of the flow over a low-aspect-ratio cylinder mounted on a ground plane,” *Experiments in Fluids*, 39, pp. 10–21.

Palau-Salvador, G., Stoesser, T., Fröhlich, J., Kappler, M., Rodi, W. (2010) "Large eddy simulations and experiments of flow around finite-height cylinders," *Flow, Turbulence and Combustion*, 84, pp. 239–275.

Rosetti, G., Vaz, G., Hoekstra, M., Goncalves, R.T., Fujarra, A. (2013) "CFD calculations for free-surface-piercing low aspect ratio circular cylinder with solution verification and comparison with experiments," 32nd international conference on Ocean, offshore and Arctic engineering. Nantes, France

Sakai, M., Sunada, Y., Imamura, T., Rioie, K.. (2014) "Experimental and Numerical Flow Analysis around Circular Cylinders Using POD and DMD," *AIAA*, pp.1-19.

Sakata, K., Cicolin, M.M., Goncalves, R.T., Hirabayashi, S., Assi, G.R.S. & Suzuki, H. (2018) "PIV measurement study on flow around circular cylinders with low aspect ratio piercing the free surface" *Proc. of the 22nd International Offshore and Polar Engineering Conference*, Sapporo, Japan, 2018.

Sakata, K., Suzuki, H., Hirabayashi, S. (2017) "Research on Vortex-Induced Motion (VIM) of a floating body with low aspect ratio," The 26th Ocean Engineering Symposium, Tokyo, Japan, 2017.

Sareen, A., Zhao, J., Sheridan, J., Hourigan, K., Thompson, M. C. (2018) "Vortex-induced vibrations of a sphere close to a free surface," *J. Fluid Mech.,* 846, pp. 1023-1058.

Suh J., Yang J., Stern F. (2011) "The effect of air-water interface on the vortex shedding from a vertical circular cylinder," *J. Fluid Struct.*, 27 (1), pp. 1-22.

Sumer, B. M., Fredsøe, J. (2006) "Hydrodynamics Around Cylindrical Structures Revised Edition," Advanced Series on Ocean Engineering: Volume 26.

Sumer, D. (2013) "Flow above the free end of a surface-mounted finite-height circular cylinder: a review," *J. Fluid Struct.* 43, pp. 41–63.

van Dyke, M. (1982) “An album of fluid motion,” *1st edn. Parabolic Press.*

Zhu, H., Wang, C., Wang, H., Wang J. (2017) “Tomographic PIV investigation on 3D wake structures for flow over a wall-mounted short cylinder,” *J. Fluid Meh.,* 831, pp. 743-778

Web sites

https://www.equinor.com/en/what-we-do/hywind-where-the-wind-takes-us/the-market-outlook-for-floating-offshore-wind.html

https://www.carbontrust.com/media/670664/floating-offshore-wind-market-technology-review.pdf

http://en.mastekhi.com/board/?id=e21

http://www.ndf.poli.usp.br/

Acknowledgements

It would not have been possible to write this thesis without support from many individuals. Therefore, I would like to express my gratitude towards all of them.

First of all, my gratitude goes to my supervisors. Prof. Hideyuki Suzuki always provided me useful advices at the laboratory meetings. I am also grateful that you permitted me to study in Norway and Brazil. Prof. Shinichiro Hirabayashi is the man who I am most grateful to. Discussions with you were always enjoyable and absolutely indispensable to my research. I must thank you for your kind consideration. Thanks also to Prof. Toru Sato for his thoughts and suggestions as the second reader. My research would not have been better without you.

My gratitude also goes to Dr. Rodolfo Gonçalves, my dear friend. Thank you for your precious advices. I cannot thank you enough. Especially I thank you for giving me the chance to perform the experiment in Brazil. Memories for the six weeks with you and EYu-san are priceless. Let's have parties even after my graduation.

I am also indebted to Prof. Gustavo Assi and Mr. Mulio Cicolin of NDF, USP who helped the PIV measurement. It was great for me to have the opportunity of meeting you in Brazil. I wish to thank Maria, Pedro, Raiza, and Matheus for helping my campus life in USP. I am excited to see you again someday. I would like to acknowledge the JASNAOE for the financial support for the occasion of the PIV measurement in Brazil.

Dr. Yasuo Yoshimura also gave me useful advices. You are like a grandfather to me. I really appreciate that you helped the force measurement late at night. I hope that you stay healthy forever.

Mr. Kato and Mr. Miyanaga helped the force measurement. I really appreciate for you to comply with my unreasonable demands.

Mrs. Ishiwatari and Mrs. Odano helped me with office procedures. Thanks to

you, we students were able to concentrate on the research. Especially Mrs.Ishiwatari took care of Kashiwa members and gave us treats every week at the preceding period.

I wish to thank comrades in the Ocean Space Planning Laboratory, Horiguchi-san, Takase-kun, Jyo-kun, Makimura-kun. Horiguchi-san was at the lab whenever I came. I always loved to chat with you. Takase-kun was a mate since undergraduate. We have been through a lot and grown up right? Jyo-kun dealt with the same topic as me, VIM and it was excited to check each other's progress every week. Makimura-kun has a high ability in document generation. I respect you because I feel that you have something that I do not have. At the preceding period, it was a good memory to eat a hot pot and watch 'Yowamushi Pedal' with you all.

I wish to thank the remaining students of our laboratory, Toyoda-kun, Li-kun, Shiohara-kun, Fukui-kun, Sakai-kun, Katafuchi-kun, Varelio, Fredi, Matheus, Marielle, and Leandro. Sharing time with you such as discussing about hydrodynamics, playing MARIOKART, having lunch, drinking, trip etc… was wonderful. The wonderful experiences really complement the research and makes my student life fruitful. Special thanks to Toyoda-kun for helping the data analysis and Shiohara-kun, Fukui-kun, Varelio, and Fredi for helping the setting of force measurements. Though I am a little bit frustrated with not completing the work thoroughly, I entrust the remain to my juniors and believe that you will make a significant contribution to the world.

I would also like to express my gratitude to graduates, Hirokawa-san, Nakamura-san, EYu-san, Ariyama-san, Kinoshita-san, Shiiba-san, Aline, Daniela, Ulfa, and Tim.

I would also like to thank professors, secretaries and students of the OTPE department. This two years would not be fulfilling without any of you. It was good to choose this laboratory and department.

At the end of the work, I would like to thank my parents for providing me the support and encouragement all this time. I am very happy to be your son.